ABSTRACT

Title of Thesis: UNSTEADY LOW REYNOLDS NUMBER AERODYNAMICS OF A ROTATING WING

Degree Candidate: Siddarth Kolluru Venkata

Degree and Year: Master of Science, 2012

Thesis directed by: Assistant Professor Anya R. Jones
Department of Aerospace Engineering

Micro air vehicles (MAVs) are small, unmanned aircraft useful for reconnaissance. The small size of MAVs presents unique challenges as they operate at low Reynolds numbers $O(10^4)$, and they share a flight regime with insects rather than conventional aircraft. The low Reynolds number regime is dominated by poor aerodynamic characteristics such as low lift-to-drag ratios. To overcome this, birds and insects utilize unsteady high lift mechanisms to generate sufficient lift. A leading edge vortex (LEV), one of these unsteady lift mechanism, is thought to be responsible for the high lift generated by these natural fliers, but the factors which contribute to the formation, stability, and persistence of LEVs are still unclear.

The objectives of this study are to: 1) qualitatively understand the formation of the LEV by evaluating the effect of wing acceleration profiles, wing root geometry, Reynolds number, and unsteady variations of pitch, 2) quantify whether high lift can be sustained at low Reynolds numbers on a rotary wing in continuous revolution, and 3) determine the effect of wing flexibility on the unsteady lift coefficient.

Experiments were performed on a rotating wing setup designed to model the translational phase of the insect wing stroke during hover. Experiments were performed in a water tank at Reynolds numbers between 5,000 and 25,000, and the flow was investigated using dye flow visualization, as well as lift and drag force measurements. A rigid wing and a simple one degree-of-freedom flexible wing were tested.

Dye flow visualization on a rotating wing showed the formation of a coherent LEV near the wing root. The LEV became less coherent further outboard, and eventually burst. As the wing continued to rotate, the location where the LEV burst moved inboard. Dye injection within the burst vortex showed the formation of multiple small scale shedding vortices that traveled downstream and formed a region of recirculating flow (i.e., a burst vortex). Parameter variations in this experiment included velocity profiles, acceleration profiles, and Reynolds numbers.

High lift and drag coefficient peaks were measured during the acceleration phase of the wing stroke at Reynolds numbers of 15,000 and 25,000. After the initial peak, the coefficients dropped, increased, and eventually attained a "steady-state" intermediate value after 5 chord-lengths of travel, which they maintained for the remainder of the first revolution. When the wing began the second revolution, both the lift and drag coefficients decreased, and leveled out at a second intermediate value. Force measurements on a chordwise flexible wing revealed lower lift coefficients. For all of the cases tested, high lift was achieved during the acceleration phase and first revolution of the wing stroke, though values dropped during the second revolution.

UNSTEADY LOW REYNOLDS NUMBER AERODYNAMICS OF A ROTATING WING

by

Siddarth Kolluru Venkata

Thesis submitted to the Faculty of the Graduate School of the
University of Maryland, College Park in partial fulfillment
of the requirements for the degree of
Masters of Science
2012

Advisory Committee:

Assistant Professor Anya R. Jones, Chairman/Advisor
Associate Professor James D. Baeder
Associate Professor J. Sean Humbert

Dedication

To my past, present, and future family.

Acknowledgments

First, I would like to express my deep appreciation for my advisor and mentor, Dr. Anya R. Jones, for her continual guidance and encouragement to look at things from different perspectives. Her enthusiasm towards this work always inspired me to give my best in all respects. I would also like to thank the members of my thesis committee Dr. James D. Baeder and Dr. J. Sean Humbert for their contributions to this thesis.

Special thanks to Andrew Lind for all the time he spent editing my drafts and critiquing my presentations. I also would like to thank Kristy Schlueter, Mark Glucksman-Glaser, Mac MacFarlane, and Moble Benedict for allowing me to bounce ideas off them, and for all their support throughout my research. I would like to acknowledge Nate Beals, Gino Perrotta, and Bao Zhang for their meticulous machining skills and all the help they provided throughout the experimentation process. Warm thanks to my friends, Matt Collett, Pratik Bhandari, Hunter Nelson, Levi DeVries, Ganesh Raghunath, Teju Jarugumilli, Camden Mamigonian, Elena Shrestha, Yashwant Ganti, Shivaji Medida, Taran Kalra, Mathieu Amiraux, and Shane Boyer who made grad school a blast.

Finally, this acknowledgment will not be complete without the mention of my parents and sisters who have always supported me and inspired me to work harder.

Table of Contents

List of Tables

List of Figures

NOMENCLATURE

α	Angle of attack, deg
θ	Wing stroke angle, deg
ν	Kinematic viscosity, m^2/s
ω	Angular velocity, rad/s
b	Span, m
c	Wing chord, m
C_L	Lift coefficient
C_D	Drag coefficient
D	Drag, N
k	Reduced frequency, $\omega c/U_{ref}$
L	Lift, N
L/D	Lift-to-drag ratio
Re	Reynolds number, $U_{ref}c/\nu$
s	Distance traveled at 3/4 span, m
s_a	Distance at 3/4 span over which wing accelerates, m
t	Time, s
U_{ref}	Reference velocity, m/s
CFD	Computational Fluid Dynamics
LE	Leading Edge
LEV	Leading Edge Vortex
MAV	Micro Air Vehicle
PIV	Particle Image Velocimetry
TE	Trailing Edge

Chapter 1

Background

1.1 Introduction

Over the last decade, advances in micro-technologies such as miniature cameras, infrared sensors, and hazardous substance detectors have increased interest in highly portable platforms [1]. One such platform is the micro air vehicle (MAV). Research into MAVs can be traced back to 1997 when the Defense Advanced Research Projects Agency (DARPA) started a program to develop and demonstrate a new type of small air vehicle. This program was intended to inspire the invention of small vehicles capable of sustained hover with a maximum dimension of only 15 cm. The goal of this program was to develop and test emerging technologies that could evolve into a mission-capable flight system for military surveillance and reconnaissance applications.

A typical MAV has a cruise flight speed near 15 m/s and operates at Reynolds numbers $O(100{,}000)$ or lower, sharing a flight regime with birds and insects rather than conventional aircraft [2]. While the definition of a MAV has now grown to encompass a variety of small vehicles, enormous scientific interest continues to drive the development of bird and insect scale autonomous MAVs. Since MAVs are primarily of interest for reconnaissance missions, both endurance and maneuverability are critical. Keenon and Grasmeyer [3, 4] have argued that very small "insect-sized"

MAVs could give the modern military significant operational advantages, despite the currently lower-than-desirable levels of performance of most hover-capable MAVs. Many scenarios are extremely challenging, requiring the vehicle to operate outdoors in gusty environments as well as within confined spaces such as buildings or caves.

Possible missions suggested for MAVs are squad-level combat, battle damage assessment, air or artillery spotting, sensor dispersal, communications relay, and detection of mines and hazardous substances. MAVs could also be equipped with small jamming systems to confuse radar or communications equipment at very short range. MAVs capable of hovering and vertical flight could be used to scout buildings for urban combat and counter-terrorist operations. A MAV could also be included in an airman's survival kit, used by a downed pilot to keep track of approaching enemy search parties, or relay communications to search and rescue units. To successfully execute these missions, MAVs should be capable of efficient hover and also be extremely maneuverable. At large scales, extreme maneuverability is achieved through use of rotary wings, but at MAV-size scales, a bio-inspired flapping wing flight may be desirable. To this end, the present work has examined, under controlled laboratory conditions, some of the unsteady flow phenomenon responsible for lift generation on a flapping wing in hover.

1.1.1 Comparison of MAV Platforms

Many fixed-wing MAV designs, like the Black Widow MAV (Figure 1.1), have been successfully developed and flight tested. They are efficient and have an en-

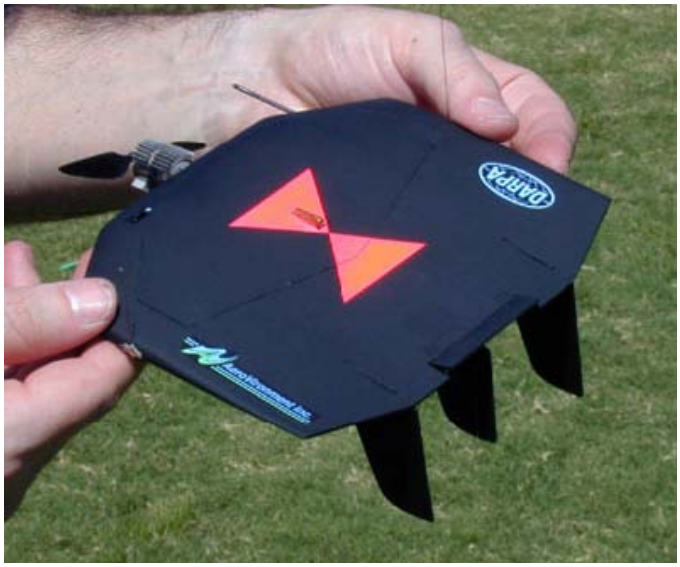

Fig. 1.1: Black Widow MAV, from Ref [5].

durance close to 30 minutes [5]. However, these fixed-wing vehicles lack the ability to hover, and therefore may have difficulty operating in highly constrained environments such as inside buildings or urban areas. Rotary-wing MAVs, on the other hand, have the capability to hover, but their efficiency is significantly lower compared to their fixed-wing counterparts [6]. Furthermore rotary-wing MAVs have limited maneuverability and are less efficient when compared to their larger scale counterparts [7].

The square-cube law is a basic geometric sizing rule stating that wing area is proportional to the square of the characteristic dimensions [8]. This law leads to structural weight becoming a dominant design driver as aircraft get larger. This is illustrated by most birds not being able to hover, while hummingbirds and fruit flies have tremendous vertical climb and hover capabilities [4]. This means that geometric scaling of fixed wings and helicopters may not be ideally suited for operating in

this completely different aerodynamic regime. Therefore, it is important to investigate alternate solutions by drawing inspiration from nature's fliers. As McMasters and Henderson put it, "humans fly commercially or recreationally, but animals fly professionally" [9]. However, there are two challenges in utilizing the flapping wing concept for MAVs: emulating their wing kinematics, and understanding the resulting complex aerodynamics.

1.2 Low Reynolds Number Flight Regime

MAVs operate in the low Reynolds number regime (10^3 - 10^5), which, compared with large, manned flight vehicles, have unfavorable aerodynamics characteristics in steady flow, such as high minimum drag coefficients and low lift-to-drag ratios [10]. Figure 1.2 shows that minimum drag coefficients measured for different airfoils are significantly higher for lower Reynolds numbers.

MAVs' small geometric dimensions, however, do result in some favorable scaling characteristics, such as reduced stall speed and better structural survivability. When compared to other rotating-wing MAV systems, it is clear that flapping wings have thus far achieved relatively low values of hovering efficiencies. However, bio-inspired flapping wings may still be a viable option as a hovering MAV platform because of their maneuverability and agility at this scale [12].

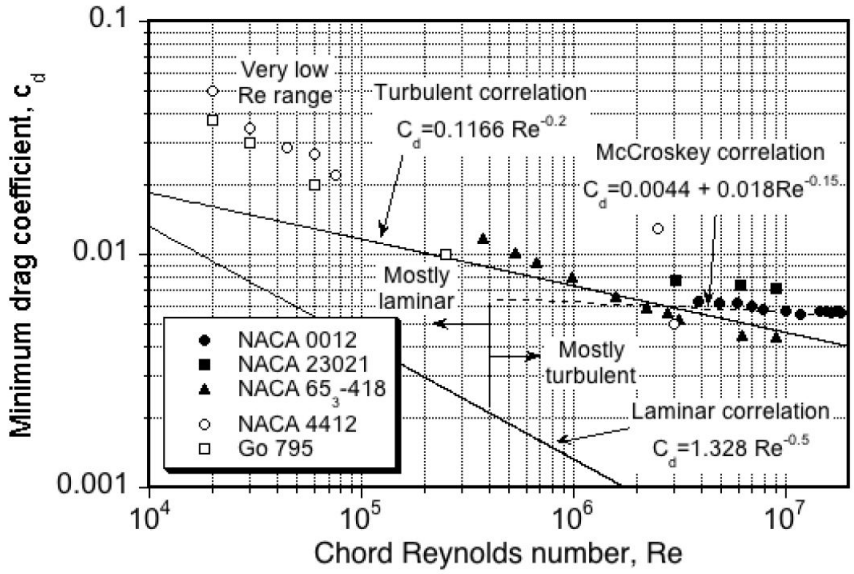

Fig. 1.2: Minimum drag coefficients of different airfoils throughout a range of chord Reynolds numbers, from Ref [11].

1.3 Flapping Wing Flight

Birds and insects are able to generate lift at angles of attack for which the wings of conventional aircraft are stalled, thus achieving a higher lift coefficient. Therefore, an understanding of natural flight will not only help improve aerodynamics, but ultimately influence design and enable new, more efficient and capable MAVs. The nature of flapping wing flight introduces several levels of complexity, primarily due to the unsteady wing kinematics. These unsteady kinematics can lead to the generation of a large number of unconventional and unsteady flow phenomena, which contribute significantly to the resultant forces and moments on the wing.

1.3.1 Avian Versus Insect Flight

In order to further understand flapping wing aerodynamics, it is important to first understand the difference between the two main modes of flapping flight in nature: insect and avian (bird) flight. Conventional fixed-wing aircraft rely on the forward motion relative to the air to produce lift. Biological fliers, on the other hand, not only move their wings forward relative to the air, but also flap up and down, plunge, and sweep. Ellington et al. [13] made the general observation that birds typically operate with attached turbulent flow over their wings and keep the flow attached while insects, on the other hand, have sharp leading edges and separated laminar flow over their wings. The difference in structure and kinematics of bird and insect wings reflect this difference in the flow around their wings.

Birds fly in the Reynolds number range of $10^3 < Re < 10^5$ while insects fly in the Reynolds number range of $10^1 < Re < 10^3$, thus the Reynolds number of the MAV flight dictates which mechanism is to be adopted. The most significant and relevant difference is the ability to hover. While most insects can hover, this capability is restricted to only a few species of birds, such as hummingbirds.

1.3.2 Insect Wing Kinematics

Many insects fly using a reciprocating wing motion [12]. The wing kinematics of this reciprocating motion feature two translational motions and two rotational motions. The translational motions are called the downstroke and upstroke, where the wing sweeps through the air at a relatively large fixed pitch. The two rotational

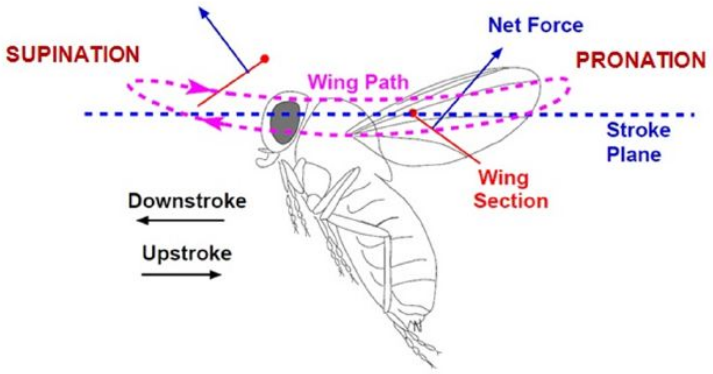

Fig. 1.3: Insect wing kinematics, from Ref [17].

motions are called pronation and supination, where the wing rapidly changes its pitch to reverse the direction of its sweep. Combined, these wing motions result in an overall stroke trajectory in which the wingtip path forms a closed loop and the wings are at a positive angle of attack during both translational motions [14].

Figure 1.3 shows a schematic of a representative flapping cycle, which continuously repeats the process of pronation, downstroke, supination, and upstroke [15]. Insects can also tilt the reference plane of flapping (the stroke plane), thereby varying the direction of the net aerodynamic forces. During the downstroke and upstroke high-lift is produced, in part, by the formation of a leading edge vortex on the wing [13]. Significant lift is also produced during supination and pronation due to rotational circulation and wake capture, a phenomenon that occurs as the wing passes through its own wake created during the previous half-stroke [16].

1.4 Unsteady Lift Enhancement Mechanisms

Natural fliers utilize unsteady flapping mechanisms to generate lift and thrust. Steady and quasi-steady aerodynamic theory, experiments, computations, and modeling have not yet fully explained the ability of flapping wing fliers to generate the required lift to achieve hover and to fly forward at the observed speeds [18]. It is therefore necessary to look at unsteady effects.

The unsteadiness of a flow is characterized by the ratio between forward velocity and flapping velocity, known as the reduced frequency

$$k = \frac{\omega\ c}{U_{ref}} \tag{1.1}$$

where ω is the flapping frequency, c is the wing chord, and U_{ref} is the reference linear velocity. The reduced frequency determines whether either unsteady or quasi-steady methods can be used. Flow is unsteady if $k > 0$, but can generally be considered quasi-steady for a reduced frequency $0 < k < 0.03$, where unsteady effects are not very significant [12]. For $0.03 < k < 0.1$, flow can be considered moderately unsteady, and beyond $k = 0.1$ flow is considered fully unsteady. k is typically between 1 and 10 for small insects [12].

The unsteady aerodynamics of insects is characterized by a constant flapping motion which enables them to hover. Unsteady lift mechanisms are therefore known to be important, but they are not fully understood. In particular, several unsteady lift mechanisms on flapping wings have been recognized in previous research (e.g., Ref [16, 13, 19]) and have been examined further during the course of the present research.

1.4.1 Dynamic Stall

Dynamic stall has been observed on helicopter blades and is known to cause the formation, shedding, and downstream convection of a strong vortex-like disturbance rising from near the leading edge [11]. The concept of dynamic stall centers on the timescale of vortex growth when flow separates from the leading edge. During this process, the fluid mechanics of stall are usually very different from those obtained on an airfoil under static conditions [20]. Once the airfoil exceeds the static stall angle, lift continues to increase despite flow reversal in the boundary layer. As the angle of attack increases further, flow separates at the leading edge and a vortex forms. This vortex convects over the surface of the airfoil, causing additional lift and so the lift curve slope increases [21]. Once the vortex reaches the trailing edge, the flow is fully separated and there is a sharp drop in lift. The flow does not reattach until the angle of attack is reduced to below the static stall angle. A similar type of flow has been observed on insect like flapping wings, resulting in the formation of the leading edge vortex.

1.4.2 Leading Edge Vortex

The formation of a LEV has been noted during many types of flapping wing motions. When the angle of attack of a wing is greater than the stall angle, the flow separates and rolls up into a vortex. This vortex is known as the leading edge vortex (LEV), and is a result of dynamic stall [22]. In flapping wing flight, the presence of LEVs is thought to be essential to delay stall and to augment aerodynamic force

production during translation of flapping wings.

The LEV forms on the upper surface of the wing and can be responsible for significantly increasing lift on the wing. Van Den Berg et al. showed that the LEV can supply up to two-thirds of the required lift during the downstroke [22]. A vortex attached to the leading edge of the wing allows the flow outside of the vortex to reattach to the wing. There are two theories to explain this increase in lift, but these are equivalent. The first, the pressure approach, suggests that the presence of a LEV lowers the local pressure on the upper surface of the wing, thus resulting in an increase in the overall lift [13]. The second, the circulation approach, suggests that the net circulation about the wing is increased due to the presence of the leading edge vortex; the circulation is a measure of the velocity difference above and below the wing [13].

One of the first studies to investigate vorticity in flapping wing flight was by Maxworthy [23]. He observed that during a wing stroke, a vortex formed at the leading edge which then connected to larger vortices at the wingtip. The vortices remained attached and stable through the entire downstroke, therefore explaining the increased lift that could not be explained by inviscid models. He also described a helical structure of the LEV where significant axial flow near the leading edge transported vorticity from the LEV core to the wingtips.

In another study, Van Den Berg and Ellington visualized flow around a mechanical model of the flying hawkmoth, *Manduca sexta*, and demonstrated a LEV forming at the base of the wing and spiraling outward to join the tip vortices [22]. Near the base of the wing, the vortex diameter was quite small and grew radially

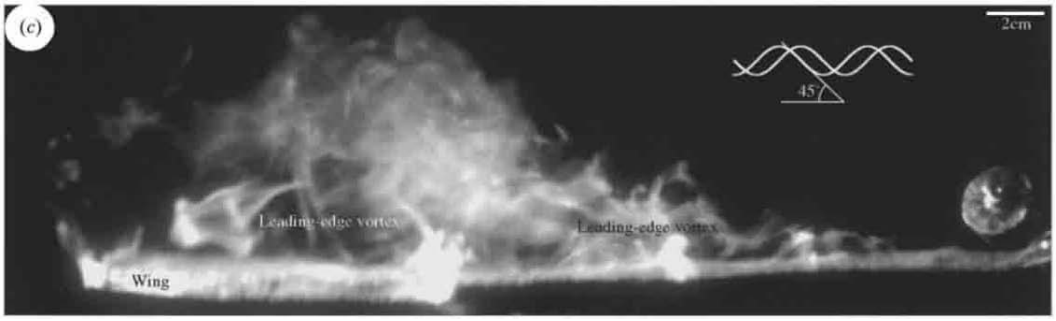

Fig. 1.4: Visualization of a helical LEV indicating a strong axial flow, from Ref [22].

along the leading edge until merging with the tip vortex that swept backward. Smoke visualization indicated a coherent helical vortex starting at the base and stretching more than two thirds of the wing before the structure broke down and connected to larger structures near the wingtips. Figure 1.4 shows an increase in LEV size with distance from the root of the wing. Vortices form as the flow separates over the sharp leading edges, and are stabilized by an axial flow along the leading edge.

The effects observed by the above mentioned models are similar to the thin surfaces of certain delta wing aircraft that use axial flow to maintain a stable LEV for lift production [18, 19]. This flow gives the delta wing a high stall angle of attack, which can be exploited for takeoff, landing, and maneuvering [24]. The delta wing owes much of the lift that it is able to generate to the vortex which is initiated at the leading edge of the wing. This vortex contains a substantial axial velocity component. At high angles of attack, the vortex on a delta wing breaks down. Figure 1.5 shows the vortex breakdown of two leading edge vortices at a location about two-thirds along their length over the top of the wing. The vortex at the top of the photograph exhibits spiral breakdown, where the diameter of the core

increases and the axial velocity component is no longer unidirectional. The vortex at the bottom of the photograph exhibits a bubble-type of vortex breakdown, where the flow becomes chaotic after vortex bursts. When breakdown occurs, the axial velocity component decreases and the pressure increases, the wing loses lift, and the wing stalls [24].

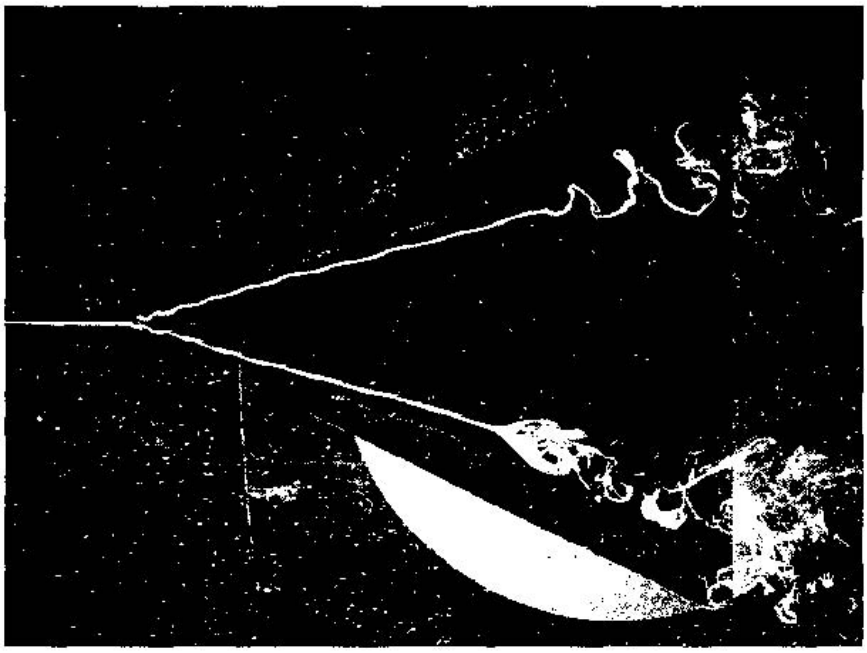

Fig. 1.5: Vortex breakdown over a delta wing, from Ref [25].

LEVs have also been experimentally identified and studied on live insects and birds, as well as mechanical models, e.g., Ref [16, 13, 26, 27, 28]. The phenomenon has been further studied numerically using CFD, e.g., Ref [29, 30]. The detailed characteristics of LEVs, including their formation and shedding processes, have been the focus of much recent research, e.g., Ref [18, 31, 32]. Given its ability to augment the lifting performance of a wing, exploiting the aerodynamic benefits of

LEV generation could be critical in the successful design of MAVs.

1.4.3 Rotational Circulation

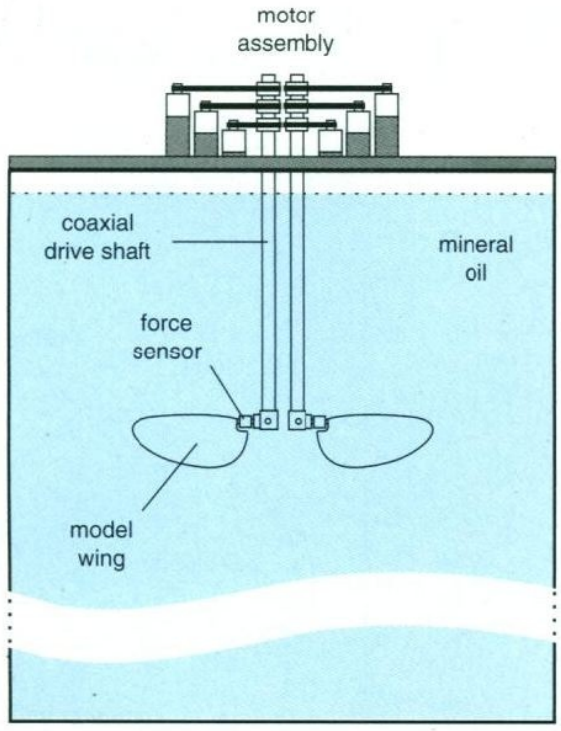

Fig. 1.6: Dickinson's Robofly setup, from Ref [16].

While wing translation with leading edge vorticity is thought to be the primary source of unsteady aerodynamic force production, rotation of the wing during supination and pronation can contribute significant lift as well. In fact, force analysis done on *Drosphelia* kinematics indicated that 35% of total lift production occurs during wing rotation [33]. Dickinson et al. [16] used their 'Robofly' (a dynamically scaled robot that consists of six servo-motors and two coaxial arms, shown in Figure 1.6) along with various rotational patterns, to investigate the relationship

between kinematics and lift generation. They identified two lift force peaks at the end and beginning of each stroke, during pronation and supination. The first force peak (shown in Figure 1.7) can be explained by rotational circulation. The wing's own rotation serves as a source of circulation to generate an upward force [16]. This mechanism, rotational circulation, is akin to the Magnus effect on a spinning baseball [34]. The surface of the rotating ball pulls air within its boundary layer as it spins, thus serving as a source of circulation. As the ball moves through the air, this circulation will increase the total flow velocity on one side and decrease it on the other. During the rotational phase of an insect wing stroke, the direction and magnitude of this rotational lift force is dependent on the pitch angle variation during rotation, the direction of free-stream velocity, and the location of the pitch axis [16,35].

1.4.4 Wake Capture

The wing kinematics employed by insects consists of a reciprocating flapping motion, so their wake repeatedly moves through the wake generated by the previous strokes. This interaction, known as wake capture, may augment the lift force [36].

Wake capture can produce lift by transfer of fluid momentum associated with large scale vortical flow shed from the previous stroke to the wing at the beginning of each half stroke [37]. The wing meets the wake created during the previous stroke after reversing its direction, thus increasing the effective flow speed surrounding the airfoil, which generates the second force peak (shown in Figure 1.7) as observed

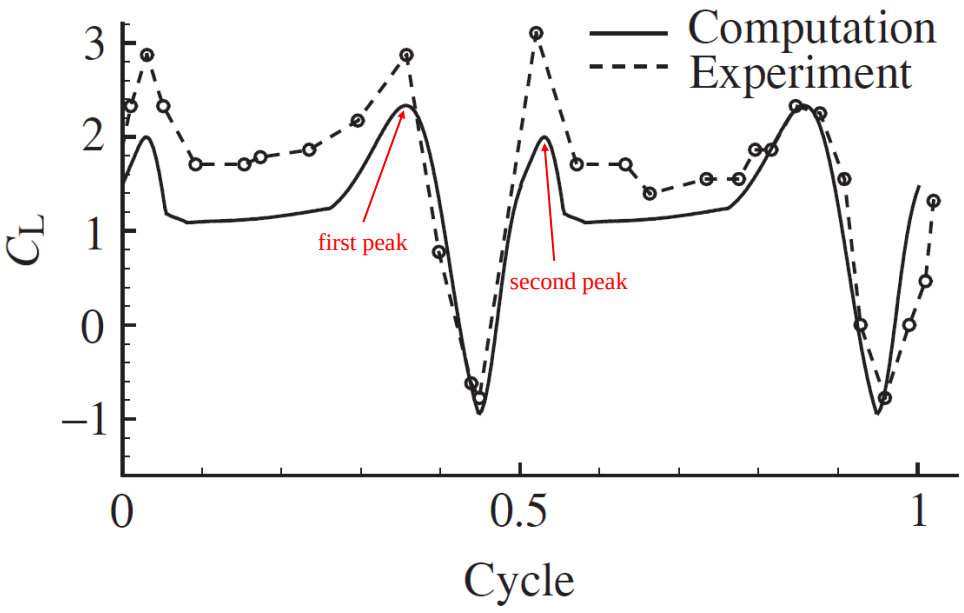

Fig. 1.7: Experimental and numerical lift coefficients for a fruit fly wing at a Reynolds number of 136, showing the two lift peaks at the end of the upstroke and the beginning of the downstroke, from Ref [30].

by Dickinson et al [16]. The key difference between wake capture and rotational circulation is that while rotational circulation manifests as a force transient during rotation, wake capture always occurs after rotation and is reflected as a force transient in the next half stroke.

1.4.5 Wing Flexibility

Although research on flexible wing aerodynamics has been far less extensive than on rigid wings, membrane airfoils (similar to those observed in nature), are likely to be used on MAV flight vehicles due to their low weight. Even though flexible wings add an additional complexity posed by the aeroelasticity, they have been shown to improve performance at high angles of attack through passive shape adaptation [38]. In particular, the stall angle of attack has been shown to increase as much as 20 deg when using a flexible wing versus a rigid wing, while maintaining comparable lift-to-drag ratios throughout the range of angle of attack [12]. At pre-stall conditions, rigid and membrane wings demonstrate similar lift characteristics [39].

Natural insect wings have complex elastic structures with variable stiffness along several axes. Adding some structural flexibility (as opposed to a rigid wing) to a flapping wing has been shown to be beneficial for performance as it allows for the passive control of wing pitch [40]. A two-panel hinged wing serves as a useful model of the passive deformation of an insect wing. A flexible wing can be modeled as a rigid anterior section and a rigid posterior portion separated spanwise by a

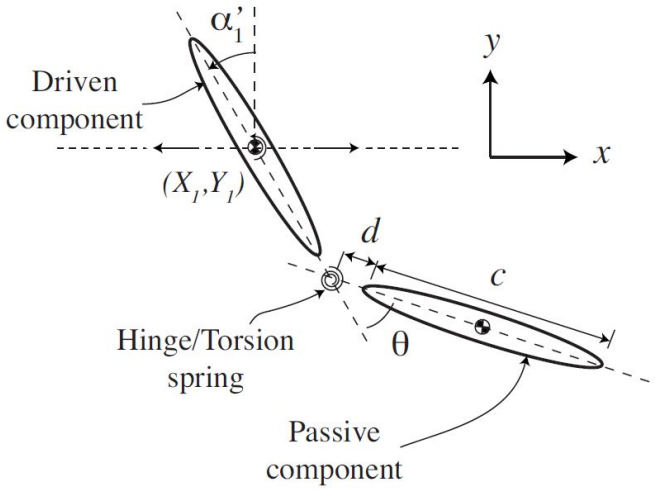

Fig. 1.8: Model system consisting of two rigid elliptical sections connected by a hinge with torsion spring used by Toomey and Eldredge, from Ref [40].

hinge at the mid-chord [41, 42]. This model of a flexible wing (refer to Figure 1.8) as a linkage of rigid panels has previously been used in computational, modeling, and experimental work by Eldredge and Toomey [40, 43, 39]. Their wing model consisted of two rigid sections connected by a hinge with a torsion spring (to model the insect wing's structural stiffness). Both experimental and numerical techniques were used in conjunction to investigate, among other things, the physics behind lift generation on a flexible wing. Toomey et al. [43] found that the power needed to flap the wing was reduced for the flexible wing compared to the rigid wing, but that at large heave amplitudes the effectiveness of the flexible wing was reduced due to premature detachment of the LEV, reducing lift on the wing.

Hui et al. [44] examined various flexible wing structures (latex, nylon, and wood) to evaluate their implications on flapping wing aerodynamics. He showed

that the flexible membrane wings were found to have better overall aerodynamic performance (i.e., lift-to-drag ratio) than the rigid wing at an angle of attack of 10 deg. The rigid wing (wood) was found to have better lift production performance for flapping flight in general. The latex wing, which was the most flexible among the three tested wings, was found to have the best thrust generation performance for flapping flight because the flapping motion of the rigid wing would induce additional drag instead of generating lift. The less flexible nylon wing, which had the best overall aerodynamic performance, was found to be the worst for flapping flight applications. Figure 1.9 shows the measured lift coefficients, drag coefficients, and the lift-to-drag ratio with respect to the orientation angle for the three tested wings by Hui et al. The orientation angle (OA) is the angle of attack of the tested wings with respect to the incoming flows. All three wings were found to have very comparable aerodynamic performances at small orientation angles (OA$<$10 deg). The flexible membrane wings were found to have slightly larger lift and drag coefficients compared with the rigid wood wing at relatively high orientation angles (OA$>$10 deg).

Kim et al. [45] developed a biomimetic flexible flapping wing using micro-fiber composite actuators and experimentally investigated the aerodynamic performance of the wing under flapping and non-flapping motions in a wind tunnel. Results showed that the camber due to wing flexibility could produce positive effects (i.e., stall delay, drag reduction, and stabilization of the LEV) on flapping wing aerodynamics in the quasi-steady and unsteady regions.

Agrawal and Agrawal [46] investigated the benefits of insect wing flexibility on

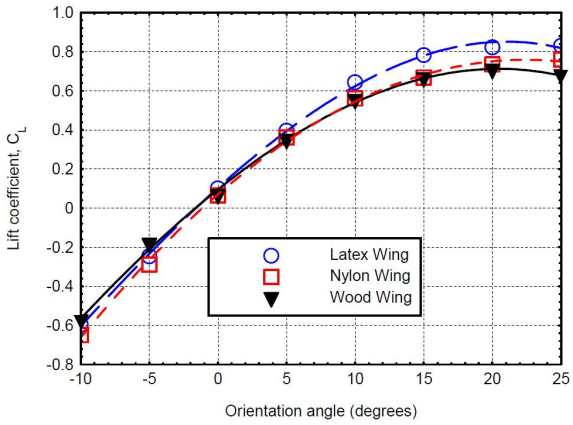

(a) Lift coefficient

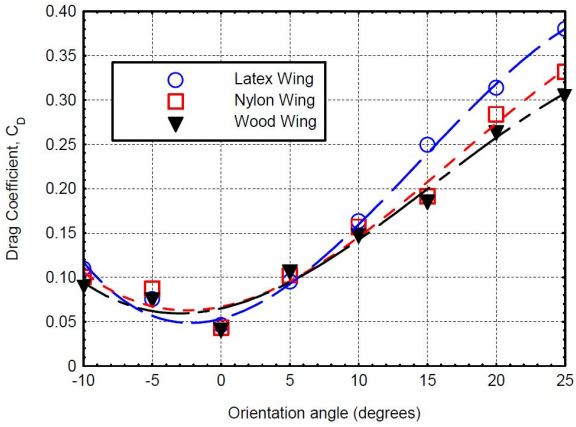

(b) Drag coefficient

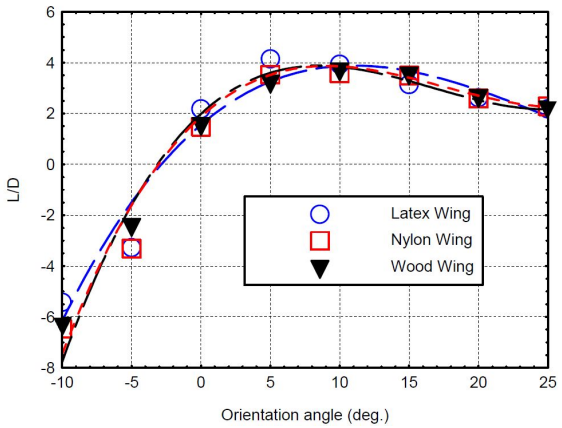

(c) Lift-to-drag ratio

Fig. 1.9: Force measurements for various flexible wings at a Reynolds number of 20,000, from Ref [44].

flapping wing aerodynamics based on experiments and numerical simulations. They compared the performance of two synthetic wings: 1) a flexible wing based on a bio-inspired design of the hawkmoth (*Manduca Sexta*) wing, and 2) a rigid wing of similar geometry. The results demonstrated that more thrust was generated by the bio-inspired flexible wing compared to the rigid wing in all wing kinematic patterns considered. This agrees with the results of Hui et al. [44]. They emphasized that coupled fluid-structure simulations of flexible flapping wings are required to gain a fundamental understanding of the physics and to guide optimal flapping wing MAV designs.

1.5 Experimental Models

1.5.1 Insect like Flapping

Experimental and computational investigations of insect-like flapping wing motions have shown that the flow structures in the wake of low aspect ratio wings have complex three-dimensional forms, which can be fundamentally different from their two-dimensional counterparts. Ellington et al. [47, 48, 49] provides a detailed analysis of wing geometry, kinematics, a discussion on aerodynamic mechanisms, and information on lift and power requirements of natural fliers. Ellington confirmed that most hovering animals flap their wings in a horizontal stroke plane and examined the idea that vorticity generated by separation at the edges of the wing could be a lifting mechanism for hovering flight. He speculated that the LEV may be the primary lift generating vortex, and that the induced spanwise flow from root to tip

may prevent the LEV from shedding throughout each half stroke. Technological advances during the 1990's allowed for more advanced experiments to test these hypotheses.

In a later study by Ellington [13], three-dimensional flow visualization was performed on an actual hawkmoth flapping in a wind tunnel, shown in Figure 1.10. He demonstrated that the LEV remains attached to the surface of wing longer than if flow were purely two-dimensional. Upon performing flow visualization using a robotic model of a flapping hawkmoth, Ellington et al. [13] observed significant spanwise flow within the LEV core, which he then attributed to a spanwise pressure gradient due to higher velocities of the wing tip. He hypothesized that this spanwise flow drains some of the vorticity of the LEV outboard to the wing tip. This, he postulated, retards the vorticity accumulation in the LEV, as compared to the two-dimensional case.

Further tests by Usherwood and Ellington [19] on a mechanical model of a hawkmoth showed a strong LEV during the downstroke and spanwise flow within the LEV core from the wing root to the tip. Near the wing tip, the LEV joined with the tip vortex. It was noted that LEV formation resembled the process of dynamic stall. They also found that the LEV had a helical structure similar to that of a delta wing, and Usherwood et al. hypothesized that the spanwise flow was responsible for this. These results, coupled with the flow visualization done on their robotic flapping model of the hawkmoth, provided new insight into hovering flight.

Birch and Dickinson [18] used digital particle image velocimetry (DPIV) to measure the velocity field around a flapping robotic model of a fruit fly. They found

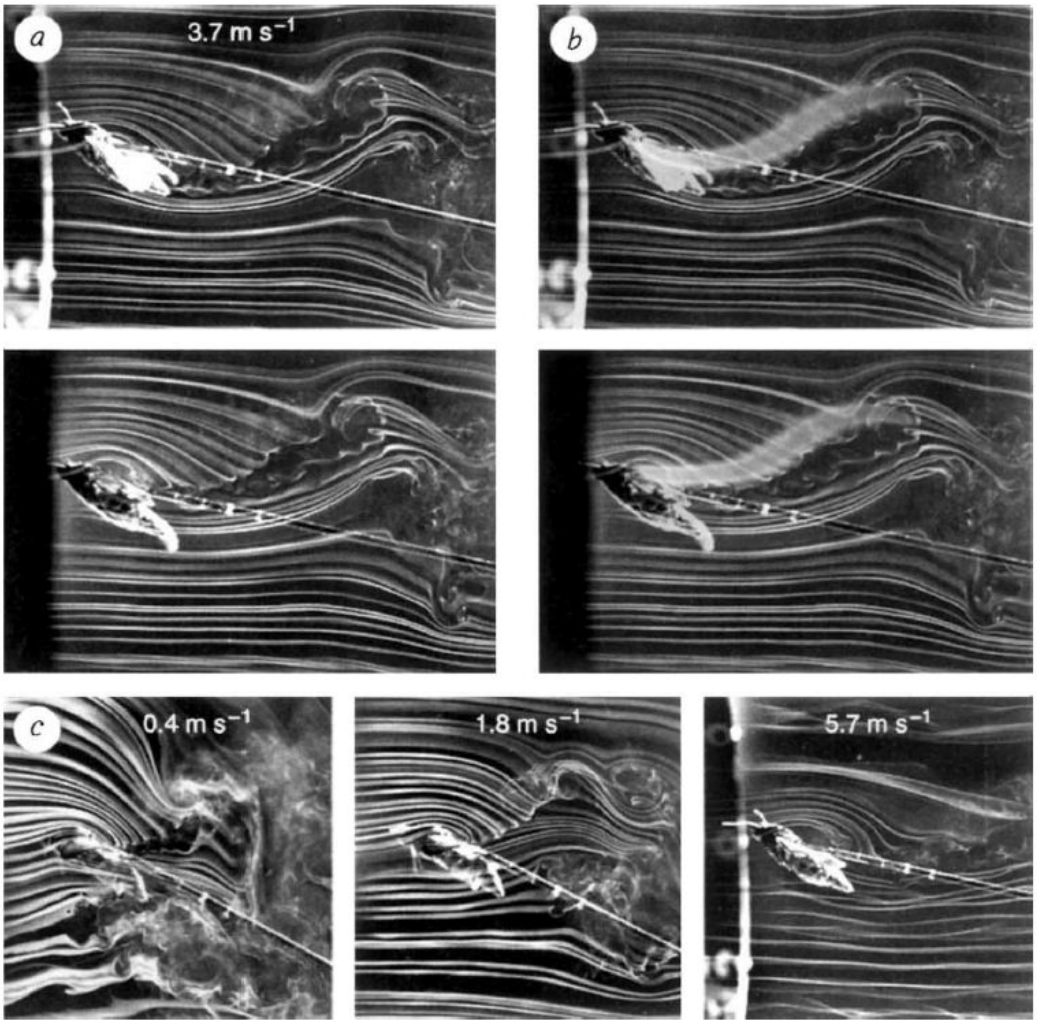

Fig. 1.10: Flow visualization around a female hawkmoth in a wind tunnel, from Ref [13].

only a very small spanwise velocity in the LEV. Additionally, they observed a large tip vortex attached to the wing, which induced spanwise flow behind the LEV, near the wing's trailing edge, as well as a strong downward flow around the wing. The flow from the previous wing stroke also contributed to this downward flow. Birch and Dickinson hypothesized that this induced downward flow significantly lowers the effective angle of attack of the wing, thus retarding the growth of the LEV and delaying shedding.

To further study the effect of spanwise flow, Birch and Dickinson [18] applied fences and baffles on the upper surface of the wing (as shown in Figure 1.11) to inhibit spanwise flow. They demonstrated that despite decreased spanwise flow, the LEV still did not detach from the wing. These authors emphasized that their results suggested some dependence upon Reynolds number as it affects the stability characteristics of the LEV. This hypothesis is different from those reported by Ellington [13]. Therefore, there is disagreement over the mechanisms that keep the LEV attached to a wing.

In another study, Birch and Dickinson [50] made force measurements on the flapping motion of a dynamically scaled fruit fly wing at two different chord Reynolds number of 120 and 1,400. They found that the wing showed relatively constant force generation during its wing stroke. They suggested this could be due to the presence of a stable LEV. They also noted a higher lift coefficient occurred at higher chord Reynolds numbers. The maximum lift coefficient at a chord Reynolds number of 120 was 1.7, whereas at a chord Reynolds number of 1,400 they found a maximum lift coefficient of 2.1 [50].

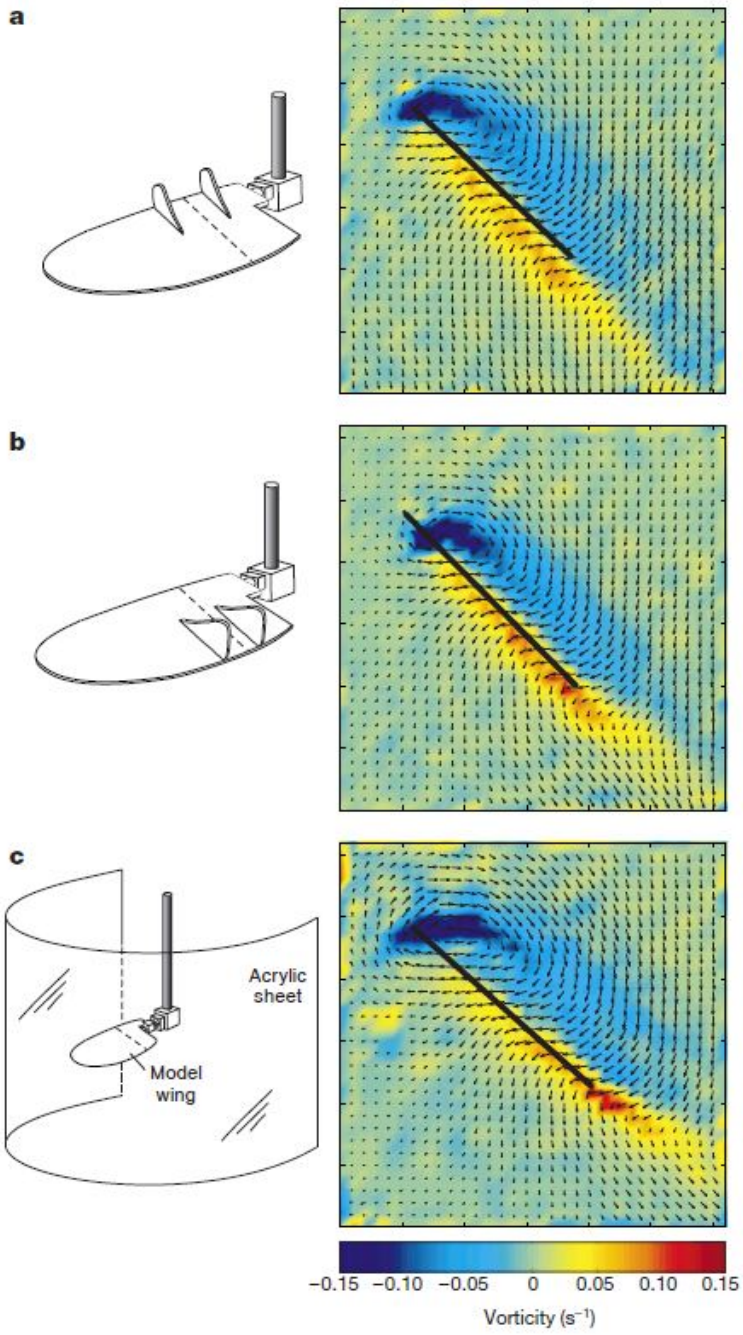

Fig. 1.11: Birch and Dickinson's setup: a) Fences on the leading edge, b) Fences on the trailing edge, c) Acrylic tip wall. The column on the right shows the presence of vorticity, from Ref [18].

More recently, Srygley and Thomas [27] have observed LEVs on butterfly wings in free flight at $Re = O(10^3)$[1] and examined the LEV development in various modes of flight (climb, maneuver, forward flight). During climb, they found that two LEVs formed on the upper surface of the wings. They postulated that in these particular flight modes, the insect required more lift and modified its wing kinematics to exploit lift enhancement from the LEVs. During forward flight, however, the LEVs were not observed on the wings. Their research also demonstrated that the LEV generated by the butterfly produced a LEV of approximately constant diameter across the wing span, as opposed to the spiral LEV structure seen on the hawkmoth [27].

Extensive flow visualization studies were performed by Singh and Chopra [15] and Ramasamy and Leishman [31] on a MAV scale flapping wings at a Reynolds number of 15,500. Their work showed the formation of unstable (i.e., shedding) LEVs. Figure 1.12 shows the LEV shedding process through the downstroke of the wing motion as taken from Ramasamy and Leishman [31]. Additionally, they showed that the shedding of the LEV occurred despite a significant spanwise flow on the upper surface of the wing. They noted that the continuous presence of at least one vortex over the wing might help to explain the sustained lift generation shown by flapping wings during stationary hovering flight.

Wilkins and Knowles [51] showed that for an LEV to be stable, the creation of vorticity at the leading edge must be matched perfectly by the convection and diffusion of vorticity into the wake, thus creating a stable equilibrium. Spanwise

[1] An estimate calculated from the free stream velocity and the known dimensions of the *Vanessa atlanta* butterfly.

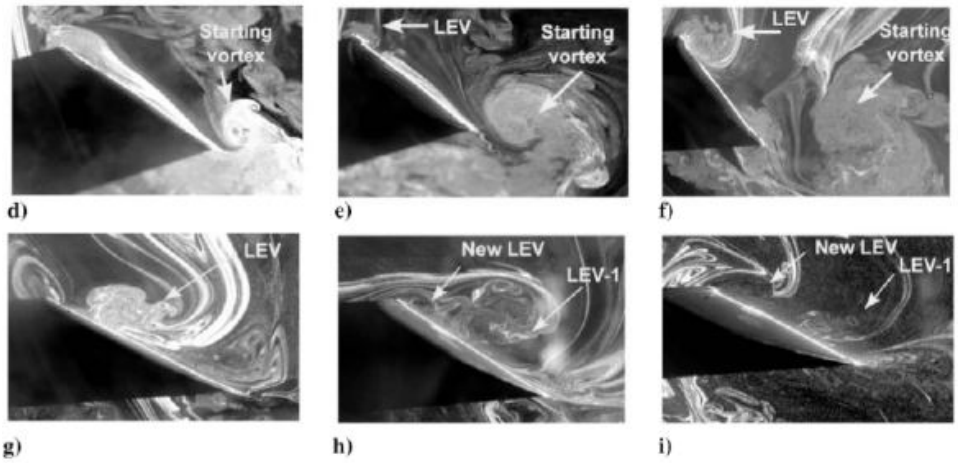

Fig. 1.12: Chordwise flow visualization images by Ramasamy and Leishman: d) Start of translational stroke, e) Accelerating wing, f) Midpoint of translational motion, g) Spilled LEV, h) Formation of new LEV, i) Multiple vortices, from Ref [31].

flow therefore provides a mechanism that stabilizes the LEV, generating sufficient lift. This agrees with what Ellington and Usherwood determined earlier [52]. Sane et al. [53] concluded that axial flow through the LEV core stabilized the LEV at the laminar Reynolds number of insect flight even at large incidence, indefinitely delaying stall. At Reynolds numbers less than 100, the three-dimensional flow around a flapping wing was remarkably self-stabilizing. At higher Reynolds numbers, the LEV periodically grew and broke away, limiting the mean value of the lift coefficients. Sane attributed this instability to the absence of axial flow.

1.5.2 Revolving Models

The propeller-like rotating wing is a popular model of insect-like flapping. It was designed to isolate the translational phase of the wing stroke. To date,

propeller experiments typically involve rotating a wing at a constant angle of attack in the absence of a free-stream. Usherwood and Ellington experimentally studied revolving hawkmoth wings at Re O(10^3). Usherwood et al. showed that the lift coefficient was found to decrease as Reynolds number increased from 10,000 and 50,000. He postulated that a weaker LEV formed at higher Reynolds number [19, 54]. Usherwood and Ellington also examined the lift and drag production on rotating wings for a fairly wide range of parameters, including angle of attack, twist, and camber. At an angle of attack around 41 deg, they showed that wing lift coefficient can reach as high as 1.75 if a stable LEV is produced over the wing.

At lower Reynolds numbers O(1,000), DeVoria et al. [55] experimentally investigated the three-dimensional vortex flow of low aspect ratio plates executing rotational motions from rest at fixed angles of attack. DeVoria employed flow visualization and DPIV to examine the flow structure on a trapezoidal plate and a rectangular plate. For the trapezoidal plate at angle of attack of 90 deg, the flow was found to be dominated by a strong trailing vortex, while the overall flow structure was a symmetrical ring-like vortex. At high speeds, the ring-like vortex was observed to shed before the wing motion ended. DPIV results indicated that this was due to a strong root-to-tip velocity induced by the tip vortices, and a Kelvin-Helmholtz-like instability in the separated shear layer at the tip. For the rectangular plate at a fixed angle of attack of 45 deg, flow visualization revealed the presence of a strong spanwise flow and an attached LEV early in the motion, which then burst over the outboard half of the wing. The LEV observed on the wing was spiral-shaped and attached to the wing early in the wing motion. Kelvin-Helmholtz-like instabilities

were observed in the shear layer, and he postulated that this contributed to the breakdown of the LEV structure.

In another study, Ozen et al. used PIV to characterize the steady-state flow structure on a low aspect ratio rotating plate at fixed angles of attack ranging from 30 to 75 degrees in a water tunnel. He observed a stable LEV for a range of Reynolds numbers between 3,600 and 14,500 [56].

Other experiments on a rotating wing model accelerating to similarly high Reynolds numbers focused on the wing startup and revealed the development of an unstable LEV that forms and sheds early in the wing stroke, resulting in high-lift transients. Jones and Babinsky [57, 58, 59] studied the fluid dynamics associated with a three-dimensional 2.5% thick waving flat plate. The flow development around a waving wing at $Re = O(10^4)$ was studied using PIV to capture the unsteady velocity field. Vorticity field computations and a vortex identification scheme revealed the structure of the three-dimensional flow-field, characterized by strong leading edge vortices. A transient high-lift peak approximately 1.5 times the quasi-steady value occurred in the first chord-length of travel, caused by the formation of a strong attached leading edge vortex. This vortex then separated from the leading edge, resulting in a sharp drop in lift. As weaker leading edge vortices continued to form and shed, lift values recovered to an intermediate value. They also reported that the wing kinematics had only a small effect on the aerodynamic forces produced by the waving wing if the acceleration is sufficiently high.

1.5.3 Computational Studies

In addition to the experimental studies, numerous studies have been conducted using computational fluid dynamics (CFD). Computations on flapping wings have specifically examined the aerodynamic characteristics of hawkmoth and fruit fly wing shapes. Liu et al. [60] conducted numerical simulations of the flow around a hawkmoth in order to study the unsteady aerodynamics of hovering flight. The LEV and the spiral axial flow during translation in their results are consistent with those reported by Ellington. Shyy and Liu [29] performed CFD on flapping wings for a range of Reynolds numbers, and specifically examined the hawkmoth and fruit fly wing geometries used in previous research. They found a much more pronounced spanwise flow through the core of the LEV on the hawkmoth wing compared to the fruit fly, which was consistent with previous findings by Usherwood and Ellington [19]. In their evaluation of the stability of the LEV, the results showed that the fruit fly wing maintained a stable LEV throughout its translational stroke, whereas on the hawkmoth model, the LEV was shed during the downstroke.

Bush et al. [61] successfully reproduced LEV behavior at low and moderate Reynolds numbers in terms of LEV stability and spanwise flow as observed by Birch and Dickinson [62], using an immersed boundary solver. The computed drag during translational flapping, agreed with the experimental data of Sane and Dickinson [63].

In another study, Blondeaux et al. [64] and Dong et al. [65] characterized the features of vortical structures and their interaction in the near-wakes of an

elliptical planform undergoing periodic flapping motion. They presented a basis for comparison with selected features of the aforementioned force measurements and visualization studies. Taira and Colonius [66] computed the wake structure from various configurations of impulsively translating plates and characterized the strong interaction between the tip and trailing edge vortex systems. Brunton et al. [67] used the same computational approach used by Taria to define the wake structure of a pitching plate.

1.6 Summary

MAVs are likely to benefit by mimicking some features of insect flight kinematics. Although conventional fixed wings can perform well in the laminar flow regime, at very low Reynolds numbers, it is possible to generate higher lift forces using a flapping wing configuration by exploiting unsteady aerodynamic mechanisms. Various lift enhancement mechanisms that are employed by insects were discussed, including LEVs, rotational circulation, and wake capture. Experimental and computational studies on both real and mechanical insects have identified the LEV as an important high lift mechanism that accounts for some of the additional lift produced by flapping insect wings when compared to fixed or rotary wings. However, there remains considerable uncertainty about the factors that control the stability of the LEV. Therefore, understanding the LEV characteristics, such as the formation, persistence and shedding, may be important for the design of a successful MAV.

1.7 Objective of Present Work

The objectives of the present work are:

1. To qualitatively understand the formation, stability, persistence, and importance of the leading edge vortex in the generation of lift on insect-like flapping wings by evaluating the effect of:
    - Wing acceleration profiles
    - Wing root geometry
    - Reynolds number
2. To characterize the flow structure on a pitching-and-rotating wing and thereby understand the effect of unsteady variations of pitch on the three-dimensional flow structures.
3. To determine whether LEVs can provide high lift at low Reynolds numbers on a rotary wing in continuous revolution.
4. To quantify the effect of wing flexibility on the lift and drag coefficients on a rotating wing and determine whether there are advantages over a rigid wing.

To this end, the work presented in this thesis employs a new three-dimensional model for the insect-like wing stroke, combining both wing rotation and unsteady pitch changes. This setup combines unsteady wing rotation (including starting/stopping, acceleration profiles, and continuous revolution) and unsteady variations in pitch. Dye flow visualization is used to qualitatively understand the evolution of unsteady

flow structures on a rotating wing. Force measurements are used to investigate the lift and drag produced on a rotating wing at a fixed angle of attack. Finally the flow structures on a pitching-and-rotating wing were qualitatively characterized.

1.8 Outline of Thesis

The present work explores the development of the LEV and the role it plays in generating lift on flapping wings. The motivation behind MAV development and the fundamentals of flapping wing aerodynamics have been discussed in this chapter. A review of past research on unsteady lift mechanisms, especially the LEV, and comparisons between rigid and flexible wings has also been presented. Chapter 2 gives a comprehensive description of the experimental techniques that were utilized to characterize the LEVs and to measure the aerodynamic forces, including dye flow visualization and force measurements. The fundamental principles, equipment used, and challenges unique to each experimental technique are explained. Chapters 3 and 4 document the results in terms of qualitative (flow visualization) and quantitative (force measurements) results for rigid and flexible wings at different Reynolds numbers, velocity profiles, and acceleration profiles. Chapter 5 concludes the thesis by discussing the significance of the findings and suggesting future experiments towards a better understanding of flapping wings for MAV applications.

Chapter 2

Methodology

2.1 Overview

Dye flow visualization and force measurement experiments were performed to gain new insight into hovering aerodynamics and help understand the complex flow field generated by a rotating wing. This chapter provides a description of the experimental setups, the equipment used, and the challenges in performing such experiments.

2.2 Experimental Setup

Experiments were performed in a 4 ft×4 ft×4 ft (1.2 m×1.2 m×1.2 m) water tank (shown in Figure 2.1) at the Low Reynolds Number Aerodynamics Laboratory (LRAL) at the University of Maryland, College Park. The target Reynolds number range for these experiments is 5,000 to 25,000, selected to provide data for comparison with results available at Reynolds numbers between 1,000 and 50,000.

Water was used as the working fluid so that measurable lift and drag forces could be obtained without the need for high rotation speeds. For example, the Reynolds number is defined as

$$Re = \frac{U_{ref}\ c}{\nu} \tag{2.1}$$

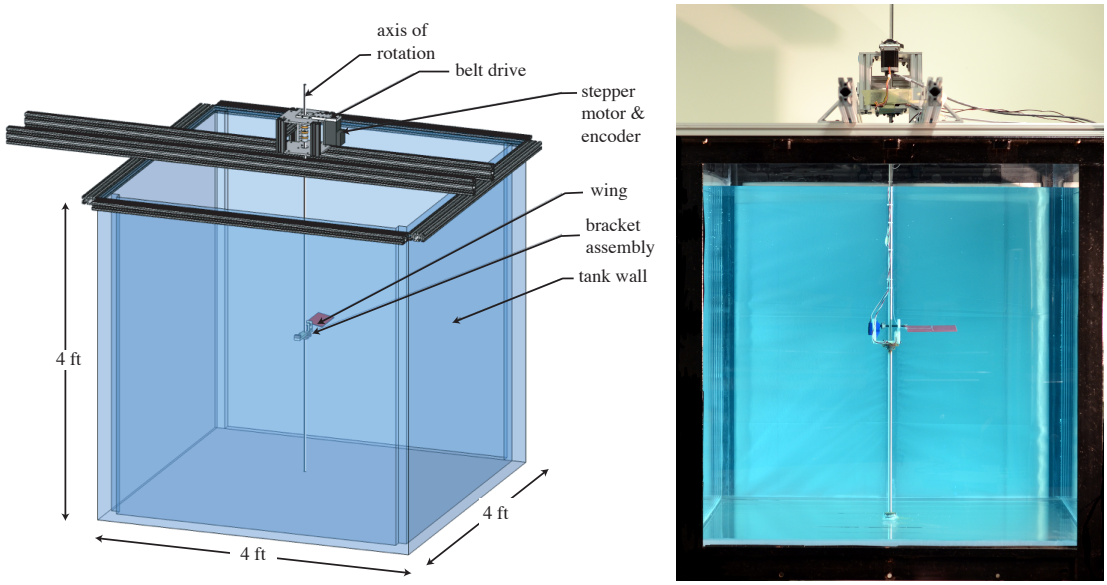

Fig. 2.1: The pitching and rotating wing setup.

where U_{ref} is the local velocity at the three-quarter span reference plane (shown in Figure 2.2(a)), c is the wing chord, and ν is the kinematic viscosity of the working fluid. Rearranging to solve for U_{ref},

$$U_{ref} = \frac{Re\ \nu}{c}. \tag{2.2}$$

The kinematic viscosity of water is 1.052×10^{-5} $\mathrm{ft^2\,s^{-1}}$ and the kinematic viscosity of air is 1.640×10^{-4} $\mathrm{ft^2\,s^{-1}}$. Keeping the chord of the wing constant at 0.25 ft (3 in) and a picking reference Reynolds number of 15,000,

$$\text{for water}: \quad U_{ref} = \frac{15,000 \times 1.052 \times 10^{-5}}{3} = 0.63\,\mathrm{ft\,s^{-1}} \tag{2.3}$$

$$\text{for air}: \quad U_{ref} = \frac{15,000 \times 1.640 \times 10^{-4}}{3} = 9.84\,\mathrm{ft\,s^{-1}} \tag{2.4}$$

therefore, operating in water allows for approximately 93% slower rotational speeds than air. It is easier to capture flow structures at slower rotational speeds for dye flow

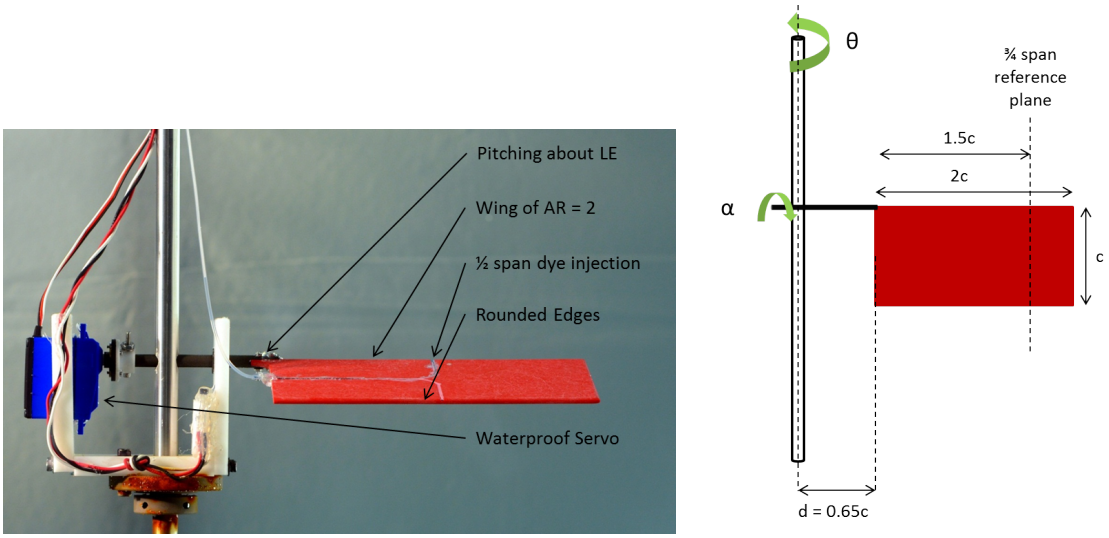

(a) U-bracket assembly

(b) Wing dimensions

Fig. 2.2: The pitching-and-rotating wing on the U-bracket assembly and wing dimensions.

visualization experiments as there is enough time for the dye to fill the structures completely, making them easier to see.

Figure 2.1 shows the pitching-and-rotating wing setup. The wing rotation was driven by a stepper motor above water and pitch by a submerged servo motor. Above the tank, an aluminum structure (80/20) supported the rig and stepper motor. A 0.5 in diameter stainless steel rod extended down into the tank and was inserted into a bearing on the tank floor. The top of this rod was connected to a belt drive system consisting of toothed pulleys (1:5), a rubber toothed belt, a stepper motor with a maximum torque of 265 oz-in, a driver, and an encoder to record position data. The stepper motor was controlled via LabVIEW through a NI USB X-Series 6341 DAQ card.

The experimental rig was designed such that, depending on the type of testing

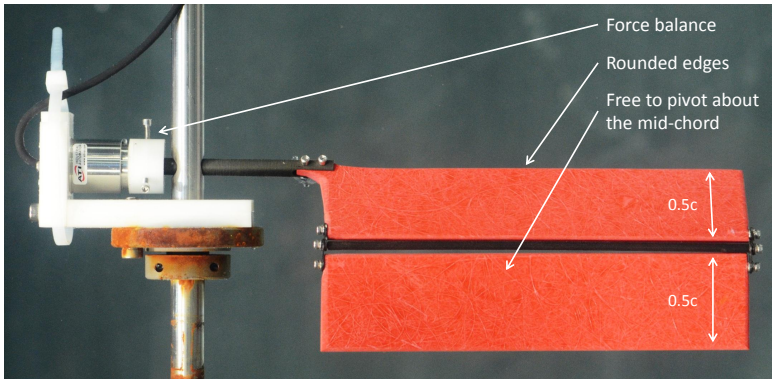

Fig. 2.3: L-bracket assembly with flexible wing and force balance.

(rotating-only or pitching-and-rotating), the rig can be modified to handle either a submersible servo motor for pitch control (Figure 2.2(a)) or a force transducer (Figure 2.3). The submersible servo motor was used to vary the angle of attack of the wing, and the force transducer was used to measure the forces acting on the rotating-only wing. For the pitching-and-rotating wing setup, a Traxxas waterproof servo motor (max torque 84 oz-in) was mounted near the wing root, on a Delrin U-bracket. The motor can drive $\pm$ 45 deg pitch changes about the leading edge via a tygon shaft as shown in Figure 2.2(a). The Delrin U-bracket was then mounted on the long stainless steel shaft. The distance between the wing root and the axis of rotation was 0.65c. A schematic of the setup with dimensions is shown in Figure 2.2(b). For the rotating-only wing setup, a force transducer (discussed further in Section 2.5.2) was mounted near the wing root on a Delrin L-bracket.

A rectangular wing with a chord of 3 in and an aspect ratio 2 was machined from a 4.5% thick fiberglass flat plate. The chord of the wing was sized to allow five chord-lengths of space between the wing tip and the walls of the tank to avoid wall

effects. Tip vortices are typically about one and a half times the chord of the wing [24], therefore a distance of five chord-lengths was chosen to aviod interference from the walls of the tank.

Natural fliers employ flexible wings, therefore, a "flexible-wing" free-to-pivot about the half chord was also machined from the 4.5% thick fiberglass flat plate. The aspect ratio 2 flexible wing shown in Figure 2.3 was hinged at the half chord by a 6 in nylon rod and dismantled chain links. This design was adopted from Eldredge and Medina [39]. However, unlike the wing developed by Eldredge et al., the flexible wing used in this experiment was not given structural stiffness by the use of a spring, and the gap between the panels was not covered or filled in (except by the nylon rod). Since the trailing half chord of the flexible wing was free-to-pivot, it hung down vertically (at a 90 deg angle of attack) before the wing motion began, as illustrated in Figure 2.4. The anterior portion of the wing was held at a fixed angle of attack of 45 deg. Once the wing began rotating, the trailing half of the wing deflected upwards to a "steady-state" position.

2.3 Wing Kinematics

Experiments were performed at a local Reynolds number ranging from 5,000 to 25,000 at the three-quarter span reference plane. The stroke angle, θ, is defined as the angle through which the wing rotates from rest to the point of interest. It is given by the encoder, which is mounted to the bottom of the stepper motor that drives wing rotation. Figure 2.5 shows the top-down view of the wing rotation in

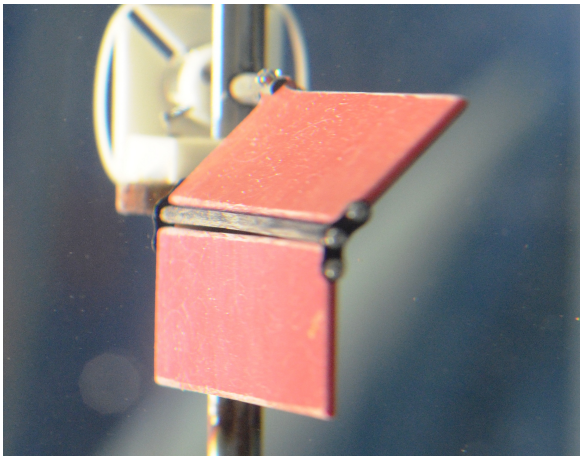

Fig. 2.4: Flexible wing at rest.

the tank. The non-dimensional distance traveled at the three-quarter span reference plane is s/c (Equation 2.5), where s is the arc length traveled by the three-quarter span reference plan normalized by c, the wing chord, and θ is the stroke angle in radians.

$$\frac{s}{c} = 2.15\ \theta. \tag{2.5}$$

In Equation 2.5, the $2.15c$ is the distance from the axis of rotation to the three-quarter span reference plan.

2.3.1 Rotation Only

The wing was set at a fixed angle of attack and accelerated linearly from rest over distances of 0.25, 0.50, 0.75, and 1.0 chord-lengths of travel at the reference plane as shown in Figure 2.6. The distance over which the wing accelerated is defined as s_a and is normalized by the wing chord c. This ratio is expressed as s_a/c. The acceleration phase of the wing stroke was programmed using two different velocity

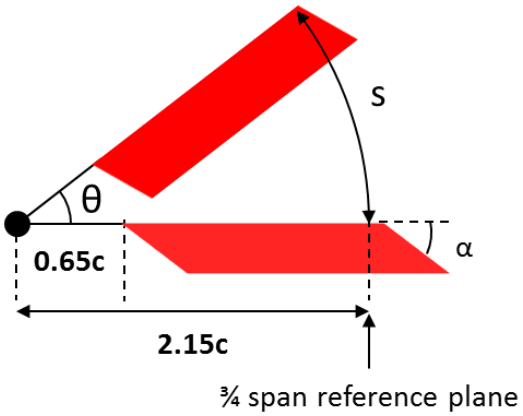

Fig. 2.5: Top-down view schematic of the rotating-only wing setup.

profiles, linear and smoothed. The linear velocity profile is given by

$$\omega(t) = \frac{\omega_{max}}{t_1} t \tag{2.6}$$

where $\omega(t)$ is the angular velocity, ω_{max} is the prescribed steady-state rotational velocity to be reached at a time t_1, and t is time. t_1 is the time over which the wing accelerates from rest to constant angular velocity. ω_{max} was determined based on the required three-quarter span Reynolds number ($Re_{3/4}$), using

$$U_{ref} = r_{ref}\ \omega_{max} \tag{2.7}$$

where U_{ref} is the reference velocity at the three-quarter span reference plane and r_{ref} is the distance from the axis of rotation to the three-quarter span reference plane, equal to $2.15c$. Therefore,

$$U_{3/4} = 2.15\ c\ \omega_{max}. \tag{2.8}$$

Substituting Equation 2.8 into Equation 2.1,

$$Re_{3/4} = \frac{2.15\ \omega_{max}\ c^2}{\nu}. \tag{2.9}$$

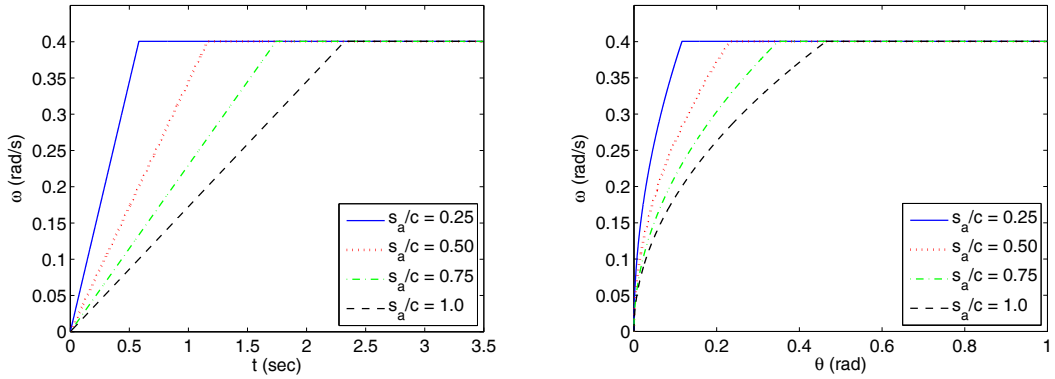

(a) Angular velocity as a function of time (b) Angular velocity as a function of stroke angle

Fig. 2.6: Rotating wing kinematics for a wing accelerating linearly in time, over 0.25, 0.50, 0.75 and 1.0 chord-length of travel at a three-quarter span Reynolds number of 5,000.

Figure 2.7 shows ω_{max} and t_1 for a wing with constant acceleration over 0.50 chord-lengths of travel.

The abrupt starting and stopping that occurs during the linear velocity profile can cause vibrations during testing. To mitigate this, the beginning and end of the wing stroke was smoothed as illustrated in Figure 2.12. Moreover, this more closely resembles the kinematics of a natural flier [12].

A hyperbolic cosine function for smoothing flapping wing kinematics was originally developed by Eldredge et al. [68] for a pitch-up, hold, and pitch-down kinematic study. The function smooths the higher derivatives of the motion to minimize acceleration effects, and was defined as

$$G(t) = \ln\left[\frac{\cosh(aU_1(t-t_1)/c)\cosh(aU_1(t-t_4)/c)}{\cosh(aU_1(t-t_2)/c)\cosh(aU_1(t-t_3)/c)}\right] \quad (2.10)$$

$$\alpha(t) = \alpha_{max}\left[\frac{G(t)}{\max(G(t))}\right] \quad (2.11)$$

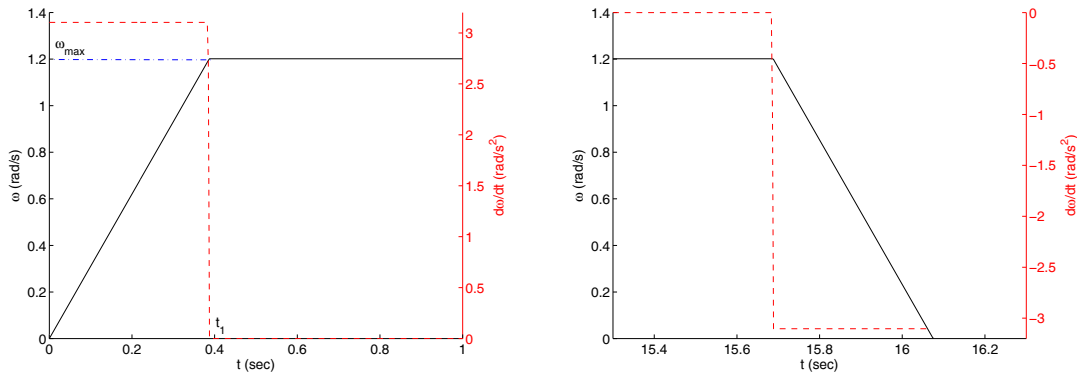

(a) Accelerating wing

(b) Decelerating wing

Fig. 2.7: Commanded linear wing kinematics as a function of time for wing accelerating and decelerating over 0.50 chord-length of travel at a three-quarter span Reynolds number of 15,000. Angular velocity is given by black solid lines and acceleration by red dashed lines. The blue dashed-dot line indicates ω_{max}.

where $G(t)$ smooths the transition from rest to a constant velocity. In the process of smoothing the function, $G(t)$ also changes the scaling, therefore $\alpha(t)$ (Equation 2.11) was used to scale the smoothed function ($G(t)$) to the required angle of attack, as illustrated in Figure 2.8. In Equations 2.10 and 2.11, c is the wing chord, α is the angle of attack for the wing as a function of time, α_{max} is the maximum angle of attack, and a is a user-defined value that controls the sharpness of the function. The value of a must be greater than 1 and is typically less than 200. A low value of a ($a = 50$) results in a very smooth transition, whereas a large value of a ($a = 100$) results in a sharp transition. Figure 2.9 shows the angle of attack as a function of time for two a values.

The time constants t_1 through t_4 are characteristic times chosen by the user to

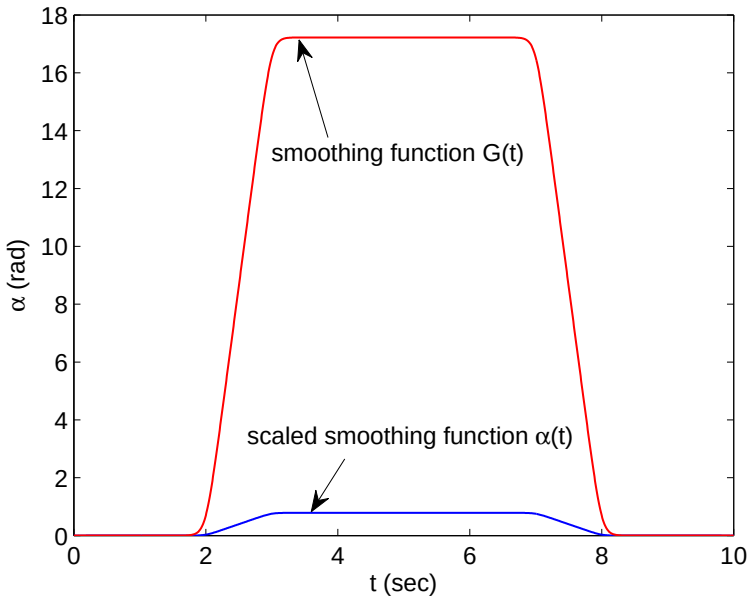

Fig. 2.8: Smoothed kinematics $G(t)$ and scaled kinematics $\alpha(t)$.

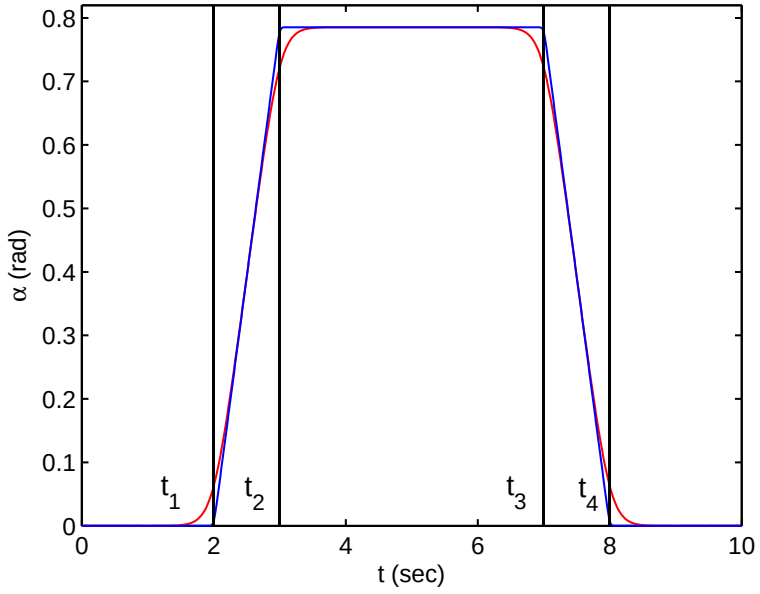

Fig. 2.9: Angle of attack as a function of time for $a = 50$ (red) and $a = 100$ (blue).

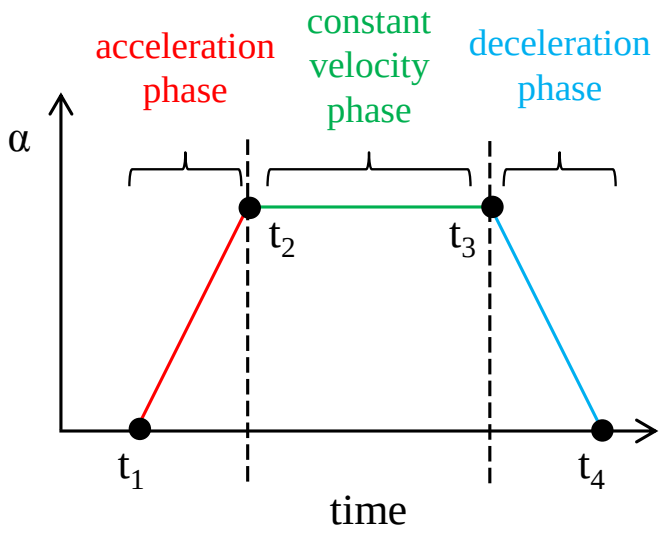

Fig. 2.10: Characteristic times, as defined by Eldredge et al. [68].

fit the prescribed motion in Eldredge's equation. t_1 is the beginning of the pitch-up motion, t_2 is the time at the end of the pitch-up and the beginning of the hold, t_3 is the time at the beginning of the pitch-down and the end of the hold, and t_4 is the end of the motion. In Figure 2.9, $t_1 = 2\,\text{s}$, $t_2 = 3\,\text{s}$, $t_3 = 7\,\text{s}$, and $t_4 = 8\,\text{s}$ and these times are shown by the vertical black lines.

Figure 2.10 is a schematic showing the characteristic times as defined by Eldredge et al. [68], as well as the three phases of the wing stroke as they relate to the rotating wing: the acceleration phase, the constant velocity phase, and the deceleration phase. The three phases are analogous to the phases defined by Eldredge et al. The accelerating phase is analogous to his pitch-up phase, the constant velocity phase is analogous to his hold phase, and the decelerating phase is analogous to his pitch-down phase.

Adjustments were made to Equation 2.10 to apply it to a fixed-pitch rotating

wing stroke. Here, the modified smoothing function is $R(t)$ given in Equation 2.12. $H(t)$ (Equation 2.13) is a scaling function used to scale $R(t)$ such that $R(t)_{max}$ is equal to ω_{max} in a manner similar to Equation 2.11. $H(t)$ is stretched using B (Equation 2.14) such that the function ranges from 0 to ω_{max}. Finally, $\omega(t)$ is the angular velocity where ω_{max} is the maximum angular velocity, given by Equation 2.15.

In rotating wing experiment the wing starts from rest, i.e., $t_1 = 0$, but the smoothing function is not defined for $t_1 = 0$ since the natural log of hyperbolic cosine is undefined at zero. Therefore, t_1 was arbitrarily set to 30% of t_2 and the value of t_2 was unchanged. Thus the value of t_1 determines the wing's acceleration[1]. Increasing the value of t_1 while keeping the value of t_2 the same reduces the time over which the wing accelerates, which in turn increases the jerk. The new smoothing profile is a piecewise function for the three phases of the wing stroke: acceleration, constant velocity, and deceleration. Each phase is now explained in detail:

1. **Acceleration Region** ($t_1 \leq t \leq t_2$) In the acceleration phase of the wing stroke,

$$R(t) = \ln\left[\frac{\cosh(aU_{ref}(t-t_1)/c)}{\cosh(aU_{ref}(t-t_2)/c)}\right] \tag{2.12}$$

$$H(t) = \omega_{max}\left[\frac{R(t)}{\max(R(t))}\right] \tag{2.13}$$

$$B = \frac{\omega_{max}}{[\omega_{max} - \min(H(t))]} \tag{2.14}$$

$$\omega(t) = B[H(t) - \min(H(t))] \tag{2.15}$$

[1]By setting $t_1 = 30\%$ of t_2 the wing is forced to accelerate from rest to a constant velocity only over 70% of the original time. This increases the value of the wing's acceleration and therefore the kinematics are not strictly comparable to the linear velocity profile. This is discussed in further detail in Section 3.4 and Section 4.3.

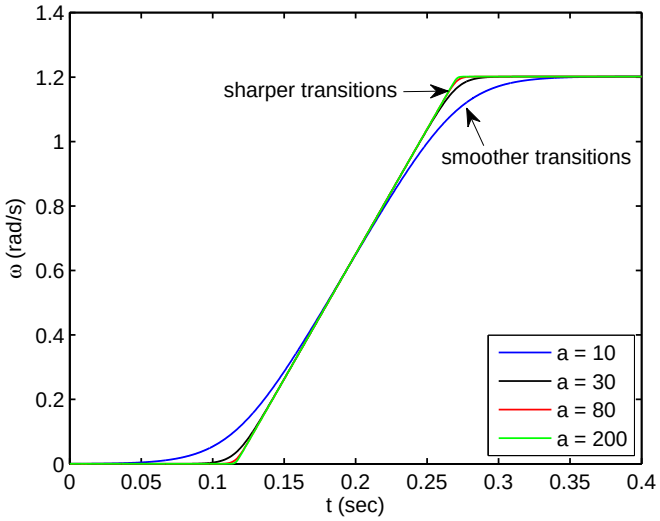

Fig. 2.11: Angular velocity as a function of time for various values of a.

where $R(t)$ smooths the transition from accelerating to constant velocity, and $H(t)$ scales $R(t)$ to achieve the required value of ω_{max}. B (Equation 2.14) is a stretching parameter used to stretch the scaled smoothing function (Equation 2.13), and $\omega(t)$ is the wing's angular velocity as a function of time. In the above equations, U_{ref} is the linear velocity at three-quarter span reference plane on the wing and ω_{max} is the maximum angular velocity. a is a user-defined value that controls the sharpness of the function and has to be greater than 1. The value of a typically ranges from 1 to 200. Past 200 the function does not change much. (This is similar to the sharpness controller defined by Eldredge et al.). Lower values of a lead to smoother transitions and higher values of a lead to sharper transitions. Figure 2.11 shows the angular velocity as a function of time during the acceleration phase for different a values.

The value of a was set to either 30 (heavily smoothed) or 75 (lightly smoothed)

for all the results discussed in this thesis. Figure 2.13 shows the velocity profiles for the two values of a used. It should be noted that, for these wing kinematics, since the desired wing angular velocity increases with Reynolds number so does the value of the wing's acceleration. Therefore, the value of the wing's acceleration depends both on the Reynolds number and the distance over which the wing accelerates from rest to constant angular velocity.

2. **Constant Velocity Region** $(t_2 < t < t_3)$

$$\omega(t) = \omega_{max} \tag{2.16}$$

In this region the angular velocity is constant and equal to ω_{max} as the wing is not accelerating. The value of ω_{max} is determined based on the required three-quarter span Reynolds number and can be found by rearranging Equation 2.9 such that

$$\omega_{max} = \frac{\nu \ Re_{3/4}}{2.15 \ c^2} \tag{2.17}$$

where ν is the kinematic viscosity of water and c is the wing chord.

3. **Deceleration Region** $(t_3 \leq t \leq t_4)$

In order to have a symmetric velocity profile, it was required that the wing decelerate in the same manner that it accelerates. Therefore, the velocity profile for the deceleration phase is the velocity profile from the acceleration phase mirrored and shifted by a value t_3. Equations 2.12 to 2.14 remain unchanged and Equation 2.15 becomes

$$\omega(t) = -B[H(t) - \min(H(t))] \tag{2.18}$$

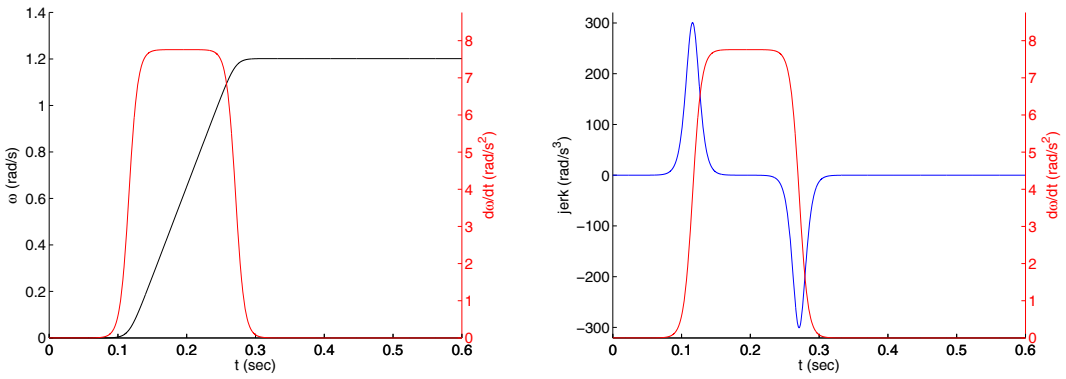

(a) Velocity and acceleration

(b) Acceleration and jerk

Fig. 2.12: Commanded wing kinematics for wing accelerating over 0.50 chord-lengths to a Reynolds number of 15,000.

Figure 2.12 shows the smoothed wing kinematics for a wing accelerating over 0.50 chord-lengths of travel. The angular velocity (ω) is shown by the solid black curve, angular acceleration is shown by the dashed red curve, and jerk is shown by the solid blue curve as a function of time. The velocity profile was heavily smoothed ($a = 30$). Figure 2.13 compares the two smoothing profiles used. The heavily smoothed ($a = 30$) curve is shown in solid red, and lightly smoothed curve ($a = 75$) is shown in dashed blue.

2.3.2 Pitch and Rotation

Previous rotary wing experiments have neglected pitch variations [40, 56], but pitch variations can have a substantial effect on the flow field and lift production. The unique pitching and rotating model described here was designed to bridge the gap between two current models: transient and quasi-steady revolving wings, and

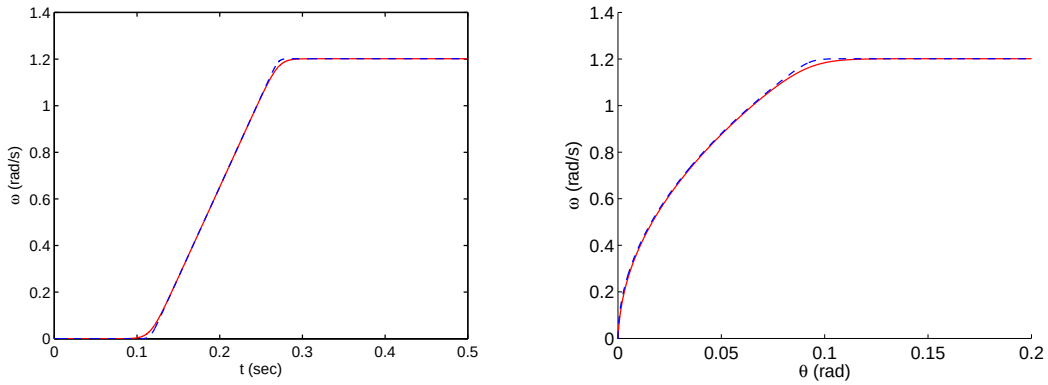

(a) Angular velocity as a function of time (b) Angular velocity as a function of stroke angle

Fig. 2.13: Rotating wing kinematics for a wing accelerating over 0.50 chord-length of travel at a three-quarter span Reynolds number of 5,000 for different values of a.

pitching and plunging wings. This is achieved by including both propeller-like wing rotation about the root and pitch variations about the leading edge.

The wing was driven in both pitch (via the submergible servo motor) and rotation (via the stepper motor) simultaneously. The angle of attack was varied from 0 deg to 45 deg over 1.3 chord-lengths of travel in wing rotation. The commanded wing kinematics are shown schematically in Figure 2.14. The solid red lines indicate wing pitch and the green dashed-dot line indicates wing rotation. The time t_{1c} represents the time required for the three-quarter span reference location of the wing to travel 1.3 chord-lengths, and the wing's angle of attack to change from 0 deg to 45 deg. Wing rotation was initiated when the angle of attack was at its minimum, $\alpha = 0$ deg. The wing was then linearly accelerated to its maximum rotational velocity over 0.25 chord-lengths of travel. The reduced frequency (a measure of the unsteadiness of the flow, defined in Section 1.4) of this motion is $k = 0.59$. Like the

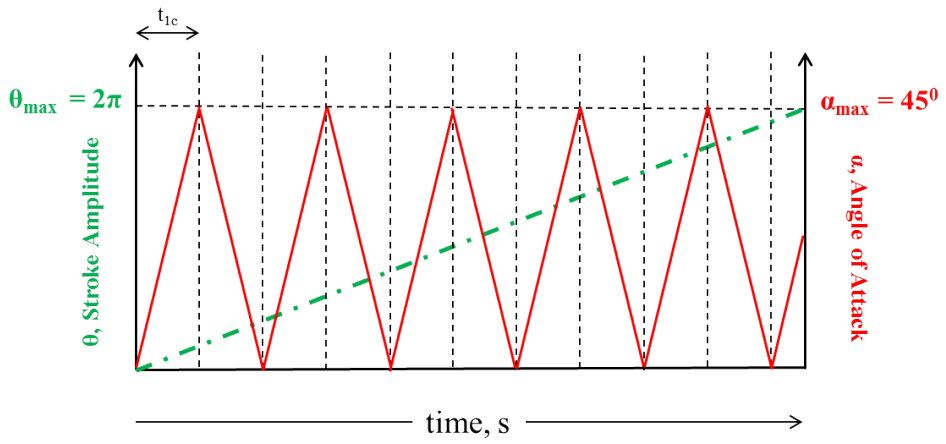

Fig. 2.14: Pitching-and rotating wing kinematics. The stroke angle θ is indicated by the dashed-dot green line and the pitch angle α by the solid red line.

rotating-only wing, the wing was accelerated to an angular velocity corresponding to a Reynolds number of 5,000, in this case over 0.25 chord-lengths of travel.

2.4 Test Matrix

The test matrix is divided into qualitative and quantitative studies. Parameters that were varied for the qualitative rotating wing experiment include angle of attack, angular velocity profile, Reynolds number, wing root geometry (discussed in Section 3.5), and point of dye injection. The experiments described here used the values of these properties given in Table 2.1. Parameters that were varied for the quantitative rotating wing experiments include angular velocity profile, Reynolds number, and wing flexibility. The experiments described here used the values of these properties given in Table 2.2. The parameters that remained unchanged throughout this thesis are:

Table 2.1: Parameter variations for qualitative tests.

Angle of attack	15 deg, 45 deg, 0 to 45 deg[3]
3/4 span Reynolds number	5,000, 10,000
Accelerating over	0.25, 0.50, 0.75, 1.0
Velocity profile	linear, heavily smoothed
Wing root geometry	open root, closed root
Point of dye injection	half span, wing root

Table 2.2: Parameter variations for quantitative tests.

3/4 span Reynolds Number	10,000, 15,000, 25,000
Accelerating over	0.25c, 0.50c, 1.0c
Velocity profile	linear, heavily smoothed, lightly smoothed
Wing flexibility	rigid, half chord flexible

1. Planform shape and thickness

2. Aspect ratio [2]

3. Distance from the axis of rotation to the wing root

[2]Except for Section 3.5.

[3]Pitching-and-rotating wing case.

2.5 Experimental Methods

Qualitative dye flow visualization and quantitative force measurements were performed on a rotating-only and a pitching-and-rotating wing. Each of the methods are described in this section.

2.5.1 Dye Flow Visualization

Dye flow visualization was performed to gain a qualitative understanding of the three-dimensional LEV structures that form on a rotating-only and pitching-and-rotating wing. A mixture of 60% blue food coloring, 20% ethanol, and 20% milk was injected into the flow. When mixed correctly, the dye attains a state of neutral buoyancy and neither sinks nor rises in the quiescent water. A stainless steel hypodermic needle was fixed along the chord of the upper surface of the wing at the root and half span (in separate experiments), injecting dye normal to the leading edge. The flow rate was controlled using a NE-300 syringe pump. The still images shown here were taken from videos, recorded using a Nikon D7000 (HD video at 23 fps). Illumination was provided by a pair of 1000 W halogen lamps. The dye flow rate was balanced between providing sufficient dye to properly visualize the flow structures and preventing an influence on the flow. The best flow rate was determined by a trial and error process. There was a 10 minute wait time between each test to allow the water to settle.

2.5.2 Force Measurements

A submersible ATI Nano17i force transducer capable of measuring three force components up to 25 N with a resolution of at least 1/160 N, and three torque components up to 250 N-mm with a resolution of at least 1/32 N-mm was used for all the force measurements. The force transducer was powered by a low-noise power supply by BK Precision (model number: XLN10014). Force data was acquired using a LabVIEW X-Series 6341 DAQ card at a sampling frequency of 10,000 Hz and exported to MATLAB for analysis. Each test case was repeated five times and the forces were averaged over all runs. The averaged raw force measurements were filtered using a 4th order Butterworth low-pass filter at 30 Hz. Several experiments were performed in order to reduce/improve the signal-to-noise ratio. One of the factors that played a big role in reducing the noise was the power supply used to operate the stepper motor. Figure 2.15 shows the fast fourier transforms (FFT) of the lift force for the two different power supplies tested (noisy and low-noise). Peaks that remained the same regardless of the power supply were at frequencies less than 25 Hz. This indicated that the peaks at higher frequencies were a result of the noise in the power supply. Therefore, a 30 Hz cutoff frequency was chosen for the filter. The raw and filtered lift coefficient is shown in Figure 2.16.

The force measurements collected were reported as wing lift and drag coefficients. The measured lift is acting on the entire wing, so was integrated along the span to account for the span-varying wing velocity. The lift force on the wing is

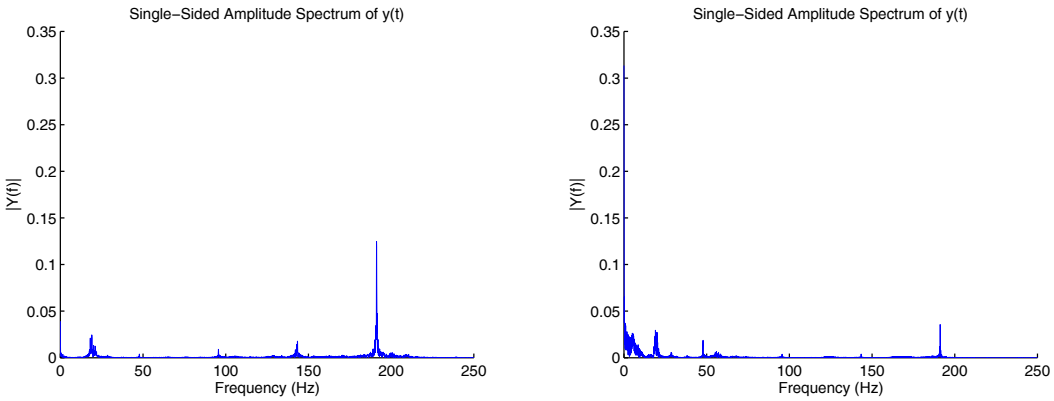

(a) Power supply 1

(b) Power supply 2

Fig. 2.15: Fast fourier transforms of the lift force for two power supplies.

given by

$$L = \int_{r_r}^{r_t} \frac{C_L \rho U_{max}^2 c}{2} \, \mathrm{d}r \tag{2.19}$$

where the velocity is

$$U_{max} = \omega_{max} \, r \tag{2.20}$$

and r_t and r_r are the distances between the axis of rotation and wingtip and axis of rotation and root, respectively. Substituting for U_{max},

$$L = \int_{r_r}^{r_t} \frac{C_L \rho \omega_{max}^2 r^2 c}{2} \, \mathrm{d}r \tag{2.21}$$

$$L = \frac{C_L \rho c \omega_{max}^2}{2} \int_{r_r}^{r_t} r^2 \, \mathrm{d}r \tag{2.22}$$

$$L = \frac{C_L \rho c \omega_{max}^2}{2} \left[\frac{r^3}{3} \right]_{r_r}^{r_t} \tag{2.23}$$

$$L = \frac{C_L \rho c \omega_{max}^2}{6} (r_t^3 - r_r^3), \tag{2.24}$$

and rearranging to solve for C_L,

$$C_L = \frac{6L}{\rho \omega_{max}^2 c (r_t^3 - r_r^3)}. \tag{2.25}$$

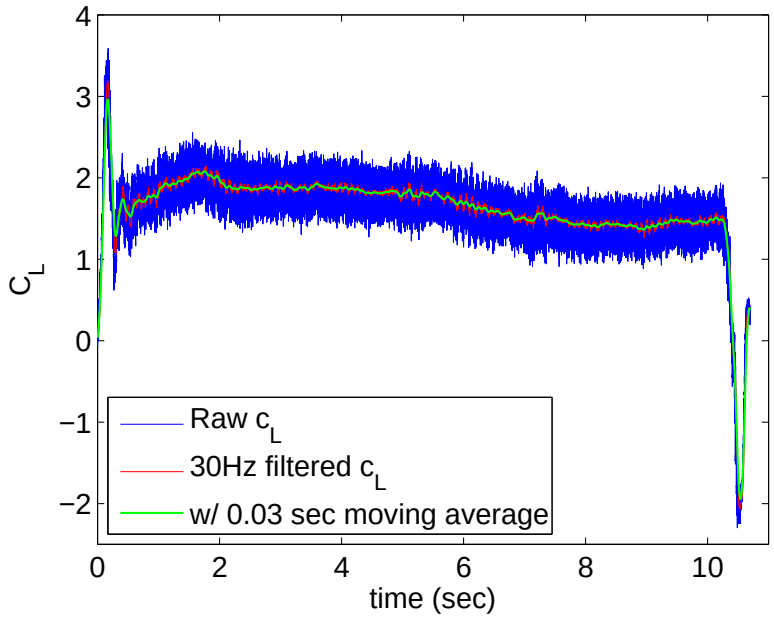

Fig. 2.16: Unfiltered lift coefficient data is shown in blue, low-pass filtered data is shown in red, and the moving averaged data is shown in green for a rigid wing at a $Re = 15{,}000$.

Similarly, the drag coefficient is given by

$$C_D = \frac{6D}{\rho\omega_{max}^2 c(r_t^3 - r_r^3)} \tag{2.26}$$

where L is the lift, D is the drag, ρ is the density of water, ω_{max} is the maximum angular velocity, and r_t and r_r are the distances between the axis of rotation and wingtip and axis of rotation and root, respectively.

After the Butterworth filter was applied to remove the electrical noise, a 0.03 second moving average was applied to the filtered data. A plot of the unfiltered, filtered, and moving average data for one case (rigid wing at $Re = 15{,}000$) is shown in Figure 2.16 as an example.

Table 2.3: RMS error for lift and drag force measurements for the rigid wing.

Re	s_a/c	Velocity Profiles	$\pm C_L$ RMS error	$\pm C_D$ RMS error
10,000	0.50	heavily smoothed	0.91	0.69
15,000	0.25	heavily smoothed	0.28	0.49
		lightly smoothed	0.27	0.33
		linear	0.46	0.39
	0.50	heavily smoothed	0.20	0.32
		lightly smoothed	0.29	0.42
		linear	0.23	0.32
	1.0	heavily smoothed	0.40	0.40
		lightly smoothed	0.25	0.30
		linear	0.17	0.41
25,000	0.50	heavily smoothed	0.13	0.14

Table 2.4: RMS error for lift and drag force measurements for the flexible wing.

Re	s_a/c	Velocity Profile	$\pm C_L$ RMS error	$\pm C_D$ RMS error
15,000	0.50	heavily smoothed	0.17	0.27
25,000	0.50	heavily smoothed	0.08	0.08

Noise in the force measurements was attributed to several factors, such as vibrations in the experimental rig and electrical signal interference due to the power supply. The force transducer was very sensitive and even picked up vibrations of doors closing, people walking, as well as other equipment being used in the lab. Therefore, it was crucial to acquire data only when surrounding environment was quiet. Another factor that introduced noise was the movement of water in the tank, therefore it was important to wait for at least fifteen minutes for the water to settle between tests. The wait time was determined by examining the water and measuring the time it took for the water to settle down completely.

To quantify the error in the force transducer measurements, the RMS error was calculated. RMS error is defined as the square root of the variance and is defined as

$$\text{RMS error} = \sqrt{\frac{\sum_{i=1}^{n}(\text{raw}_{1,i} - \text{filtered}_{1,i})^2}{n}}. \tag{2.27}$$

The RMS error for the various cases tested is summarized in Table 2.3 for the rigid wing and in Table 2.4 for the flexible wing. Heavily smoothed refers to $a = 30$, and lightly smoothed refers to $a = 75$ in the kinematics Equations 2.12 - 2.15. For the Re = 10,000 case, the signal-to-noise ratio is very low and the RMS is much higher than the other cases, therefore, none of the data for this case is shown in the following chapters. An example that demonstrates the bounds of RMS error for lift and drag coefficients for a rigid wing at Re = 15,000 is shown in Figure 2.17. The red curves are $\pm$ the RMS error and imply that 70% of the raw data lie within them.

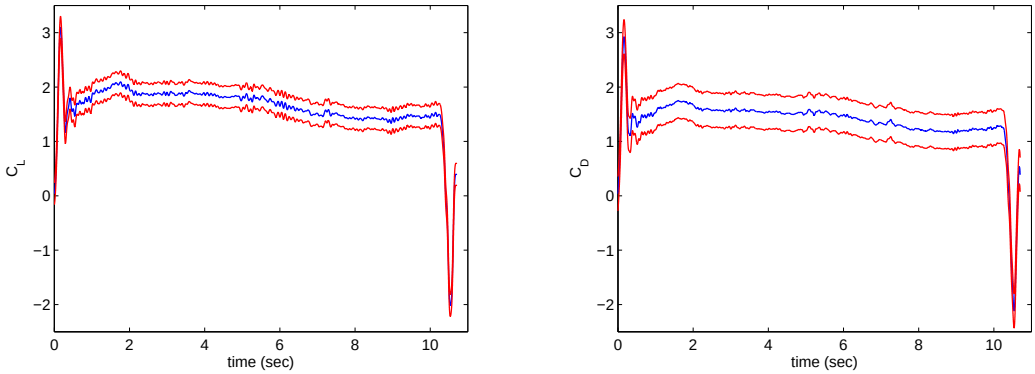

(a) Lift coefficient

(b) Drag coefficient

Fig. 2.17: The lift and drag coefficients are shown in blue for a rigid wing at Re = 15,000, and the upper and lower bounds of the RMS error are shown in red. The wing is accelerating over 0.50 chord-lengths of travel and the velocity profile is heavily smoothed ($a = 30$).

2.6 Summary

Two experimental setups are described here, the rotating-only wing model and the pitching-and-rotating wing model. The rotational motion is controlled by a stepper motor mounted above the water tank. The stepper motor is computer controlled and can be programmed to perform various kinematics. The rotating wing experiment was designed to model the translational phase of the insect wing stroke during hover with a simple set of kinematics. The wing is started from rest and rotates about the root in a propeller-like manner. A submersible servo motor is used to control the angle of attack. For the rotating-only wing model the wing is fixed at a constant angle of attack, whereas for the pitching-and-rotating wing model, the angle of attack was varied from 0 deg to 45 deg. This rig allows

for variation of a wide range of parameters including wing root geometry, angle of attack, Reynolds number, acceleration profiles, velocity profiles, and wing flexibility. Qualitative analysis was performed using dye flow visualization at the wing root and half span. Lift and drag forces were measured using a six-component submersible force transducer. Flow visualization results on the rotating wing described here are presented in Chapter 3, and the force measurement results are presented in Chapter 4.

Chapter 3

Flow Visualization Results

3.1 Overview

Dye flow visualization was used to qualitatively study the evolution of unsteady flow structures on the rotating wing. Several parameters including dye injection location, angle of attack, wing root geometry, velocity profiles, acceleration profiles, Reynolds number, and unsteady variations in pitch were varied to gain insight into their influence on the development of the flow and the leading edge vortex (LEV).

Dye flow visualization is a relatively simple and inexpensive method that can be used to gain a qualitative understanding of three-dimensional flow structures. The experiments discussed here were performed on both a rotating wing at a fixed angle of attack and a pitching-and-rotating wing. Dye was injected at two locations on the wing, at the wing root and the half span. Dye injection at the wing root revealed the presence of a coherent LEV along the leading edge that burst at some location along the wing span. In a separate set of experiments to get a better understanding of the flow structures post-LEV-burst, dye was injected at the half span location on the wing. Dye injection at the half span revealed the presence of a recirculating region form post-LEV-burst.

3.2 Baseline Case

The rotating wing was fixed at an angle of attack of 45 deg. Figure 3.1 shows chordwise views of the wing at multiple points in the wing stroke at a three-quarter span Reynolds number of 5,000. In each of these images, the wing is rotating from left to right in a tank of quiescent water such that the leading edge of the wing appears near the top of the image and the trailing edge near the bottom. A leading edge vortex (LEV) is observed to form as soon as the wing motion begins. A LEV forms when the flow around the leading edge begins to flow from the bottom of the wing to the top, and does so by curling up at the leading edge, forming a vortex.

The presence of spanwise flow is revealed by the motion of the dye from the injection point at the wing root to the wing tip. Figure 3.1 shows four images from early in the wing stroke, illustrating the formation of the LEV and the existence of spanwise flow. (Some dye blobs are also visible, a result of starting the dye injection before the wing motion). The leading edge vortex begins to form almost immediately when the wing begins to rotate, and is already visible by $s/c = 0.64$ as in Figure 3.1(a). Slightly later in the wing stroke (Figure 3.1(b)), a distinctive LEV is observed. Spanwise flow becomes visible along the leading edge as the dye moves from the wing root towards the wing tip. As the wing continues to rotate, the dye continues to convect through the LEV core due to spanwise flow. In Figure 3.1(d) at $s/c = 2.3$, a coherent LEV is observed along the leading edge of the wing near the root. This LEV becomes less well-defined and "bursts" at the quarter span location on the wing (indicated by the black dotted line).

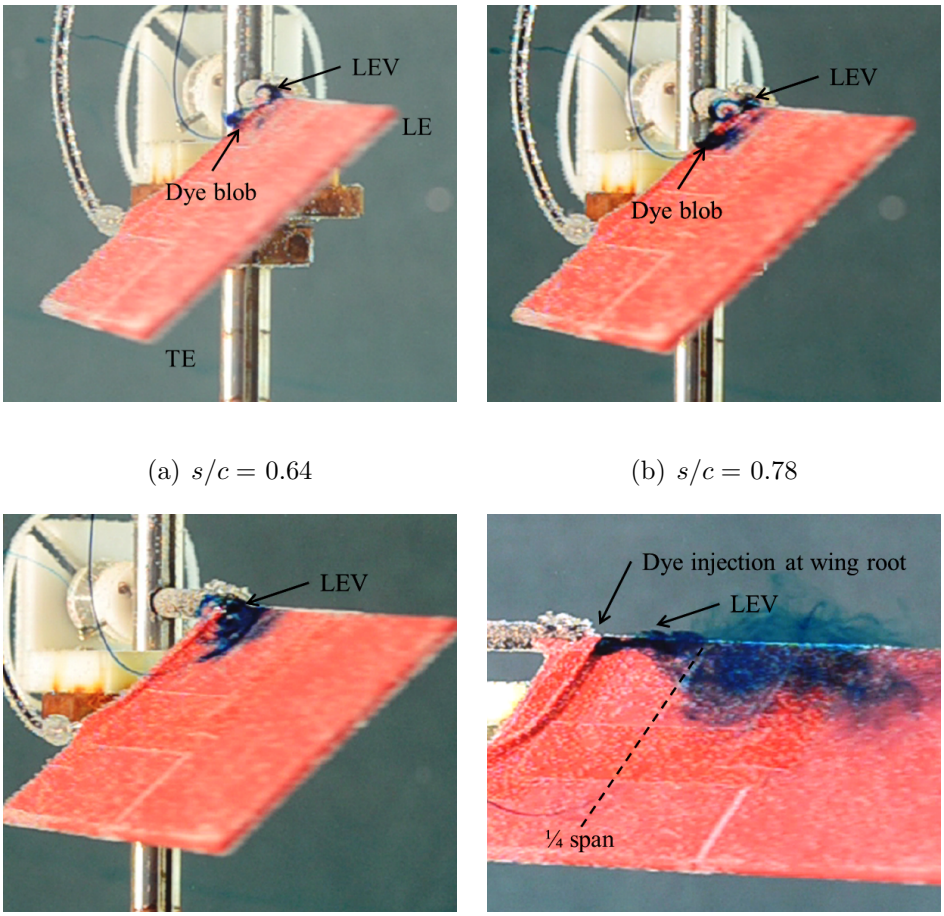

(a) $s/c = 0.64$ (b) $s/c = 0.78$

(c) $s/c = 1.0$ (d) $s/c = 2.3$

Fig. 3.1: Dye injection at wing root. Flow visualization for Re = 5,000 near the beginning of the wing stroke. The velocity profile is linear in time, accelerating over 0.5 chord-lengths of travel.

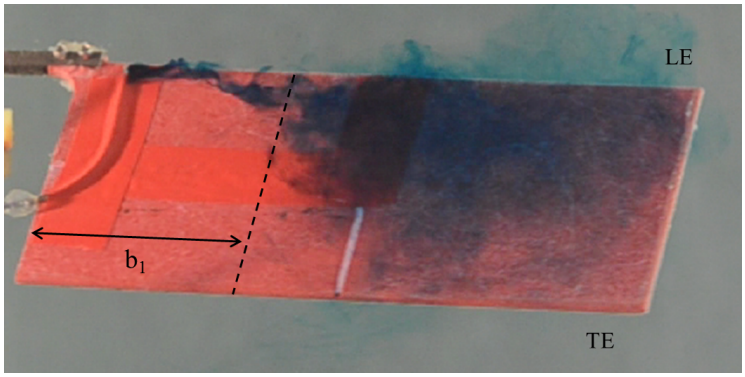

(a) $s/c = 3.9$, $b_1/c = 0.70$

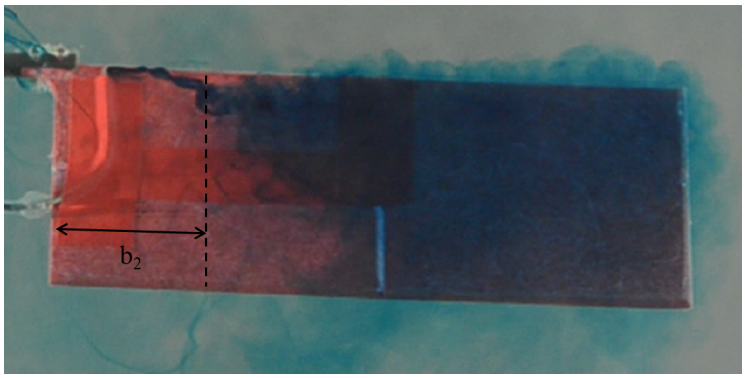

(b) $s/c = 18.6$, $b_2/c = 0.47$

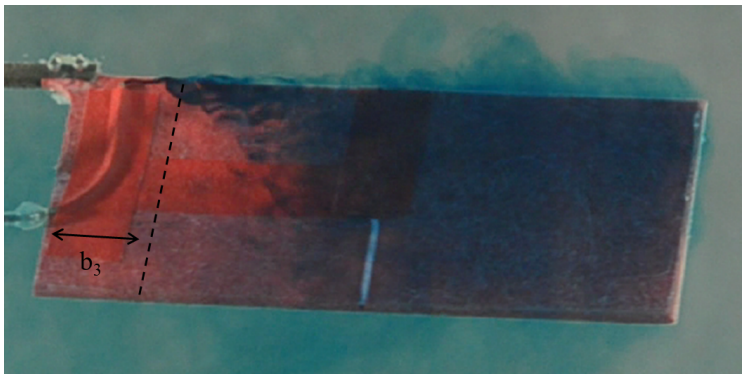

(c) $s/c = 32.3$, $b_3/c = 0.30$

Fig. 3.2: Dye injection at wing root. Flow visualization for Re = 5,000 for three revolutions.

In order to examine the persistence of this LEV structure, the wing was rotated for three revolutions (θ = 1,080 deg and s/c = 40.53). Figure 3.2 shows spanwise views of the wing at a fixed angle of attack of 45 deg for three revolutions at a Reynolds number of 5,000. A coherent LEV was observed to persist near the wing root for all revolutions. The dye injected at the wing root enters the core of the LEV as it forms and travels through the vortex core towards the wing tip. At some point along the wing span, the LEV becomes less coherent and the line of dye becomes less well-defined. When this occurs, the vortex is said to have burst (similar to the formation seen on delta wings, as described in Section 1.4.2). Vortex breakdown occurs when a single LEV is unable to contain all the vorticity present in the flow. The burst point moves inboard as the wing continues to rotate. The distance from the wing root to the point where the LEV burst is defined as b and is then non-dimensionalized by the chord. This ratio is then referred to as b_x/c, where x corresponds to the revolution the wing is in.

In Figure 3.2(a), the wing is in the first revolution, corresponding to a $s/c = 3.9$. Here the vortex preserves its structure and remains coherent for a $b_1/c = 0.70$. As the wing continues to rotate (see Figure 3.2(b) and 3.2(c)), the location at which the vortex bursts moves towards the wing root. This happens because the vorticity increases as the wing continues to rotate for multiple revolutions, and the coherent portion of the LEV is unable to contain the vorticity within itself. The length of the coherent part of the vortex has reduced by $\approx 57\%$ of its original length at $s/c = 32.3$. After the vortex bursts, the flow becomes chaotic and loses the organization it had, though it does retain some circulation.

3.3 Variation of Reynolds Number

All of the qualitative results described in the previous section were obtained at $Re = 5{,}000$. In an effort to begin to understand how Reynolds number affects the leading edge vortex, the Reynolds number was increased from 5,000 to 10,000 and the flow visualization is repeated. Figure 3.3 shows the flow visualization images for three revolutions at a three-quarter span Reynolds number of 10,000. A LEV is still present along the leading edge of the wing, but appears lighter in color as the dye diffuses more quickly when the wing velocity is increased. Similar to the previous case, a coherent LEV is formed which then bursts at some location along the span. However, at this higher Reynolds number, the LEV appears to burst slightly closer to the root. To avoid confusion from the previous case (at $Re = 5{,}000$), the distance from the root to the point of vortex burst is now indicated by e and, similar to the previous case, it is then non-dimensionalized by the wing chord, c. In this case $e_1/c = 0.55$, $e_2/c = 0.39$, and $e_3/c = 0.28$. The length of the coherent part of the LEV is reduced by $\approx 49\%$ of its original length at a $s/c = 32.2$. This reduction in the length of the orderly portion of the LEV is smaller than the $Re = 5{,}000$ case. Since the wing is operating at a higher Reynolds number, the vorticity that forms at the leading edge is higher than the $Re = 5{,}000$ case. The LEV is unable to contain all the vorticity in a single vortex and then bursts forming several small scale vortex structures. This agrees with the findings by Lentink and Dickinson [69].

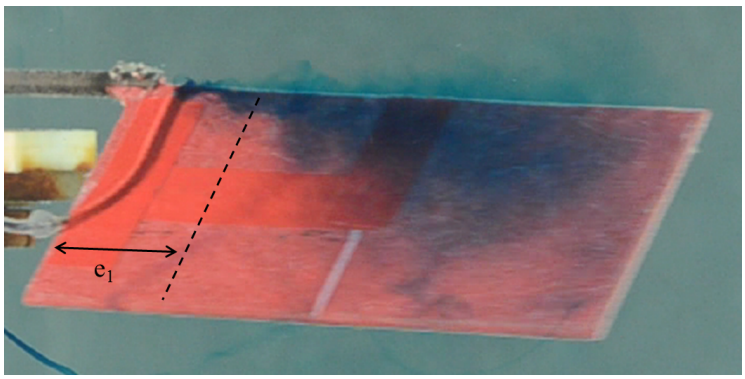

(a) $s/c = 3.2$, $e_1/c = 0.55$

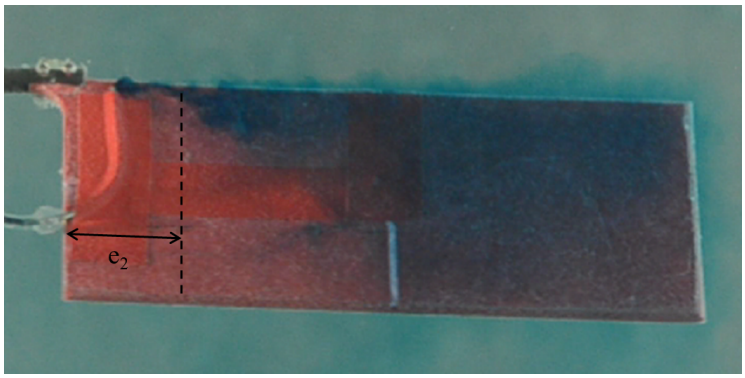

(b) $s/c = 18.5$, $e_2/c = 0.39$

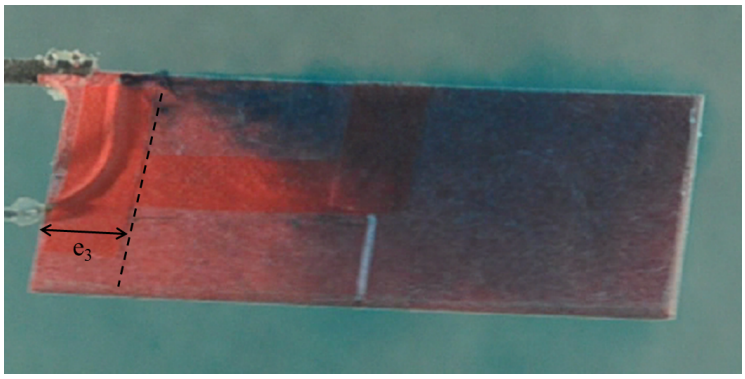

(c) $s/c = 32.2$, $e_3/c = 0.28$

Fig. 3.3: Dye injection at wing root. Flow visualization for Re = 10,000 for three revolutions.

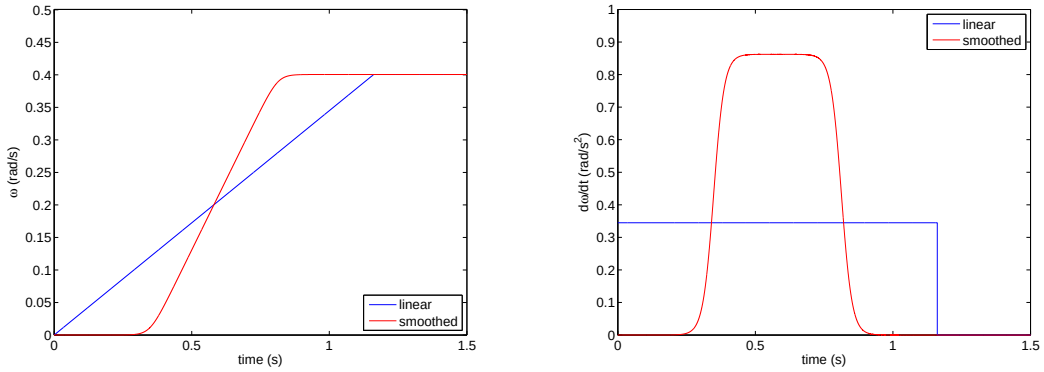

(a) Angular velocity as a function of time (b) Angular acceleration as a function of time

Fig. 3.4: Comparison of the linear and heavily smoothed ($a = 30$) velocity profiles. Wing is accelerating over 0.50 chord-lengths of travel at $Re = 5{,}000$.

3.4 Variation of Velocity Profiles

Another parameter that was varied in this series of rotating wing experiments was the velocity profile. As explained earlier in Section 2.3.1, the smoothed velocity profile has two advantages over the linear profile: 1) it reduces vibrations that may be caused due to instantaneously starting and stopping the wing motion, and 2) it more closely resembles the kinematics of an insect's wing stroke. This set of experiments was performed to determine whether smoothing the velocity profile influenced the LEV development in any way.

For all the cases presented earlier, the wing's velocity was increased linearly (i.e., with a constant acceleration) from rest to a constant velocity. Before comparing the flow structures of the linear profile to that of the smoothed profile, it is important to compare the acceleration profiles for each case. The wing was ac-

celerated over 0.50 chord-lengths of travel with different accelerations[1]. Figure 3.4 shows the two velocity profiles (linear and heavily smoothed) at $Re = 5{,}000$. It can be seen that the slope for the smoothed profile is much steeper than that of the linear profile. The difference in acceleration is a result of setting $t_1 = 30\%$ of t_2 (see Section 2.3.1), thus decreasing the time allowed for the wing to reach its constant velocity, and therefore increasing its acceleration. As a result, the acceleration during the constant acceleration portion of the wing stroke for the linear and smoothed profile is $0.58\,\mathrm{rad/s^2}$ and $0.86\,\mathrm{rad/s^2}$ respectively, which resulted in a difference of approximately 33% between the two cases. Some of the effects of increasing acceleration, i.e., larger vortices and faster shedding vortices (discussed in more detail in Section 3.6.1), are therefore expected.

Figure 3.5 shows chordwise views of the rigid wing accelerating over 0.50 chord-lengths of travel. As soon as the wing begins to rotate, a LEV begins to form at the leading edge as seen at $s/c = 0.19$ in Figure 3.5(a). Soon after, the LEV grows and dye can be seen convecting through the core of the LEV. Similar to the other case described in Section 3.2, spanwise flow is observed from the root to the tip of the wing. Finally, at a later time $s/c = 1.9$ as seen in Figure 3.5(d), a coherent LEV is observed along the leading edge of the wing. This LEV then bursts near the quarter span location on the wing.

The basic structure of the flow is the same as discussed previously and shown in Figure 3.1. The one observable difference between tests with the linear and

[1]This is true for the linear case, however, for the heavily smoothed case the distance over which the wing accelerates was reduced by 30% of the original distance.

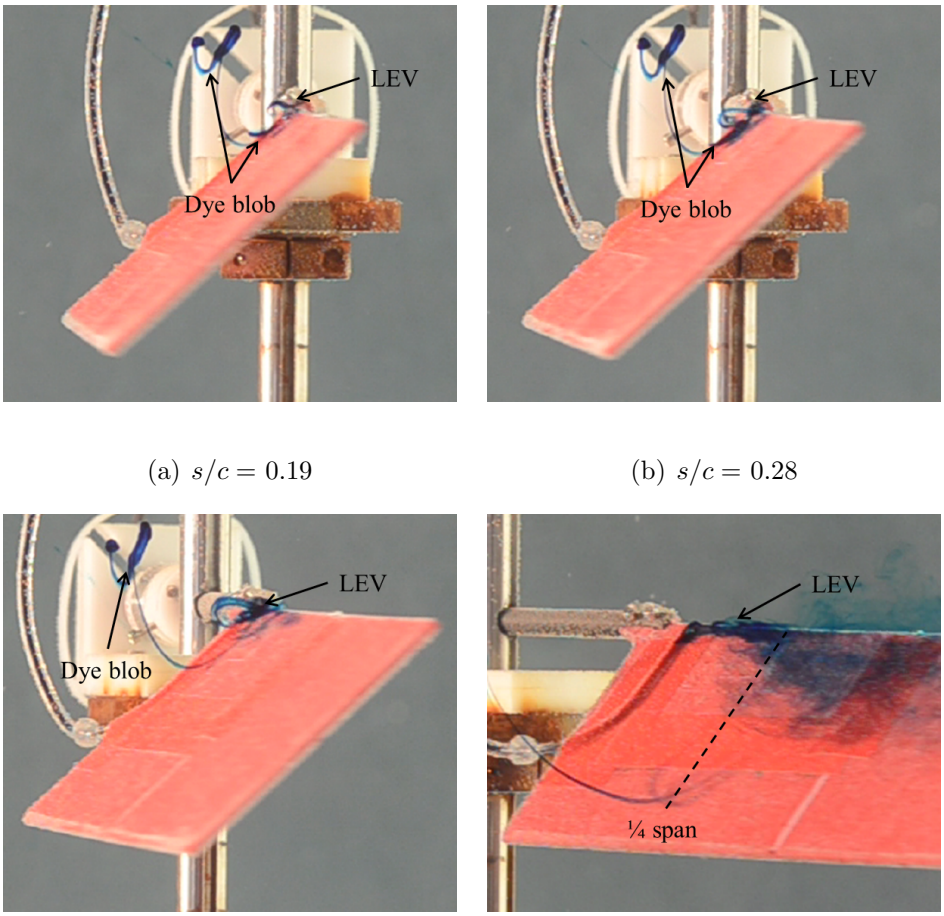

(a) $s/c = 0.19$ (b) $s/c = 0.28$

(c) $s/c = 0.54$ (d) $s/c = 1.9$

Fig. 3.5: Dye injection at wing root. Flow visualization for Re = 5,000 near the beginning of the wing stroke. The velocity profile is heavily smoothed (a = 30), accelerating over 0.5 chord-lengths of travel.

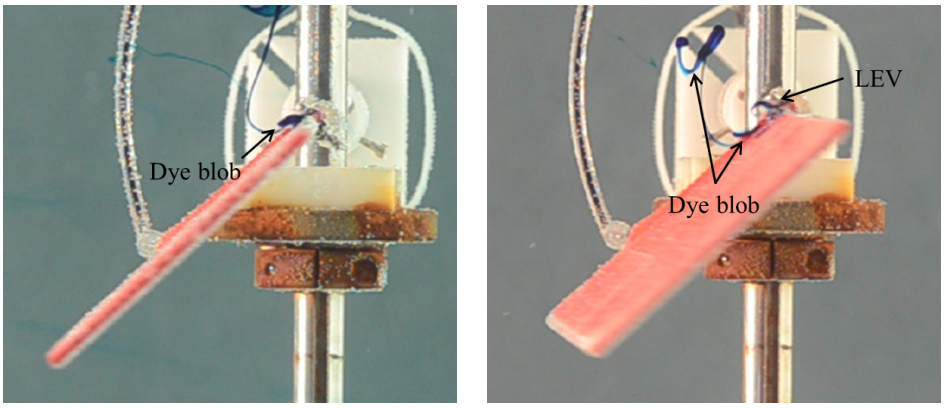

(a) Linear velocity profile (b) Heavily smoothed velocity profile

Fig. 3.6: Comparison of the linear and smoothed velocity profiles at $s/c = 1.9$.

smoothed velocity profiles is that the entire LEV formation process begins much earlier in the wing stroke for the smoothed case ($s/c = 0.19$) when compared to that of the linear case ($s/c = 0.64$). Since the wing is accelerating much faster for the smoothed case, vorticity begins to form earlier and causes the flow to roll into a vortex sooner in the wing stroke. Figure 3.6 compares the linear velocity profile to the smoothed velocity profile at the same point in the wing stroke, $s/c = 1.9$. For the linear case shown in Figure 3.6(a), only a dye blob is present, whereas for the smoothed case, shown in Figure 3.6(b), the LEV has begun to form. The LEV bursts at the quarter-span location for both cases, at $s/c = 1.9$ for the heavily smoothed case, and at $s/c = 2.3$ for the linear case. However, these differences observed maybe due to the higher acceleration rather than the smoothed velocity profile. This set of experiments should be repeated after the acceleration of the two cases are matched.

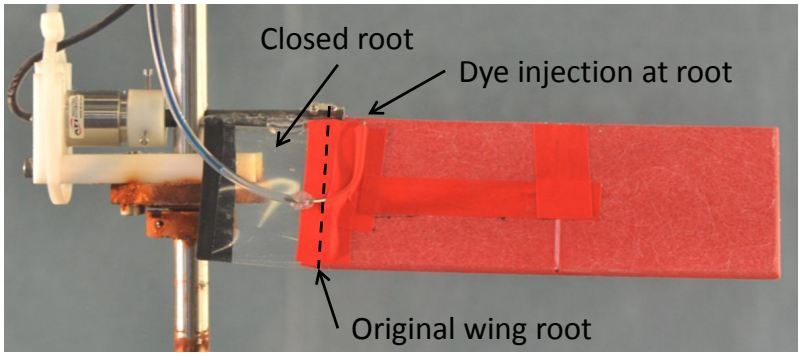

Fig. 3.7: Closed wing root configuration.

3.5 Variation of Wing Root Geometry

The goal of this portion of the study was to qualitatively understand the effect of the wing root geometry on the development and persistence of LEVs in unsteady (early in the wing stroke) and quasi-steady (after multiple revolutions) conditions. The root of the wing was covered in an attempt to study the influence of the root vortices on the LEV. In order to reduce their effect, the wing root was "closed" using book laminate. The book laminate was fixed onto the root of the wing using electrical tape. This removed the gap between the wing and the shaft, as seen in Figure 3.7. The dimensions of this plastic piece were 3 in $\times$ 1.8 in. It is important to note that by covering the wing root, the effective aspect ratio (span/chord) increased from 2 to 2.6. In addition to the change in aspect ratio, the radial location of the wing root also shifts. As a result, dye injection shown here was not performed at the "true" wing root, but in the same location as in previously shown results. The location where the dye is injected will be referred to as the "original" wing root for all the results discussed in this section.

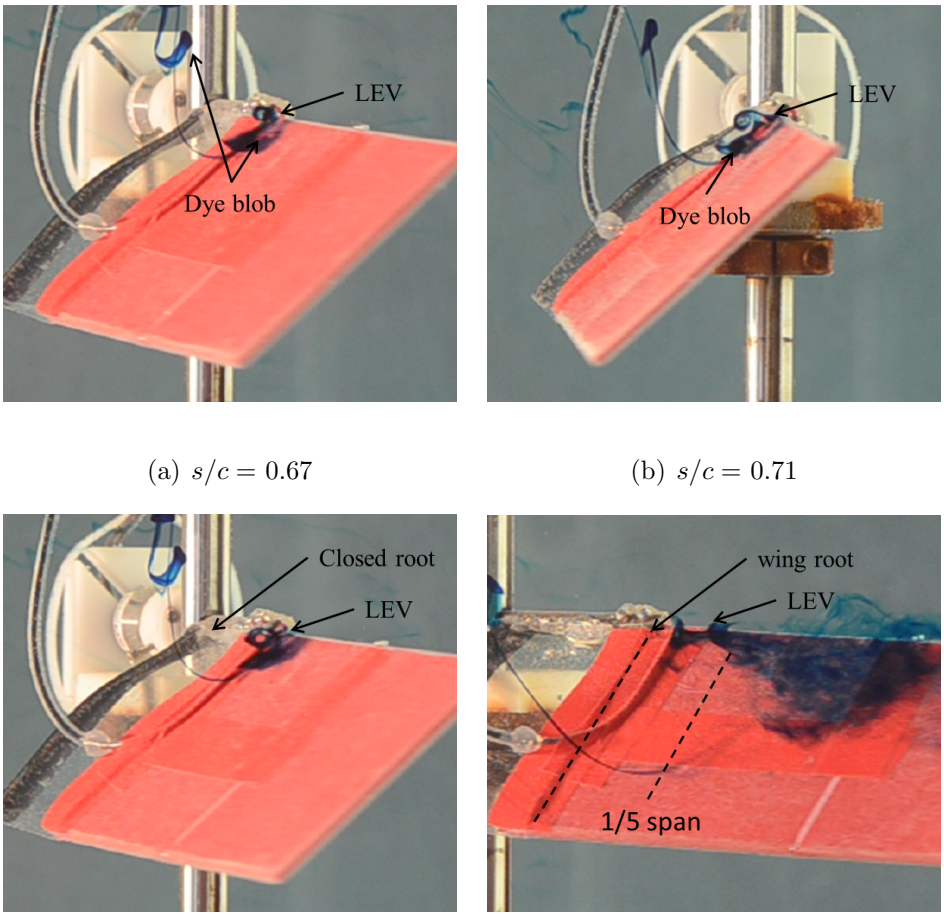

(a) $s/c = 0.67$ (b) $s/c = 0.71$

(c) $s/c = 0.90$ (d) $s/c = 2.2$

Fig. 3.8: Closed root configuration. Dye injection at wing root. Flow visualization for Re = 5,000 near the beginning of the wing stroke. The velocity profile is linear, accelerating over 0.5 chord-lengths of travel.

Figure 3.8 shows chordwise views of the wing at a three-quarter span Reynolds number of 5,000. Images were taken at approximately the same s/c as that of the open root case (see Figure 3.1). The formation of a leading edge vortex is once again observed at $s/c = 0.67$, similar to Figure 3.1(a). The LEV begins to grow, and draws the initial dye blob that was present on the wing into its core (Figure 3.8(b)). Figure 3.8(c) shows the presence of spanwise flow on the surface of the wing. Dye begins to convect through the core of the vortex and moves towards the tip of the wing. Finally, at a $s/c = 2.2$, a coherent LEV is observed along the leading edge, which bursts at approximately 1/5 of the original span. Here the burst appears to take place a little earlier than the open root configuration, where the vortex burst at approximately 1/4 span (shown in Figure 3.1(d)). However, if the book laminate was accounted for, the burst location is approximately a third of the new span, so its difficult to draw any conclusions at this time.

The next step was to determine how long this LEV persisted and whether or not the location where the vortex bursts moved inward as it did on the open-root configuration. Figure 3.9(a) shows the presence of a coherent LEV along the leading edge. The LEV then loses its orderly nature and bursts at $f/c = 0.64$ (measurements based on original span). At a later time, $s/c = 4.5$ (Figure 3.9(b)), the coherent portion of the LEV does not appear to be present. Finally, at a $s/c = 5.0$ shown in Figure 3.9(c), the dye appears to have dissipated almost completely and a LEV is no longer visible. Unlike the open-root configuration, a coherent LEV did not persist for multiple revolutions. This could be a result of closing the root of the wing. Perhaps the vortices at the wing root played a role in preserving the LEV at

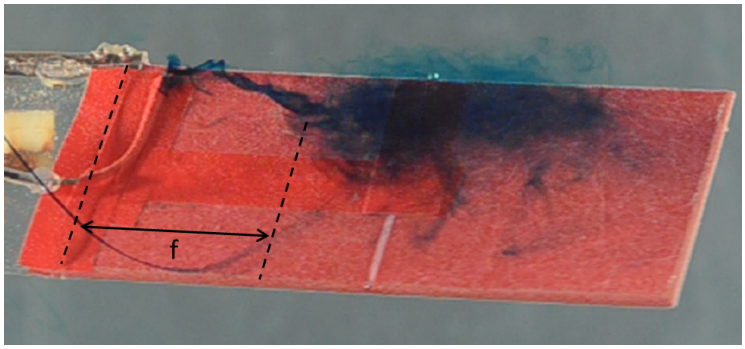

(a) $s/c = 2.8$, $f/c = 0.64$

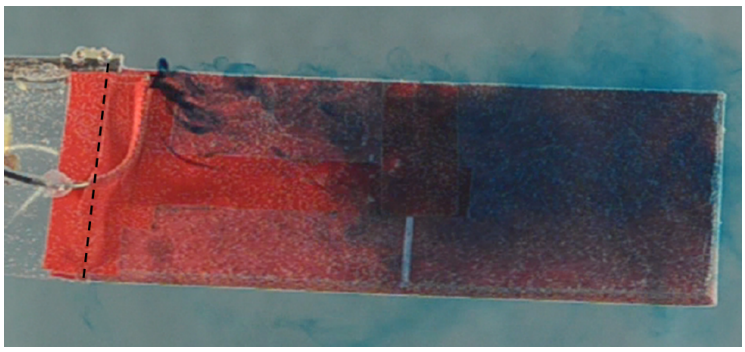

(b) $s/c = 4.5$

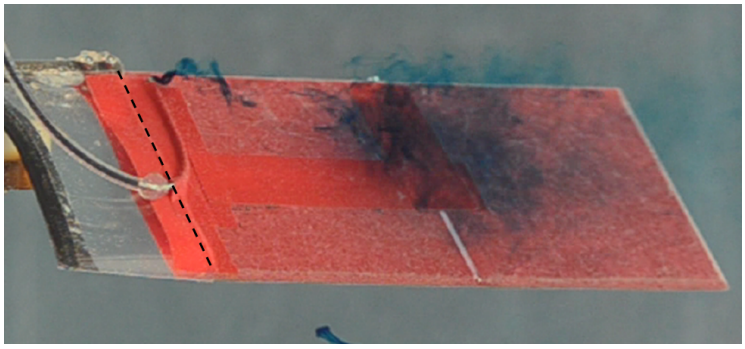

(c) $s/c = 5.0$

Fig. 3.9: Closed root configuration. Dye injection at wing root. Flow visualization for $Re = 5{,}000$.

the leading edge. This could also be a result of not injecting the dye at the true wing root. Perhaps the burst location has moved inboard prior to the dye injection location.

In order to better understand the effect of wing root geometry on the rotating wing, these experiment should be repeated by physically reducing the length of the tygon shaft (refer to Section 2.2) and therefore moving the actual wing root to the central shaft instead of using book laminate. In this manner, the aspect ratio of the wing would remain the same and a direct comparison could be made. Unfortunately, this test could not be completed with the current model since the steel flanged collar prevents mounting the wing close to the shaft at an angle of attack of 45 deg (see Figure 3.7).

3.6 Flow Structures Post-LEV-Burst

For this set of experiments, dye was injected at the half span location to discern the flow structures within the burst LEV. All the images shown here focus on the region outboard of the half span and do not capture the coherent vortex at wing root described earlier. The wing was rotated about the root at a three-quarter span Reynolds number of 5,000. It was accelerated from rest to a constant velocity over 0.50, 0.75, and 1.0 chord-lengths of travel (linear velocity profile) and the flow structures at the three different acceleration profiles are compared.

3.6.1 Variation of Acceleration Profiles

The goal of this study was to determine the effect of wing acceleration on the flow structures within the burst LEV. Figure 3.10 shows chordwise views of the wing corresponding to approximately equal points in the wing stroke (s/c) for different wing accelerations (s_a/c). The three columns represent three different accelerations, $s_a/c = 0.5$, 0.75, and 1.0, and the rows represent the progression in time, given by the number of chord-lengths traveled at three-quarter span, s/c. It is important to note that when the value of s/c is less than s_a/c, the image was captured while the wing was accelerating. When s/c is greater than s_a/c, the image was captured while the wing was rotating at a constant velocity. (I.e., Figures 3.10(a-c,e,f) were captured during the acceleration phase, while the rest were captured during the constant velocity phase).

In all of the cases shown here, the development of the flow on the rotating wing appears to follow a progression—the formation of a vortex at the leading edge, the pairing of shed vortices, and finally, a region of recirculating separated flow, referred to as the burst vortex in Section 3.2. The first row in Figure 3.10 shows the formation of the initial vortex for the three wing acceleration cases. This initial vortex forms at $s/c \approx 0.3$ in all three cases, but the vortices appear to be larger for larger s_a/c or lower wing acceleration values. When the wing is accelerating faster (Figure 3.10(a)) the oncoming flow has to negotiate a sharp turn more quickly, whereas for a lower wing acceleration (Figure 3.10(c)) the flow can make a more gradual turn, therefore resulting in larger vortices for lower wing accelerations. The

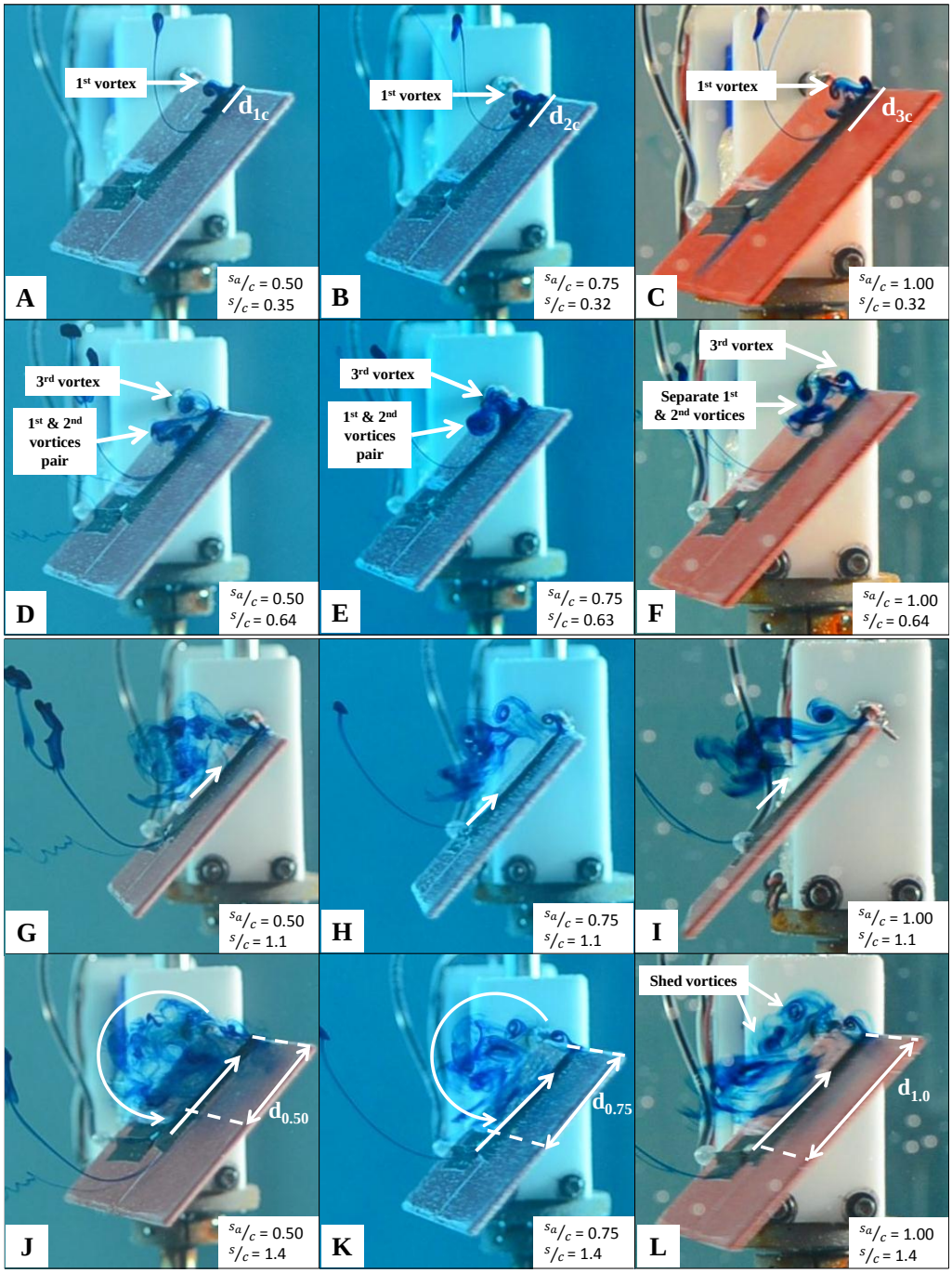
1st vortex
d1c
A
sa/c = 0.50
s/c = 0.35
1st vortex
d2c
B
sa/c = 0.75
s/c = 0.32
1st vortex
d3c
C
sa/c = 1.00
s/c = 0.32
3rd vortex
1st & 2nd vortices pair
D
sa/c = 0.50
s/c = 0.64
3rd vortex
1st & 2nd vortices pair
E
sa/c = 0.75
s/c = 0.63
3rd vortex
Separate 1st & 2nd vortices
F
sa/c = 1.00
s/c = 0.64
G
sa/c = 0.50
s/c = 1.1
H
sa/c = 0.75
s/c = 1.1
I
sa/c = 1.00
s/c = 1.1
d0.50
J
sa/c = 0.50
s/c = 1.4
d0.75
K
sa/c = 0.75
s/c = 1.4
Shed vortices
d1.0
L
sa/c = 1.00
s/c = 1.4

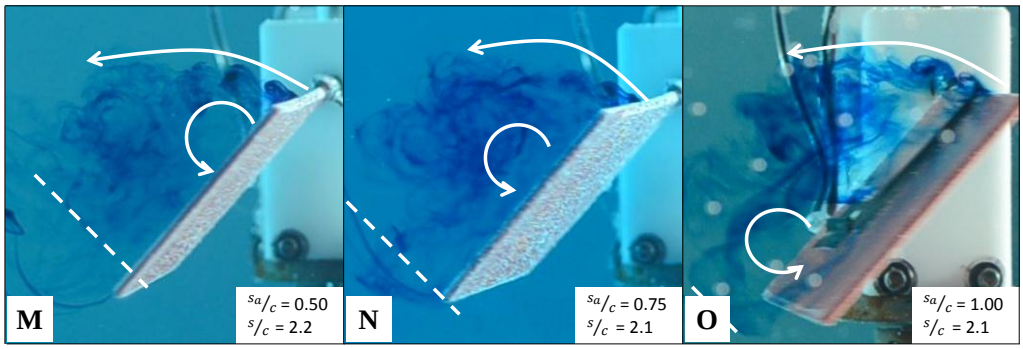

Fig. 3.10: Dye flow visualization of a rotating wing at a fixed angle of attack of 45 deg.

diameter of the initial vortex is defined as d and is then non-dimensionalized by the wing chord. This ratio is then referred to as d_{xc}/c, where x corresponds to the column the wing is in (i.e., the distance over which the wing is accelerated). The physical size of the vortex in the third column, $d_{3c}/c \approx 0.21$, is greater than that in the first column, $d_{1c}/c \approx 0.16$.

In the second row of Figure 3.10, the first vortex has shed and a second vortex has also formed and shed. As the third vortex forms, the first and second shed vortices pair and begin rotating about a common point. The images taken at $s/c \approx 0.6$ (Figure 3.10(d-f)) illustrate this process, though the flow appears to be at a slightly different stage for each acceleration case. In Figures 3.10(d,e) ($s_a/c = 0.50$ and 0.75), the first and second vortices have paired. In Figure 3.10(f) ($s_a/c = 1.0$), these vortices are about to pair, but have not done so yet. Note that Figure 3.10(d) was captured during the constant velocity phase and Figures 3.10(e,f) were captured while the wing was accelerating.

Another interesting feature seen in Figure 3.10(d) is an S-shaped structure.

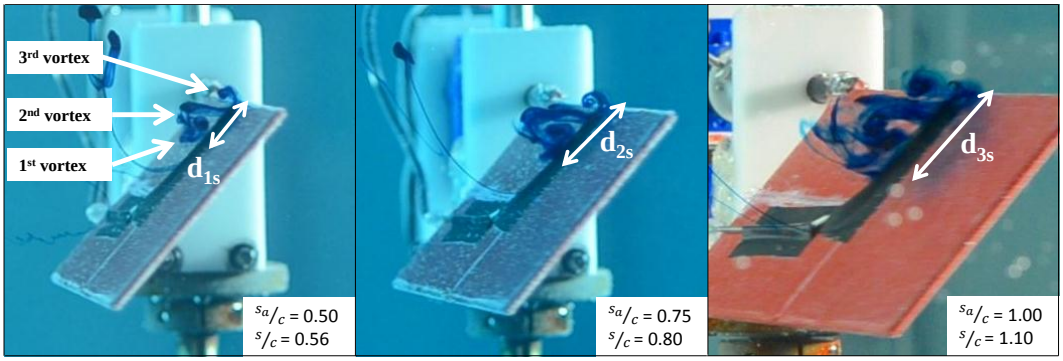

Fig. 3.11: S-shaped flow structure observed in all three acceleration cases soon after the end of the wing's acceleration phase. $d_{1s}/c \approx 0.26$, $d_{2s}/c \approx 0.31$, and $d_{3s}/c \approx 0.43$.

This structure appears soon after the wing reaches the constant velocity phase for all three acceleration cases, as shown in Figure 3.11. For the $s_a/c = 0.50$ case, the S-shaped structure consists of the first and second shed vortices, which will soon pair (see Figure 3.10(d)), and a newly-formed third vortex. The length of the S appears to increase as the wing acceleration decreases. The value of $d_{3s}/c \approx 0.43$ for $s_a/c = 1.0$, while $d_{1s}/c \approx 0.26$ for $s_a/c = 0.50$. Just past this point in the wing stroke, the vortices at the bottom of this structure begin to recirculate, causing them to move along the surface of the wing towards the leading edge.

Returning to Figure 3.10, rows 3 and 4 (corresponding to $s/c \approx 1.1$ and 1.4), illustrate the path taken by the shed vortices. The vortices that formed at the leading edge initially traveled downstream over the wing, but eventually reverse direction and move along the upper surface of the wing towards the leading edge, forming a region of recirculating flow over the upstream half-chord. This counter-

clockwise motion is indicated by the arrows in row 4. Vortices are shed off the leading edge and travel approximately half-way down the chord, where they contact the wing surface. It can be seen that the precise distance traveled prior to impact depends on the acceleration. For $s_a/c = 0.50$ shown in Figure 3.10(g), the shed vortices impact the wing upstream of mid-chord, but at $s_a/c = 1.0$ shown in Figure 3.10(i) they impact just downstream of mid-chord. When these shed vortices collide with the wing, they deform. Interaction with the solid boundary causes these now-deformed vortices to move along the wing towards the leading edge, thus forming a region of recirculating flow.

Figure 3.12(a) shows the flow structures visible when dye is injected at the wing root, and Figure 3.12(b) shows a chordwise view of the flow structure at the half span, indicated by the solid yellow line in Figure 3.12(a). Both images are from different s/c but the flow structure does not change significantly after the LEV bursts. Figure 3.12(b) indicates that after the vortex bursts at some location along the span, it lost its coherent structure but retained some recirculation, and forms a recirculating separated region. This recirculating region contains vortices that were previously shed, as well as new vortices that continue to shed as the wing rotates.

Later in the wing stroke, when $s/c \approx 2.1$ (row 5 of Figure 3.10), the flow is fully-separated with a large recirculating region. The size of the recirculating region increases with s_a/c. When $s_a/c = 0.50$ (Figure 3.10(m)), the recirculating region covers approximately 75% the wing chord and has not quite reached the trailing edge. When $s_a/c = 0.75$ (Figure 3.10(n)), the recirculating flow extends to the trailing edge. For $s_a/c = 1.0$ (Figure 3.10(o)), the recirculating region is past the

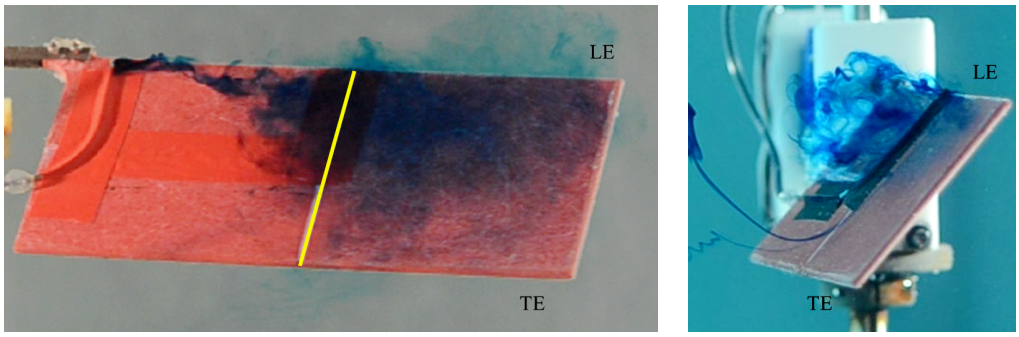

(a) $s/c = 3.9$ (b) $s/c = 1.4$

Fig. 3.12: Comparison of flow structures.

trailing edge. This recirulating region, i.e., the burst vortex, covers the outboard portion of the wing as seen in Figure 3.1.

3.6.2 Variation of Angle of Attack

The experiment described in Section 3.6.1, was repeated with a fixed angle of attack of 15 deg. Figure 3.13 shows the chordwise views of flow visualization images for the different wing accelerations (columns) throughout the wing stroke (rows). The first row in Figure 3.13(a-c) shows the first shed vortex at the half span, and the second vortex starting to form. Very little dye is entrained in the first vortex at $s_a/c = 0.50$ (Figure 3.13(a)), but this vortex is more visible in the image taken at $s_a/c = 0.75$ (Figure 3.13(b)). In Figure 3.13(c) a dye blob is visible in addition to the initial vortex. This blob is a result of injection of some dye before the start of the wing motion. Overall, it appears that the vortices formed at $\alpha = 15$ deg are smaller than those that form at $\alpha = 45$ deg, and travel downstream over the surface of the wing rather than lifting off the wing's surface as they do at $\alpha = 45$ deg.

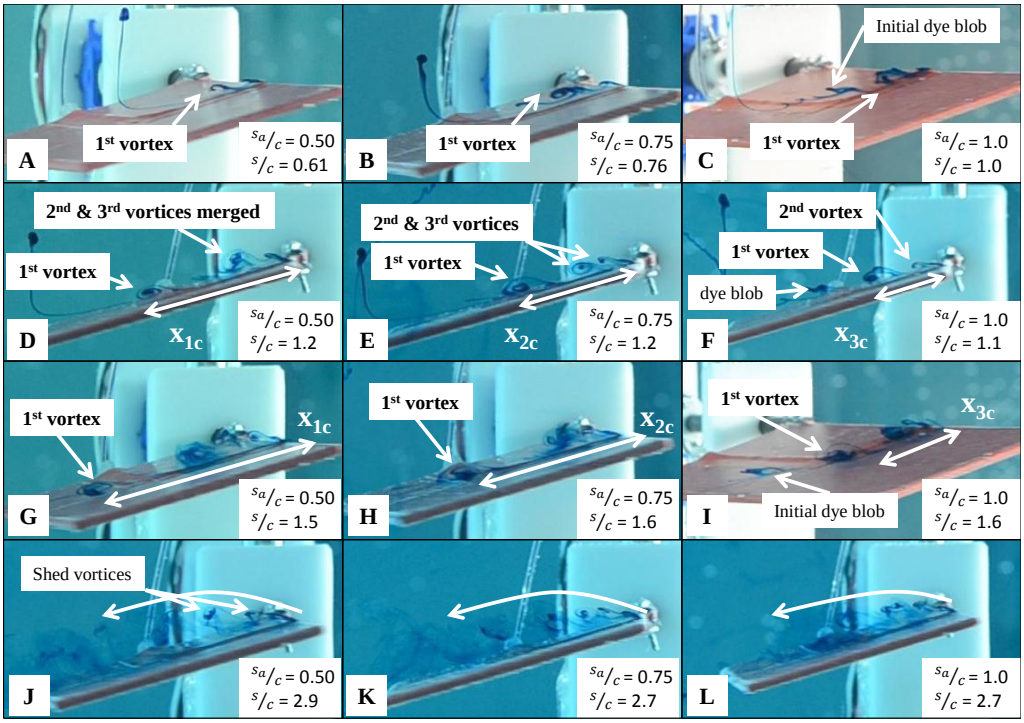

Fig. 3.13: Dye flow visualization of a rotating wing at a fixed angle of attack of 15 deg.

In Figures 3.13(d-f)), at $s/c \approx 1.2$, all three cases show different development stages of the flow structures on the wing. In each case, the first vortex has shed and traveled to a different location, x_c, downstream over the surface of the wing. At this point in the wing stroke, the shed vortex has moved more than half the chord-length downstream in Figure 3.13(d) at $s_a/c = 0.50$, but only about one-third of a chord-length in Figure 3.13(f). Furthermore, the development of the next few vortices vary amongst the acceleration cases.

Figure 3.13(d) ($s_a/c = 0.50$, $s/c = 1.2$), shows the first vortex at $x_{1c}/c \approx 0.55$, while the subsequent vortices have shed and merged with each other. In the second acceleration case, $s_a/c = 0.75$ (Figure 3.13(e)), the initial vortex has traveled to

$x_{2c}/c \approx 0.49$ and the next few vortices have formed, but have not yet merged. In the third case where $s_a/c = 1.0$ shown in Figure 3.13(f), the first vortex has traveled a distance $x_{3c}/c \approx 0.32$, and the next vortex has begun to form. The differences in the development and migration of the vortices observed here suggest that the wing acceleration can affect the timing of vortex formation and shedding on a rotating wing at a 15 deg angle of attack.

Later in the wing stroke, at $s/c \approx 1.6$ (shown in Figures 3.13(g-i)), the first vortex has moved further along the wing in each of the three acceleration cases. This shed vortex appears to move downstream faster for slower wing accelerations. The velocities (relative to the wing itself) at which the vortex travels downstream between 1.2 and 1.6 chord-lengths of wing travel are approximately $0.039\,\mathrm{m\,s^{-1}}$, $0.030\,\mathrm{m\,s^{-1}}$, and $0.014\,\mathrm{m\,s^{-1}}$ for acceleration over 0.50, 0.75, and 1.0 chord-lengths of travel, respectively. At $s/c \approx 1.6$, the locations of the initial vortices are $x_{1c}/c \approx 0.77$, $x_{2c}/c \approx 0.64$, and $x_{3c}/c \approx 0.43$. Unlike the 45 deg angle of attack case, there does not appear to be an obvious recirculating region present.

The fourth row of Figure 3.13(j-l) illustrates the flow structure for the three different acceleration cases much later in the wing stroke, at $s/c \approx 2.7$. In all three cases, there is a trail of shed vortices extending along the surface of the wing from the leading edge to the trailing edge without forming a recirculating region.

3.7 Pitching and Rotating Wing

The rotating wing experiment was extended to include unsteady variations in pitch at a Reynolds number of 5,000. The angle of attack of the wing was varied from 0 deg to 45 deg over 1.3 chord-lengths of travel at the three-quarter reference plane in wing rotation, using the underwater servo motor as described in Section 2.3.2. The dye was injected at the half span location. As seen from the rotating wing experiments, a coherent LEV is present along the leading edge but bursts prior to reaching the half span location on the wing. All the images in this section show the flow structures on the outboard half of the wing.

Results of dye flow visualization for the pitching and rotating wing case are given in Figure 3.14. In this figure, the '+' superscript on α denotes that the wing's angle of attack is increasing. The '-' superscript denotes a decreasing angle of attack. The angle of attack given here was calculated by correlating the known pitch kinematics with the stoke angle obtained from the encoder.

Figure 3.14(a) shows the wing pitching up near the beginning of the wing stroke. The wing executed one pitch stroke (0 to 45 to 0 deg) before wing rotation began, resulting in excess dye present in the background and a dye blob on the wing. At this point in time, the flow looks much like it did near the start of the $\alpha = 15$ deg rotating-only wing stroke, as shown in Figure 3.13(d-f). Flow is largely along the surface of the wing, and contains vortices that move downstream towards the trailing edge.

In Figure 3.14(b), the wing stroke has progressed to $\alpha \approx 18$ deg, $s/c = 0.34$.

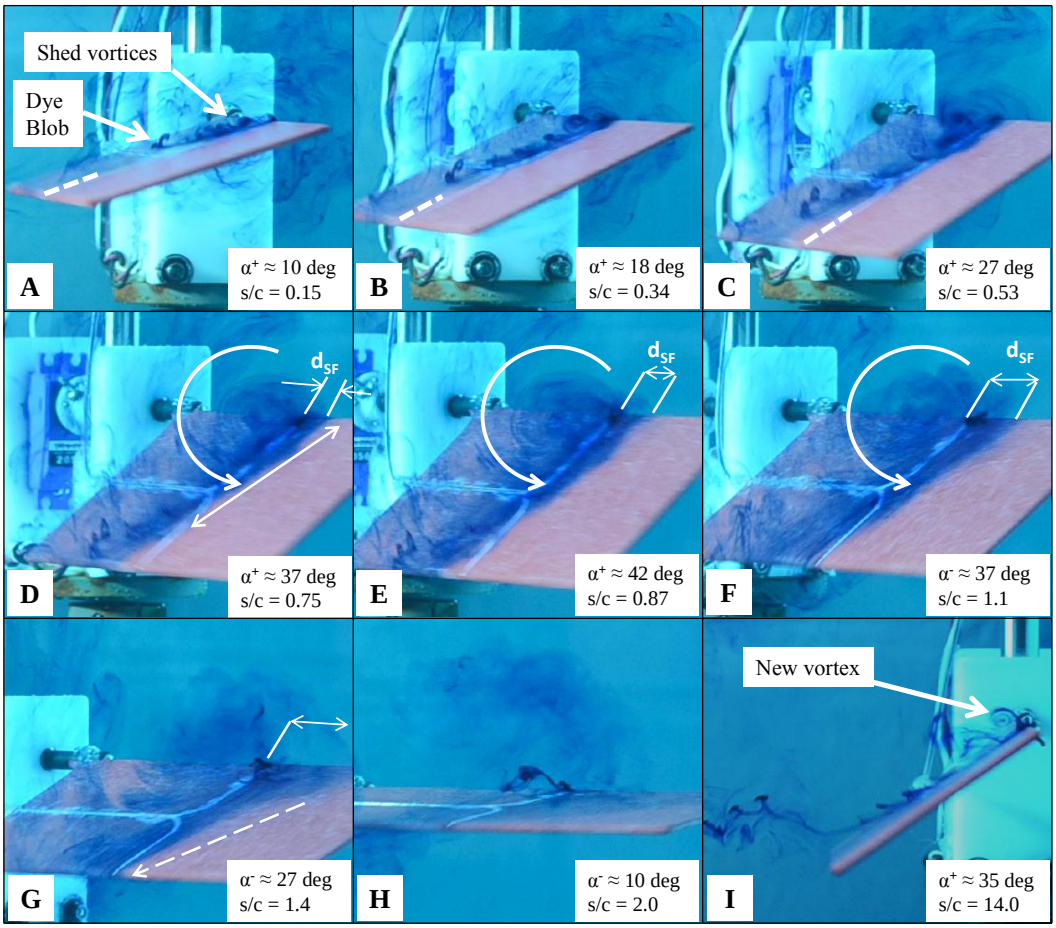

Fig. 3.14: Dye flow visualization of a pitching and rotating wing.

Flow has continued along the surface of the wing and curves towards the wing root on the downstream half of the chord. The surface of the wing has a white line from leading to trailing edge at half span. This physical mark is highlighted by the dashed white line in Figure 3.14(a-c) to illustrate the extent of spanwise flow. Near the leading edge, vortices have formed, and a region of recirculating flow begins to form around them. Later in the wing stroke, at $s/c = 0.53$, this recirculating region has grown larger and flow along the trailing half of the wing has continued towards the trailing edge and root.

In Figure 3.14(d), the recirculating region has grown further and is now more well defined. In this view, the white line on the wing is more obvious, and it is clear that dye has moved toward the wing tip at the leading edge and towards the wing root at the trailing edge. As the wing stroke progresses, dye near the leading edge continues to move towards the tip. The distance of the dye along the leading edge from the half span location is defined as d_{SF}. In Figure 3.14(e), the distance d_{SF} has increased, and continues to do so in Figure 3.14(f). It also becomes clear that the dye at the trailing edge is now moving towards the wing tip.

Figure 3.14(e) shows the flow at $\alpha \approx 42\,\text{deg}$, near the maximum angle of attack. It was previously noted that on a rotating-only wing at $\alpha = 45\,\text{deg}$, the flow is fully separated from the wing and recirculates in a burst vortex. In the pitching and rotating setup, the recirculating region near the leading edge is on the surface of the wing and the flow along the back half of the wing remains intact. For the pitching and rotating wing, however, α does not remain constant, but decreases immediately upon reaching $\alpha_{max} = 45\,\text{deg}$. When the wing begins to pitch down, the structure of the flow begins to break up, and the recirculating region is less defined as shown in Figure 3.14(f).

The images in Figure 3.14(f-h) were taken as the wing pitched down. As α decreased, the trailing edge of the wing rose, and the region of recirculating flow near the leading edge was ejected from the wing's surface. In Figure 3.14(g), any organization that the recirculating region might have previously had has largely vanished, and by Figure 3.14(h) only a cloud of dye remains well above the wing. It is interesting to note that this cloud of dye has moved vertically off of the wing

rather than downstream towards the trailing edge. Additionally, the newly injected dye has also risen off of the wing's surface.

Finally, Figure 3.14(i) shows the flow much later in the wing stroke and at $\alpha \approx 35\,\text{deg}$. There is less dye in the flow and thus the large-scale structures are not visible. At this point, a new vortex has formed and flow has reattached to wing's surface downstream of this new vortex.

3.8 Summary

This chapter presented results for dye flow visualization experiments performed on a rotating-only wing and a pitching-and-rotating wing, with a focus on the three-dimensional flow structures that formed on a fixed-pitch rotating wing. When dye was injected at the wing root, a coherent LEV was observed along the leading edge which then burst at the quarter span location along the wing, very similar to the LEV seen on delta wings. As the wing continues to rotate, the location where this LEV becomes less well-defined and the burst point moves inboard. When the LEV burst, the flow became chaotic and recirculating flow covered the remaining outboard portion of the wing. The small scale flow structures in burst vortex were not clearly visible when dye was injected at the wing root. In order to get a better understanding of the flow structures within the burst LEV, dye was then injected at the half span location.

Dye flow visualization on the rotating-only wing at half span was performed at two fixed angles of attack of 45 deg and 15 deg. The distance over which the

wing was accelerated was varied and the flow structures were compared for three different acceleration values. At a fixed angle of attack of 45 deg, the value of the wing's acceleration affected vortex size. Lower acceleration values resulted in larger vortices. Vortices shed and formed a recirculating region, which provided new insight into the flow structures post-LEV-bust. At a fixed angle of attack of 15 deg, the acceleration affected the speed of which vortices were shed rather than vortex size and a recirculation region was absent.

Unsteady variations of pitch were introduced to the rotating-only wing. Dye flow visualization was performed at the half span location on the wing. At low angles of attack, the flow structures were similar to those observed on the rotating-only wing at an angle of attack of 15 deg. At high angles of attack, however, a large recirculation region near the leading edge was observed, with attached flow behind it.

Chapter 4

Force Measurements Results

4.1 Overview

This chapter presents quantitative results from investigating the lift and drag produced on a rotating-only wing at a fixed angle of attack of 45 deg. Force measurements were used to quantify the aerodynamic forces produced by the flow structures discussed in the previous chapter. Unsteady force measurements were acquired for a 720 degree wing stroke. As previously described, the six-axis force transducer has a capacity of 25 N in the x, y and z directions with a rated resolution of 1/160 N, as well as a torque capacity of 250 N-mm with a rated resolution of 1/32 N-mm. The measured forces were normalized using

$$C_L = \frac{6L}{\rho\omega_{max}^2 c(r_t^3 - r_r^3)} \tag{4.1}$$

$$C_D = \frac{6D}{\rho\omega_{max}^2 c(r_t^3 - r_r^3)} \tag{4.2}$$

as described in Section 2.5.2, where ω_{max} is the maximum angular velocity, and r_t and r_r are the distances between the axis of rotation and wingtip and axis of rotation and root, respectively. As described in Section 2.5.2, the lift and drag signals were filtered and a 0.03 second moving average was applied. Several parameters including velocity profiles, acceleration profiles, Reynolds number, and wing flexibility were varied.

4.2 Baseline Case

To better understand the force history of the rotating wing, a baseline case is first discussed in detail. Figure 4.1 shows the coefficients of lift and drag with respect to the stroke-to-chord ratio (s/c) for a wing accelerating over 0.50 chord-lengths of travel at a three-quarter span Reynolds number of 15,000[1]. The velocity profile was heavily smoothed ($a = 30$), and is shown in Figure 4.2. In both Figures 4.1 and 4.2 the first vertical black line corresponds to the transition to constant velocity, the second vertical line marks the end of the first rotation, and the third line represents the beginning of deceleration.

The coefficients of lift and drag initially overshoot, then undershoot, increase again, and eventually level off to an intermediate value for the remainder of the first revolution. After the wing enters the second revolution, the coefficients begin to decrease again before leveling out to a second value until the wing begins to decelerate. The acceleration region and the constant velocity region are explained in further detail to better understand the behavior of the force coefficients.

4.2.1 Acceleration Phase

Figure 4.3 shows the lift and drag coefficients early in the wing stroke, i.e., the acceleration phase of Figure 4.1. The vertical black line indicates the end of the acceleration phase and the beginning of the constant velocity phase. During this

[1]The Reynolds number for the baseline case described here is much higher than the baseline case described in the previous chapter. This is because at low Reynolds numbers, the signal-to-noise ratio of the force transducer was very low.

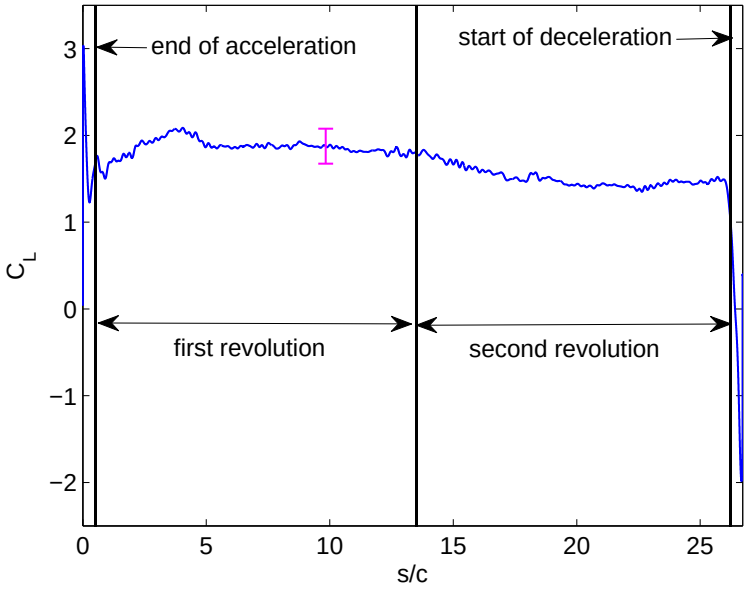

(a) Lift coefficient

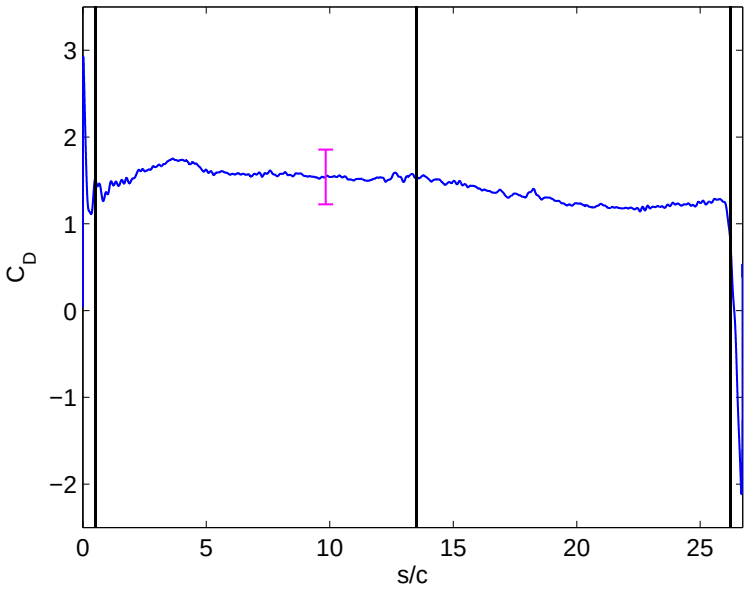

(b) Drag coefficient

Fig. 4.1: Lift and drag coefficients for a rotating wing at a fixed angle of attack of 45 deg accelerating over 0.50 chord-lengths of travel at a three-quarter span reference Reynolds number of 15,000.

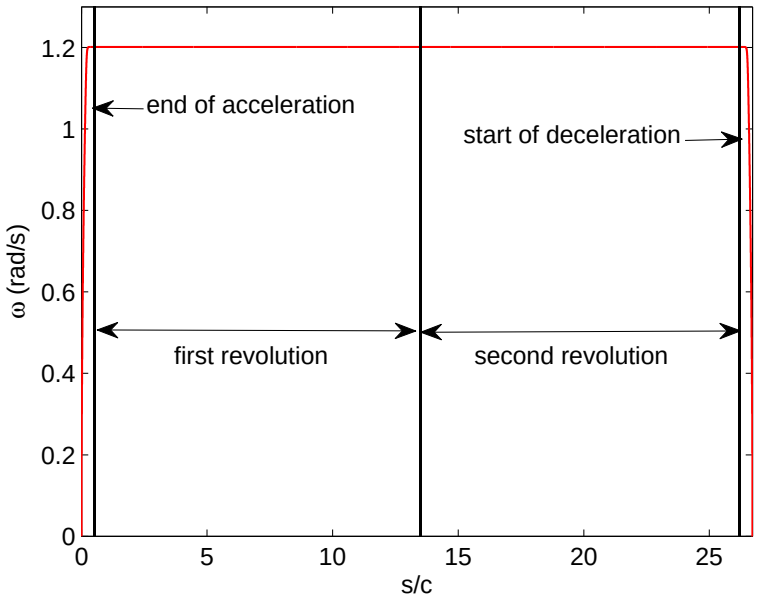

Fig. 4.2: Heavily smoothed velocity profile: angular velocity with respect to s/c at a Reynolds number of 15,000.

acceleration region, the value of C_L peaks at approximately 3.04 and C_D peaks at a value near 2.92. The initial peak observed in Figure 4.3 is a result of a combination of the inertial force and added mass. The wing was rotated in air to measure the inertial forces, the forces measured were very small and were within the noise of the force transducer. Since the inertial forces on the wing were small it can be concluded that a majority of the initial peak is a result of added mass.

Added mass is the enhanced and/or altered inertia of an object that is caused by motion of a fluid around the object [70]. When a flapping wing accelerates through a fluid, it forces some fluid to accelerate with it and the inertial resistance of this fluid creates a reaction force on the wing [71]. Knowledge of added mass is very crucial to understand the performance of objects (in this case, a flat plate)

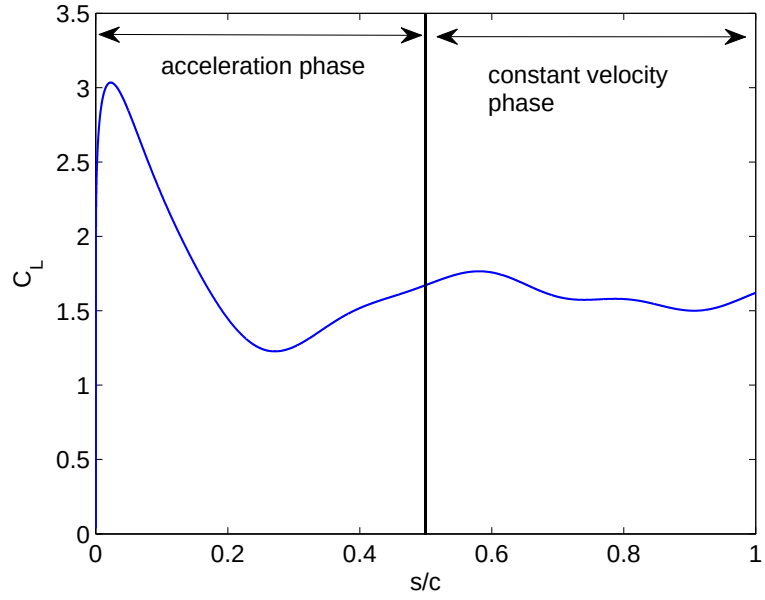

(a) Lift coefficient

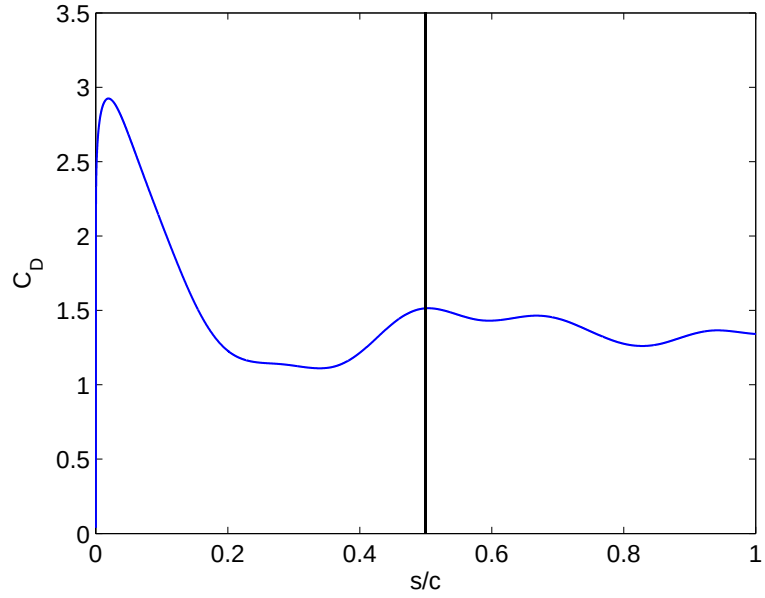

(b) Drag coefficient

Fig. 4.3: The acceleration phase for a rotating wing at a fixed angle of attack of 45 deg accelerating over 0.50 chord-lengths of travel at a three-quarter span reference Reynolds number of 15,000.

underwater. The drag added mass of a flat plate at a fixed angle of attack can be theoretically modeled as a cylinder with a diameter d as shown in Figure 4.4, where the diameter is defined as

$$d = c\sin(\alpha) \tag{4.3}$$

where c is the wing chord and α is the angle of attack. For a cylinder accelerating in a stationary fluid, Jones et al. [71] found the pressure force in the x-direction per unit length of a cylinder to be

$$F_p^{'} = -\frac{1}{4}\rho d^2 \pi \frac{\mathrm{d}u}{\mathrm{d}t} \tag{4.4}$$

where ρ is the density of the fluid, d is the diameter of the cylinder, and $\mathrm{d}u/\mathrm{d}t$ is the linear acceleration. In this case, the pressure force is acting in the same direction as the drag and can therefore account for the added mass phenomenon in the drag force. The total drag force acting on the cylinder is therefore

$$F_d = \int_{r_r}^{r_t} \frac{1}{4}\rho d^2 \pi \frac{\mathrm{d}u}{\mathrm{d}t}\mathrm{d}r \tag{4.5}$$

where r_t and r_r are the distances between the axis of rotation and wingtip and axis of rotation and root, respectively. The linear acceleration can be converted to the angular acceleration using:

$$u = r\omega \tag{4.6}$$

$$\frac{\mathrm{d}u}{\mathrm{d}t} = r\frac{\mathrm{d}\omega}{\mathrm{d}t} \tag{4.7}$$

where r is the radius. Substituting Equation 4.7 into 4.5

$$F_d = \int_{r_r}^{r_t} \frac{1}{4}\rho d^2 \pi r \frac{\mathrm{d}\omega}{\mathrm{d}t}\mathrm{d}r. \tag{4.8}$$

Integrating Equation 4.8,

$$F_d = \frac{1}{8}\rho d^2 \pi \frac{\mathrm{d}\omega}{\mathrm{d}t}\left[r_t^2 - r_r^2\right]. \tag{4.9}$$

Substituting Equation 4.3 into 4.9,

$$F_d = \frac{1}{8}\rho c^2 \sin^2(\alpha)\pi \frac{\mathrm{d}\omega}{\mathrm{d}t}\left[r_t^2 - r_r^2\right]. \tag{4.10}$$

Substituting Equation 4.10 into 4.2,

$$C_{D\text{addedmass}} = \frac{(3/4)\pi\ c\sin^2(\alpha)(\mathrm{d}\omega/\mathrm{d}t)(r_t^2 - r_r^2)}{\omega_{max}^2(r_t^3 - r_r^3)}. \tag{4.11}$$

The maximum value of added mass of a rotating wing is thus

$$C_{Dpeak} = \max\left[\frac{(3/4)\pi\ c\sin^2(\alpha)(\mathrm{d}\omega/\mathrm{d}t)(r_t^2 - r_r^2)}{\omega_{max}^2(r_t^3 - r_r^3)}\right] \tag{4.12}$$

where α is the angle of attack, c is the wing chord, $\mathrm{d}\omega/\mathrm{d}t$ is the angular acceleration of the wing, ω_{max} is the maximum angular velocity, and r_t and r_r are the distances between the axis of rotation and wingtip and axis of rotation and root, respectively. It should be noted that the added mass is proportional to the angular acceleration of the wing, therefore, increasing the acceleration should result in a larger added mass peak. The theoretical drag coefficient added mass peak at $s/c \approx 0.02$ (calculated using Equation 4.12) was found to be 2.28, suggesting that the peak observed in the experimental data (shown in Figure 4.3) is indeed due to added mass.

4.2.2 Constant Velocity Phase

Figure 4.5(a) focuses on the constant velocity region of Figure 4.1(a), and the axes have been adjusted to provide clarity. After the wing enters the constant

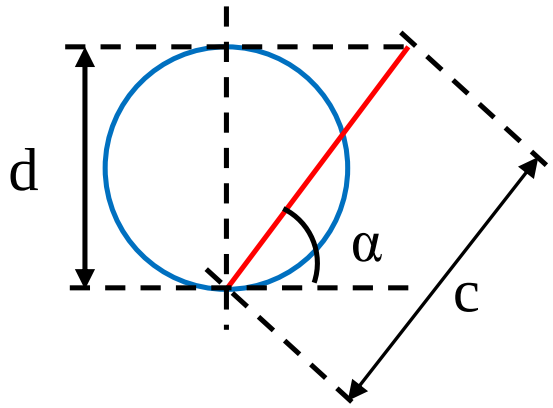

Fig. 4.4: A flat plate at a fixed angle of attack can be modeled as a cylinder with a diameter d.

velocity phase, the lift and drag coefficients level out to an intermediate value for the remainder of the first revolution. This "steady-state" is achieved after about 1.4 s (5 chord-lengths of travel and approximately 133 deg stroke angle). The value of C_L and C_D appear to be essentially constant for about 2.8 s ($\approx$ 8.5 chord-lengths and approximately 227 deg stroke angle). The "steady-state" mean for this region of the first revolution was found to be 1.85 for the coefficient of lift and 1.55 for the coefficient of drag. After the wing enters the second revolution, the coefficients begin to decrease before leveling out to a second intermediate value. The coefficient of lift and drag averaged over 8.5 chord-lengths of travel (to remain consistent with the previous revolution results) during the second revolution are 1.44 and 1.21, respectively. A 22% reduction of C_L and C_D was observed from the first revolution. It is postulated that this is a result of the wing interacting with the wake from its previous stroke.

The aerodynamic efficiency, quantified by L/D, is shown in Figure 4.6. Similar

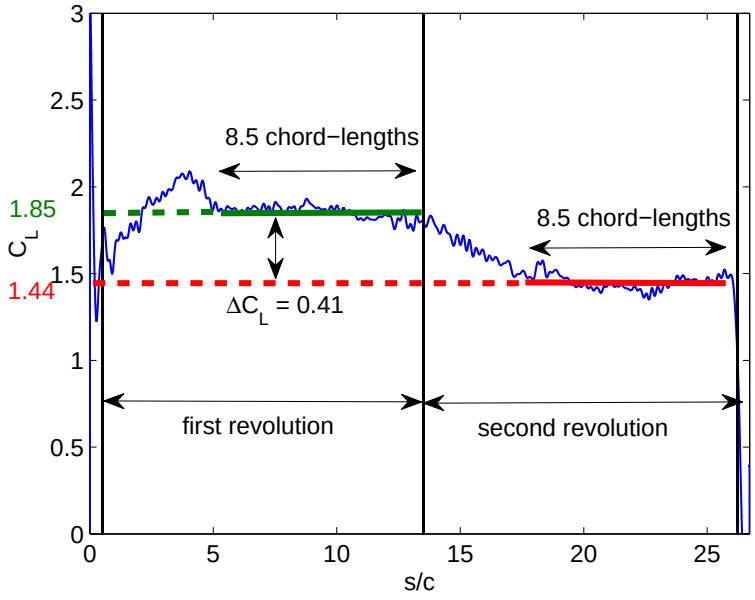

(a) Lift coefficient

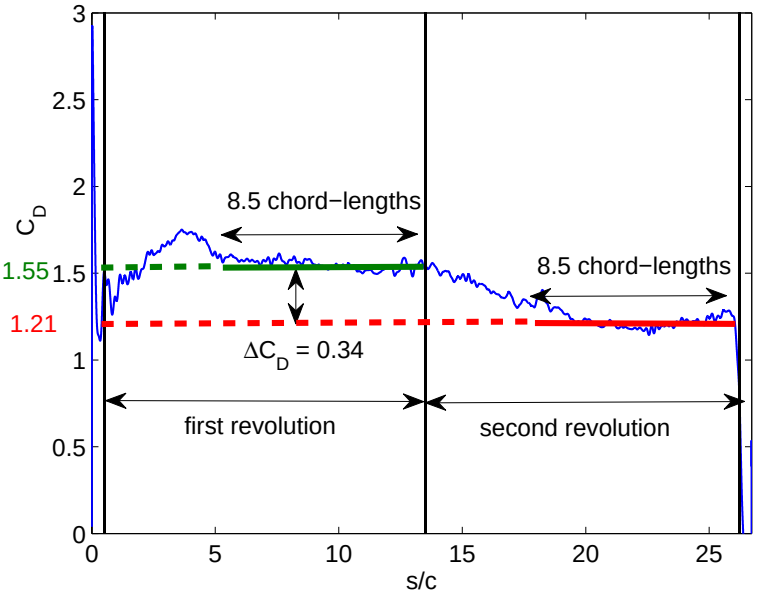

(b) Drag coefficient

Fig. 4.5: Constant velocity phase lift and drag coefficients for a rigid rotating wing at a fixed angle of attack of 45 deg accelerating over 0.50 chord-lengths of travel at a three-quarter span reference Reynolds number of 15,000.

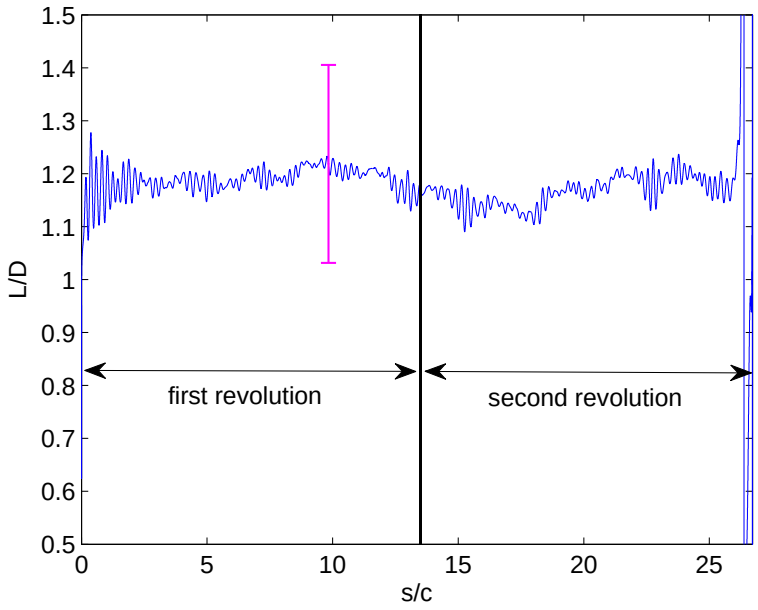

Fig. 4.6: Lift-to-drag ratio versus s/c for the rotating wing at $Re = 15{,}000$ accelerated over 0.50 chord-lengths of travel.

to previous figures, the black vertical line ($s/c = 13.5$) marks the end of the first revolution and the beginning of the second revolution. The lift-to-drag ratio appears to remain roughly constant through out the two revolutions. This is because reduction of C_L for the second revolution is proportional to the reduction in C_D (approximately 22%). This leads to an averaged (over each revolution) lift-to-drag ratio of 1.19 for the first revolution and 1.17 for the second revolution. The difference is so small that it is within experimental error.

Table 4.1: Maximum angular acceleration at Re = 15,000.

Accelerating over	Velocity profile	Maximum angular acceleration (rad/s^2)[2]
0.25c	smoothed (both)	15.5
	linear	6.2
0.50c	smoothed (both)	7.8
	linear	3.1
1.0c	smoothed (both)	3.9
	linear	1.6

4.3 Variation of Velocity Profiles

As described in Chapter 2, the wing stroke was programmed using three different velocity profiles: linear in time, heavily smoothed ($a = 30$), and lightly smoothed ($a = 75$). The wing was accelerated such that it reached its maximum angular velocity after 0.25, 0.50, or 1.0 chord-lengths of travel at the three-quarter span reference plane (plots shown in Section 2.3). For each case, the wing stroke was symmetric such that the wing acceleration and deceleration phases were equal and opposite. The wing reached a maximum stroke angle (θ) of 720 deg, corresponding to $s/c = 27$. The maximum angular acceleration for all the tested velocity profiles is given in Table 4.1.

The goal of this set of experiments was to determine the effect of the velocity

[2]The maximum angular acceleration is the same for both of the smoothed cases, however, the instantaneous acceleration values during transition are higher for the lightly smoothed case.

profile on the lift force generated by the wing. In order to compare the difference between the smoothed and the linear velocity profiles, it was important that the value of the accelerations were same. However, during the acceleration and deceleration phase of the wing stroke mentioned in Section 3.4, the acceleration of the smoothed and the linear cases were different. This difference in the acceleration values was a result of setting $t_1 = 30\%$ of t_2 as explained in Section 2.3.1. As a result, the accelerations for the smoothed cases were $\approx 60\%$ (see Table 4.1) greater than that of the linear case. Therefore, the transients observed during the acceleration and deceleration phase for the smoothed and unsmoothed velocity profiles cannot be directly compared. A slightly better comparison can be made with the linear velocity profile accelerating over 0.25 chord-lengths of travel, though the acceleration still differes by approximately 20%.

Figure 4.7 shows the coefficients of lift and drag with respect to the stroke-to-chord ratio for the three different velocity profiles at $Re = 15{,}000$. The coefficient curves for the smoothed cases correspond to $s_a/c = 0.50$ and the coefficient curves for the linear case correspond to $s_a/c = 0.25$. The three lines, blue, red and green correspond to the linear, heavily smoothed, and lightly smoothed velocity profiles, respectively. The three vertical lines indicate the end of acceleration phase, the end of the first and beginning of second revolution, and the beginning of the deceleration phase. Regardless of the velocity profile, an initial transient peak is observed. The coefficients then undershoot, overshoot again, and eventually achieve a relatively constant value after 5 chord-lengths of travel. As previously seen in Section 4.2, the coefficients decrease when the wing enters the second revolution. Another transient

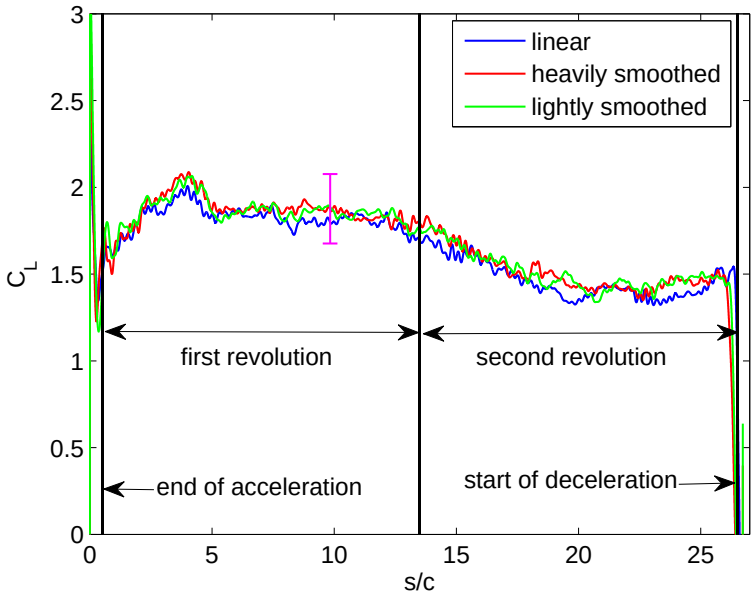

(a) Lift coefficient for entire wing stroke $\theta_{max} = 720\,\text{deg}$

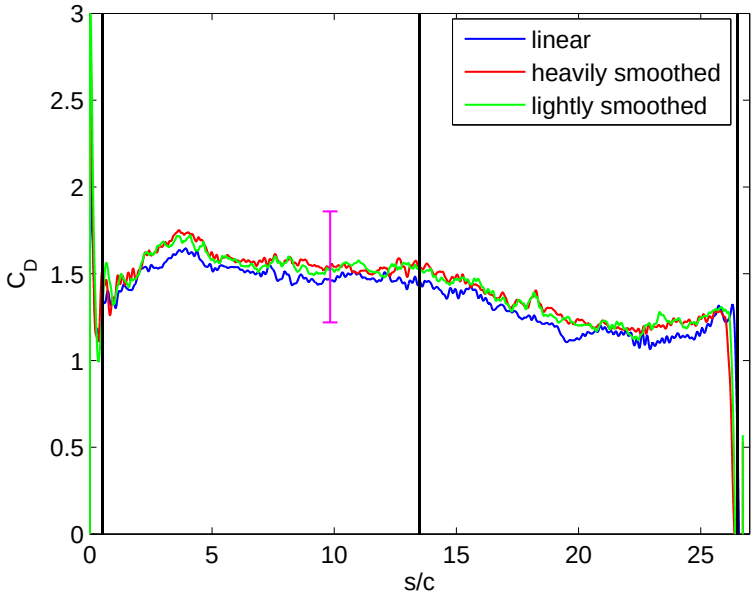

(b) Drag coefficient for entire wing stroke $\theta_{max} = 720\,\text{deg}$

Fig. 4.7: Comparison of three different velocity profiles for a rotating wing at $Re = 15{,}000$.

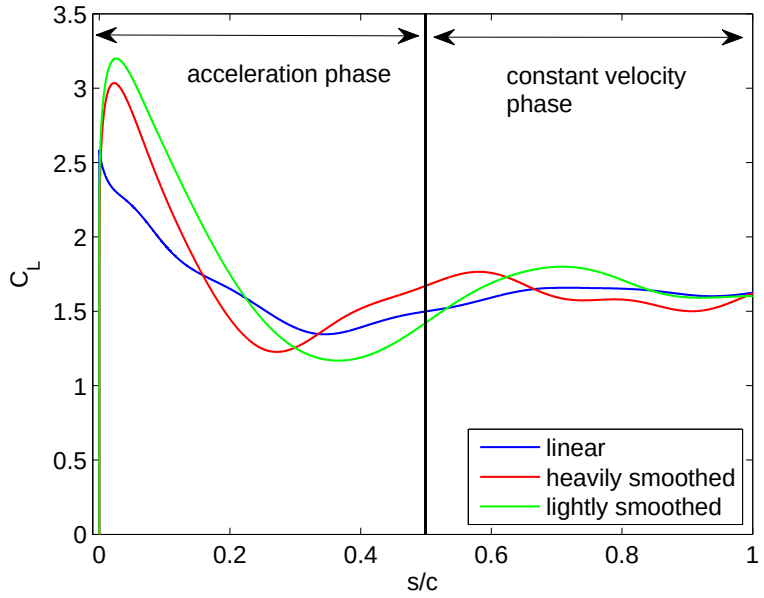

(a) Lift coefficient for early wing stroke

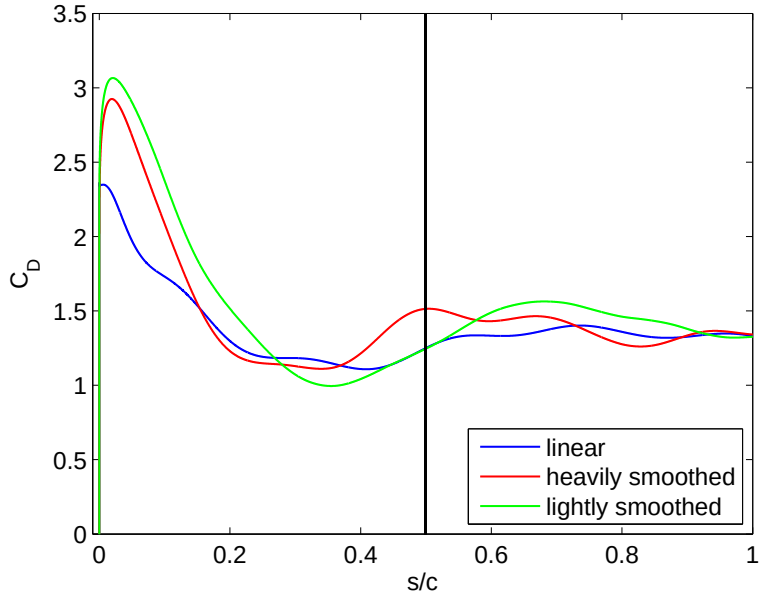

(b) Drag coefficient for early wing stroke

Fig. 4.8: Comparison of the acceleration phase for three different velocity profiles for a rotating wing at $Re = 15{,}000$.

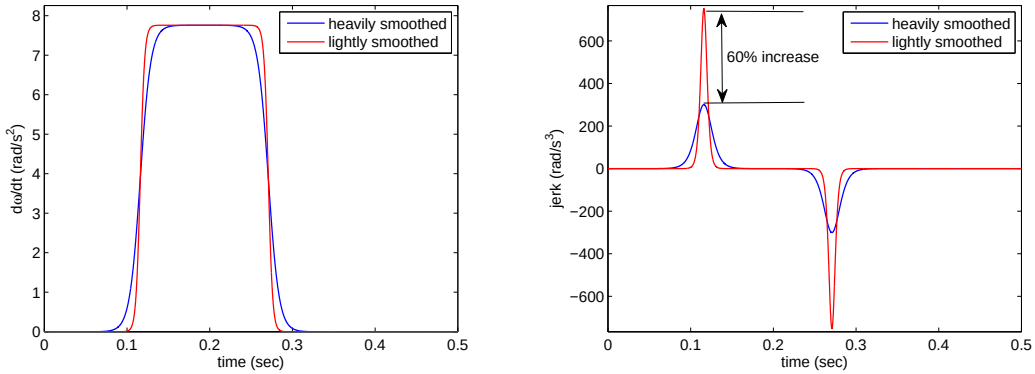

(a) Acceleration vs. time

(b) Jerk vs. time

Fig. 4.9: Acceleration and jerk with respect to time for the two smoothed profiles, heavily smoothed (blue) and lightly smoothed (red) for a wing accelerating over 0.50 chord-lengths of travel.

trough is observed when the wing decelerates. This is in agreement with the results seen in Figure 4.7. Only the shape of the transients during the acceleration and deceleration phase are affected by smoothing the velocity profile (see Figure 4.8).

Even though the maximum angular acceleration of the two smoothed cases are the same, the heavily smoothed case has a much lower jerk when compared to the lightly smoothed case. Figure 4.9 compares the acceleration and jerk for a wing accelerating over 0.50 chord-lengths of travel at a Reynolds number of 15,000. The higher jerk in Figure 4.9(b) for the lightly smoothed case compared to the heavily smoothed case is a result of sharper transitions during acceleration. Therefore a higher jerk implies a higher instantaneous value of acceleration which results in a larger added mass. If the added mass is higher, the peak in the force coefficients will be higher as well. This agrees with the coefficients in Figure 4.8.

Figure 4.8 focuses on the early wing stroke to highlight the transients of C_L and C_D that occur during the wing's acceleration. The lightly smoothed case has a greater transient peak than the heavily smoothed case. A phase shift between the two cases is also observed. Figure 4.10(a) shows the raw and filtered data for the linear velocity profile early in the wing stroke. In this a phase shift is observed, which is a result of filtering. However, Figure 4.10(b) shows the raw data for all three profiles to show that the phase shift observed between the two smoothed cases is not a result of filtering. Both velocity profiles result in the same overall shape regardless of the value of the transient or the phase shift. Once the wing completes the acceleration phase, the coefficients converge to similar values and trends.

The transient peak for the linear case is very sharp and abrupt, unlike the two smoothed cases. This sharp and abrupt nature of the linear profile coefficients is a result of the jump in the acceleration of the wing as shown in Figure 2.7. The value of the linear profile peak is lower than the two smoothed cases. This is likely because the acceleration for the linear profile is 20% lower than that of the smoothed cases. This was verified using Equation 4.12. The theoretical added mass for both the smoothed cases is 2.28, whereas the added mass for the linear case is 1.82, which is $\approx$ 20% less than 2.28. This agrees with the experimental results.

4.4 Variation of Acceleration Profiles

For this set of experiments, the heavily smoothed velocity profile and three-quarter span reference Reynolds number of 15,000 were used, and the distance over

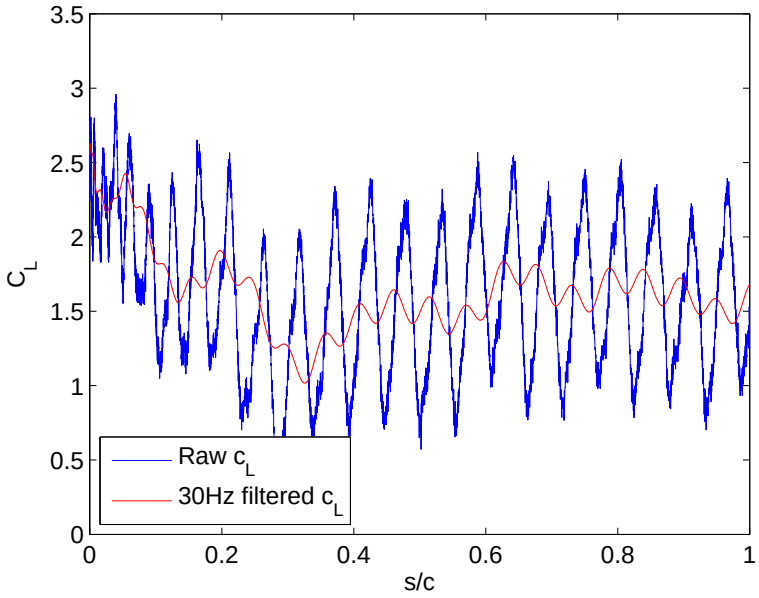

(a) Lift coefficient for linear velocity profile

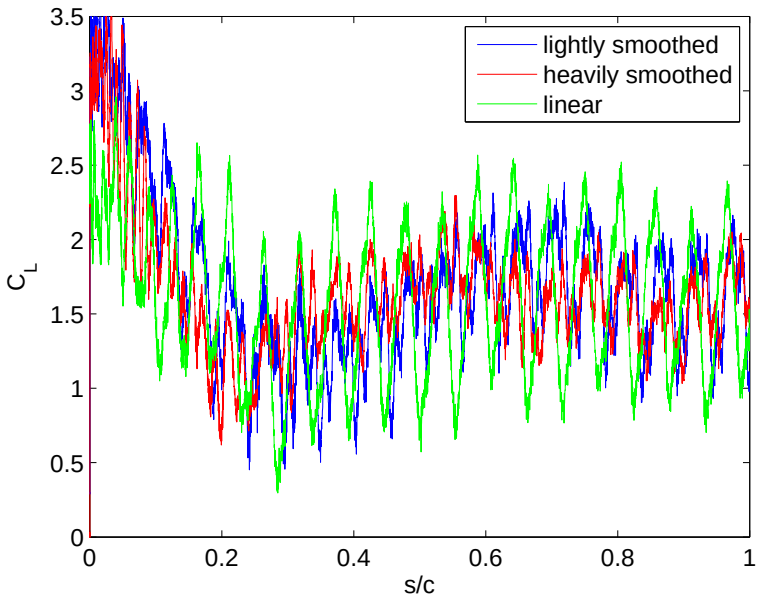

(b) Lift coefficient for all three cases

Fig. 4.10: Raw and filtered lift coefficients for three different velocity profiles for a rotating wing at $Re = 15{,}000$.

which the wing accelerated (and thus the value of the wing's acceleration) was varied. The wing was accelerated from rest to constant velocity over 0.25, 0.50 and 1.0 chord-lengths of travel at the three-quarter span reference span. The distance over which the wing accelerated is denoted as s_a and is non-dimensionalized using the wing's chord. This ratio is expressed as s_a/c. Table 4.1 shows the value of the wing's acceleration for each of the three cases. Figure 4.11 shows the lift and drag coefficient curves for different values of s_a/c. As in previous figures, the vertical black line indicates the end of the first revolution and the beginning of the second. The vertical line indicating the end of the acceleration phase is not shown as it varies for the three cases. As in the baseline case described in Section 4.2.1, a transient peak is observed as soon as the wing beings to accelerate. The maximum angular acceleration determines the magnitude of the peak (refer to Equation 4.12). For all values of s_a/c, the "steady-state" lift and drag coefficients (past 1 chord-length of travel since the largest distance over which the wing accelerates is 1 chord-length) are the same for all acceleration profiles.

Figure 4.12 shows the acceleration phase of the wing stroke for each of the three cases. The dashed blue, red, and green vertical lines mark the end of acceleration for the $s_a/c = 0.25$, 0.50 and 1.0 cases, respectively. Since $s_a/c = 0.25$ has the greatest acceleration, it was expected to have the greatest peak as shown in Table 4.2. The added mass values were calculated using Equation 4.12. At $s_a/c = 0.25$, a high peak is observed in both the lift and drag coefficients with a max $C_L \approx 4.5$ and max $C_D \approx 4.0$. The max coefficients of lift and drag were both approximately 3.0 for $s_a/c = 0.50$ and the coefficients were both approximately 1.75 for $s_a/c = 1.0$. In all

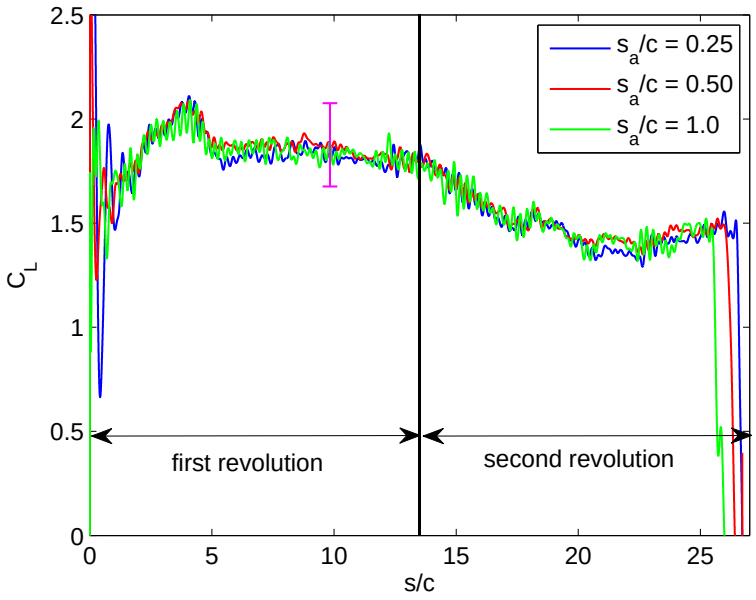

(a) Lift Coefficient

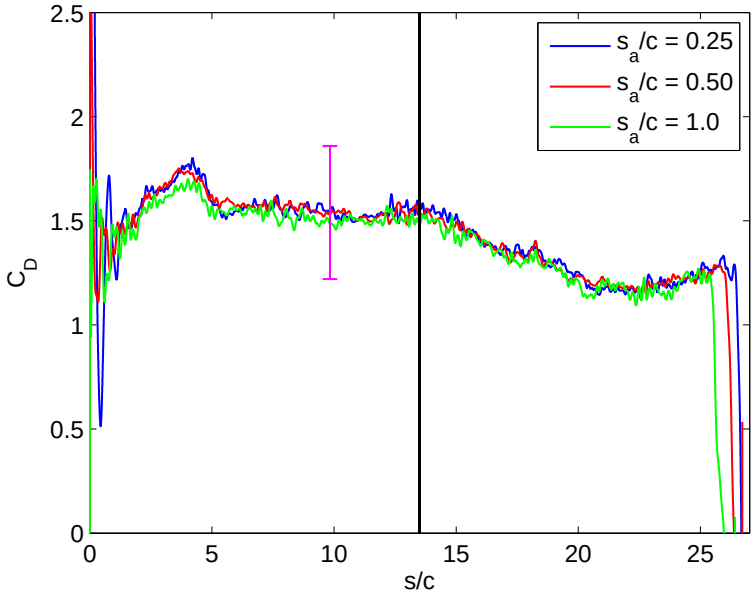

(b) Drag Coefficient

Fig. 4.11: Constant velocity phase lift and drag coefficients. Comparison of three different s_a/c for a rotating wing at $Re = 15{,}000$.

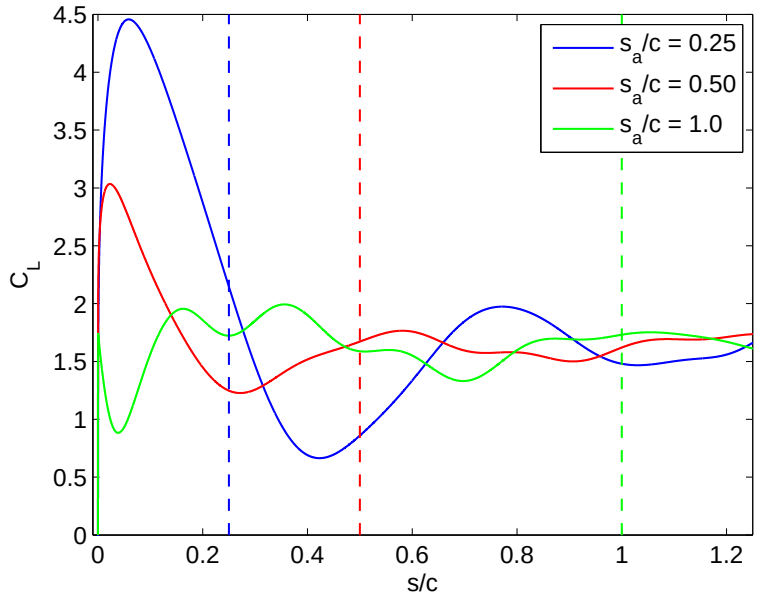

(a) Lift Coefficient

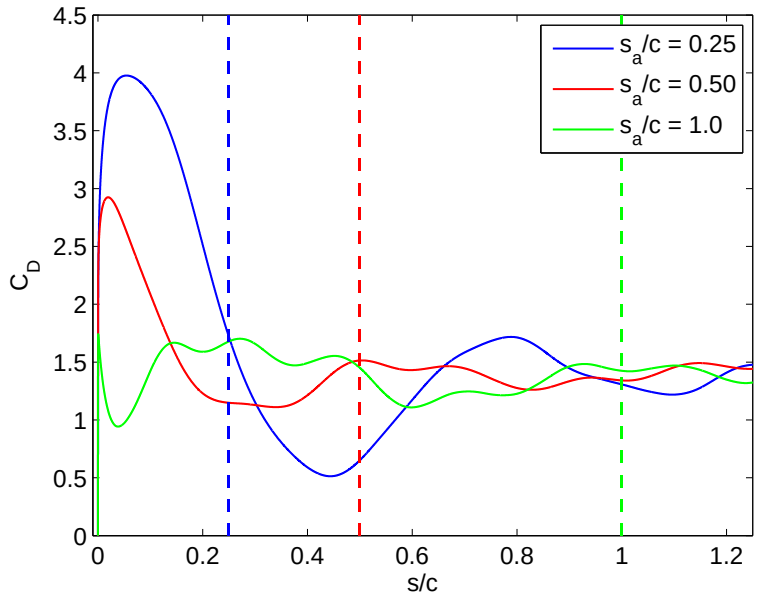

(b) Drag Coefficient

Fig. 4.12: Comparison of the acceleration phase for three different accelerations for a rotating wing at $Re = 15{,}000$. The dashed blue, red and green lines indicate the transition from acceleration to constant velocity for the respective s_a/c values.

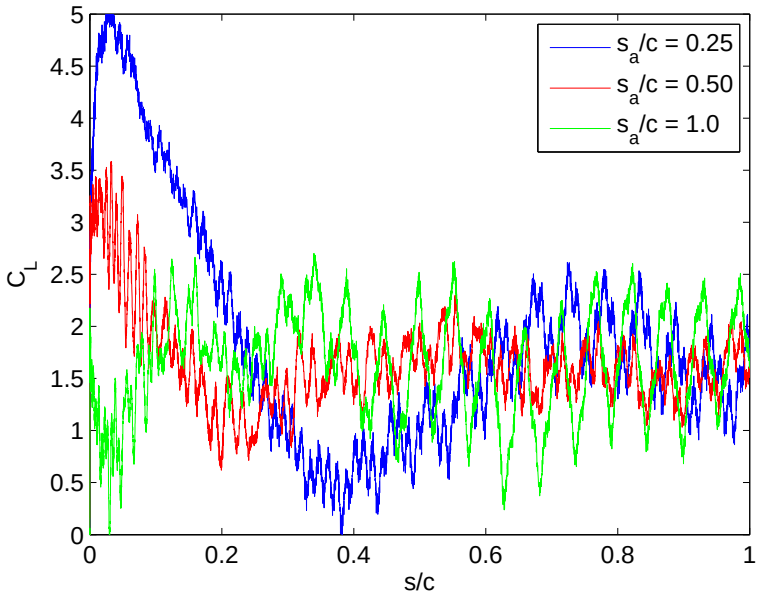

Fig. 4.13: Raw lift coefficients for the acceleration portion of the wing stroke.

three cases, a high added mass peak is observed for the lift and drag coefficients, the peaks then undershoot, rise again, and eventually level out after 5 chord-lengths of travel. The raw lift coefficients for this portion of the wing stroke are shown in Figure 4.13.

4.5 Variation of Reynolds Number

All the quantitative results presented thus far have been at a Reynolds number of 15,000. To investigate the effect of Reynolds number on the rotating wing, different Reynolds numbers were achieved by rotating the same wing at different angular velocities. The other Reynolds numbers tested were 10,000 and 25,000. This range of Reynolds numbers were chosen due to the limitations of the force transducer. Unfortunately the data collected at a Reynolds number of 10,000 is not shown as

Table 4.2: Theoretical added mass peak values at Re = 15,000.

Accelerating over	Maximum angular acceleration (rad/s^2)	Theoretical added mass max(C_D)	Measured max(C_D)
0.25c	15.5	4.54	3.98
0.50c	7.8	2.28	2.92
1.0c	3.9	1.14	1.74

the signal to noise ratio was very poor and this resulted in very high RMS error values, as shown previously in Table 2.3.

Figure 4.14 compares the lift and drag coefficients for two Reynolds numbers of 15,000 and 25,000. The wing travels faster for the higher Reynolds number, but by plotting the force coefficients with respect to s/c (instead of time) the forces can be compared as the stroke angle varies. An initial added mass peak is seen for both cases. After the initial peak, the coefficients fall, rise again, and eventually settle into a "steady-state" value. After the wing finishes the first revolution, there is a drop in both the lift and the drag coefficient curves regardless of the Reynolds number. These are the same trends which have were discussed in earlier sections.

Increasing the Reynolds number from 15,000 to 25,000 does not appear to affect the force coefficients. In Figure 4.14(a), the curves lay near each other, and both curves follow the same trends previously described. For $1 \leq s/c \leq 5$, there

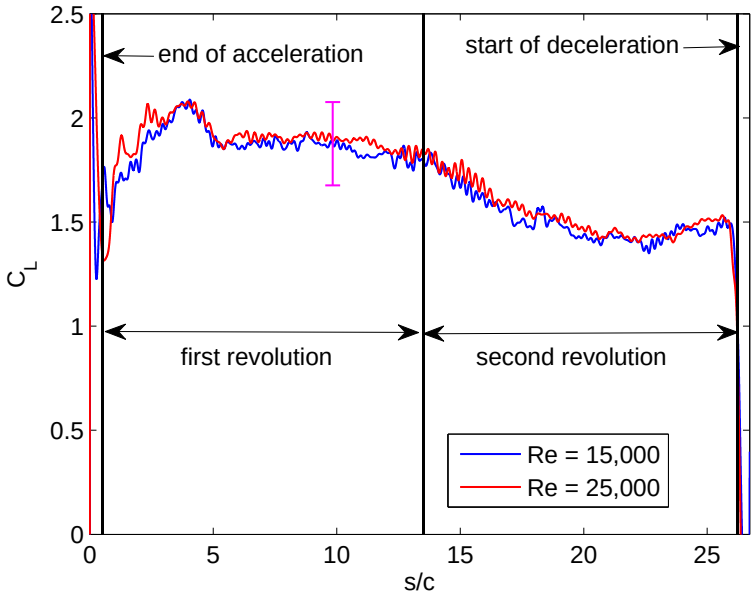

(a) Lift Coefficient

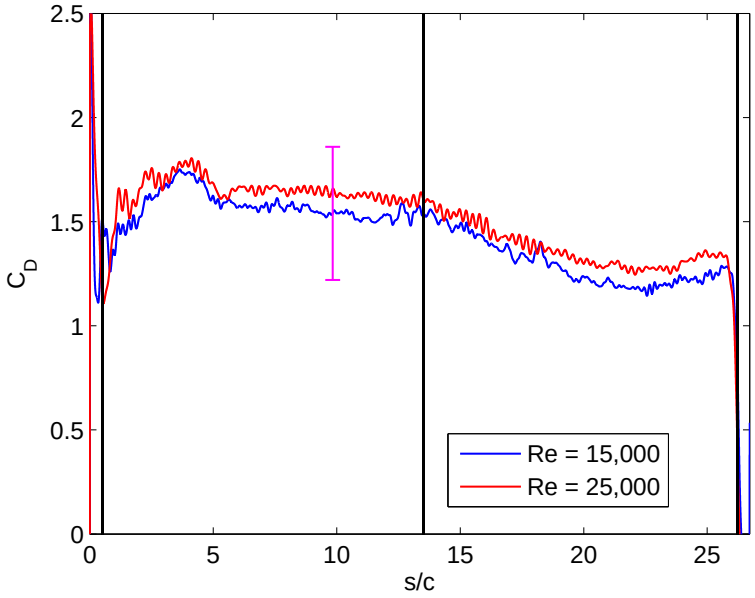

(b) Drag Coefficient

Fig. 4.14: Lift and drag coefficients. Comparison of different Reynolds numbers for a rotating wing accelerating over 0.50 chord-lengths of travel.

is a small difference in how the two curves increase, but the difference is within experimental error (error bars shown in Figure 4.14(a)). Figure 4.14(b) shows the drag coefficient curves for the two Reynolds numbers. Unlike the lift curves, there is a small noticeable difference in the values. The drag coefficient is consistently slightly higher for $Re = 25{,}000$ when compared to $Re = 15{,}000$ case. However, the difference is very small and is within experimental error so a definitive conclusion cannot be drawn. Overall, lift and drag coefficients do not appear to change significantly in the Reynolds number range tested.

4.6 Wing Flexibility

All the experiments described to this point used a rigid wing. Since natural fliers employ flexible wings, further experiments were performed to investigate and compare a "flexible wing" to its rigid counterpart. The flexible wing was modeled with two segments configured to allow passive deformation about the half chord as described by Eldredge [40, 43, 39] and in Section 1.4.5. The anterior section of the wing was fixed at a constant angle of attack of 45 deg, and the posterior section was allowed to passively deform. Since the trailing half-chord of the flexible wing was free-to-pivot, it hung down vertically (at a 90 deg angle of attack) before the wing motion began.

Figure 4.16(a) shows the coefficient of lift for the two wings at a Reynolds number of 15,000. The schematic of the flexible wing in Figure 4.15(a), shows the wing's steady-state position at a Reynolds number of 15,000. The passively

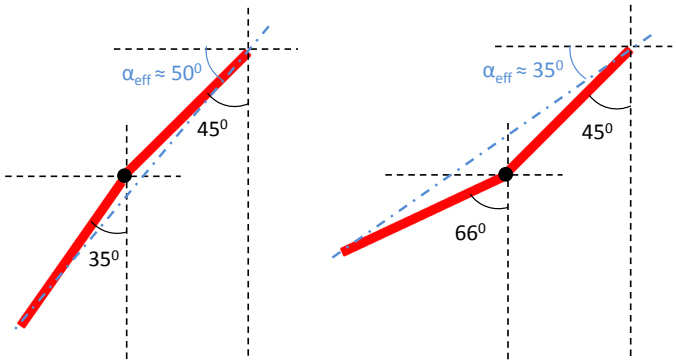

(a) $Re = 15{,}000$ (b) $Re = 25{,}000$

Fig. 4.15: Steady-state flexible wing positions.

deforming trailing half of the flexible wing deflects by an angle of 35 deg during steady-state, resulting in an effective angle of attack of $\approx$ 50 deg. The effective angle of attack of 50 deg is close to the angle of attack of the rigid wing (45 deg). Since the effective angle of attack of the flexible wing is very similar to the angle of attack of the rigid wing, the forces generated by both wings should be about equal. Figure 4.16(a) shows that the two wings do generate similar amounts of lift. Like the rigid wing, the lift coefficient decreases from the first to the second revolution.

It is also important to note that during the acceleration and deceleration phases, the peak lift coefficient of the rigid wing is much greater than the corresponding peak for the flexible wing (shown in Figure 4.17). It is postulated that the force the fluid exerted on the flexible wing was less than the force exerted on the rigid wing, since the passive half of the flexible wing was free to deform during the acceleration and deceleration phases.

Figure 4.16(b) shows the drag coefficient for the two wings at Reynolds number

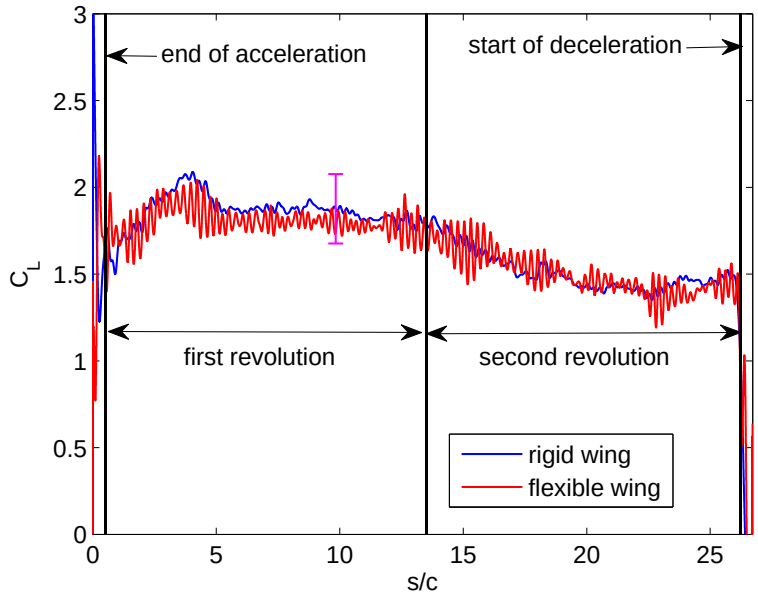

(a) Lift Coefficient

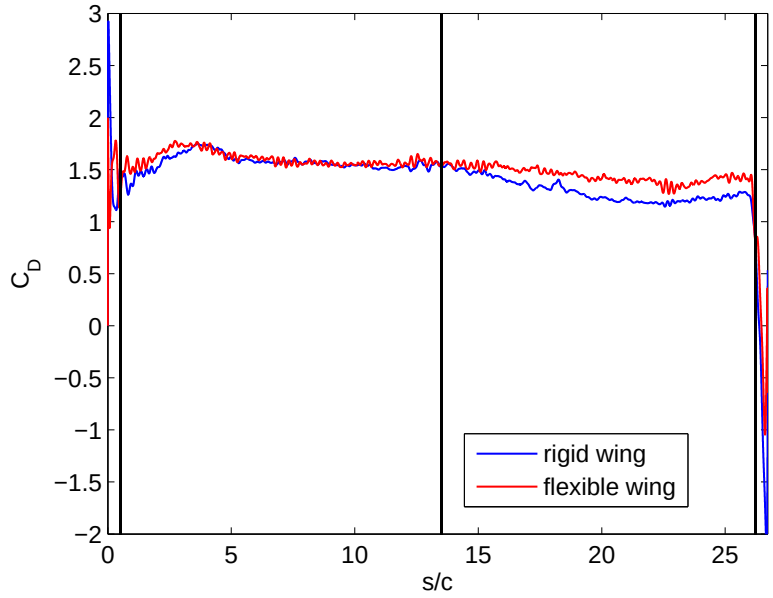

(b) Drag Coefficient

Fig. 4.16: Coefficient of lift and drag for a rigid and half chord flexible wing at $Re = 15{,}000$.

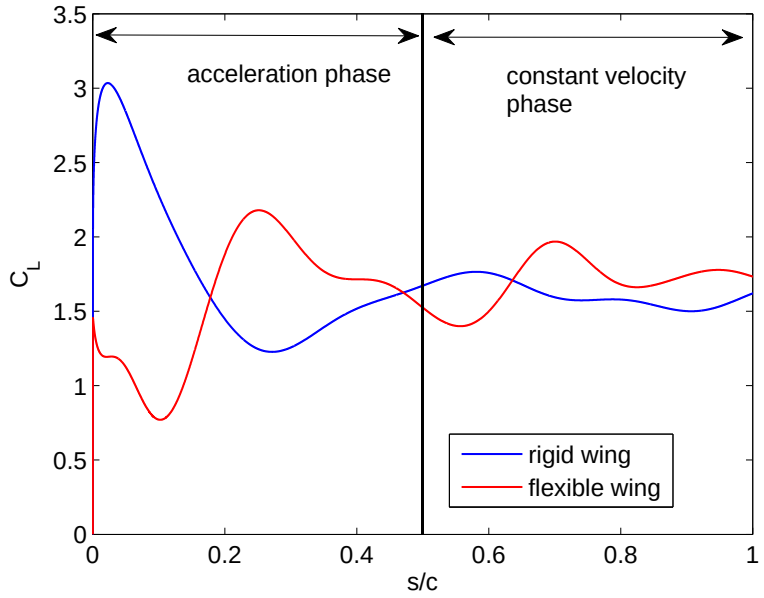

(a) Lift Coefficient

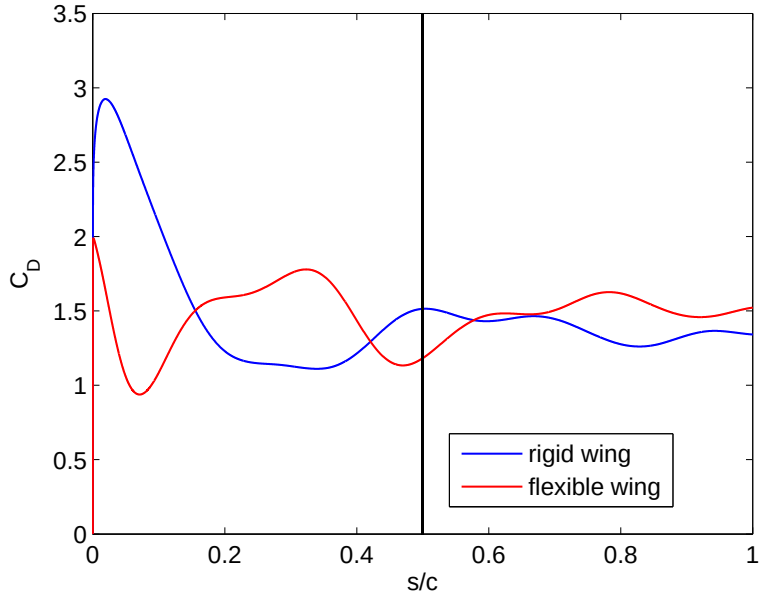

(b) Drag Coefficient

Fig. 4.17: Comparison of the acceleration phase for the coefficient of lift and drag for a rigid and half chord flexible wing at $Re = 15{,}000$.

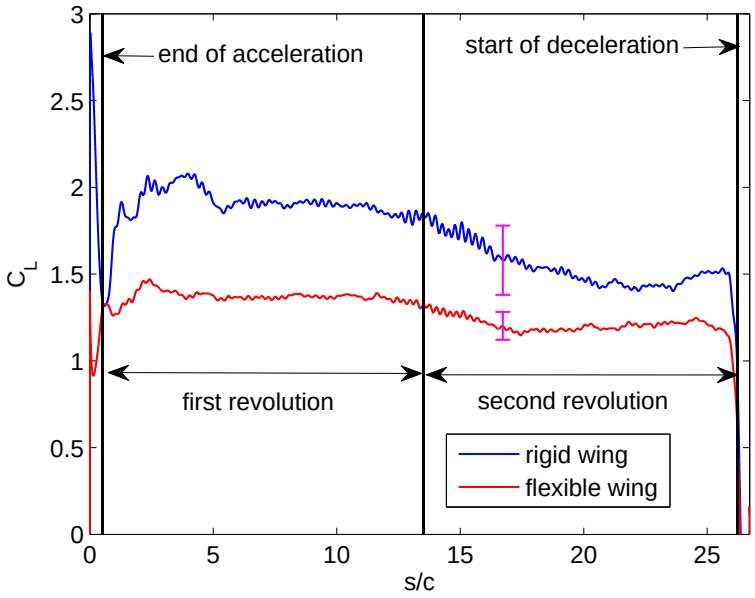

(a) Lift Coefficient

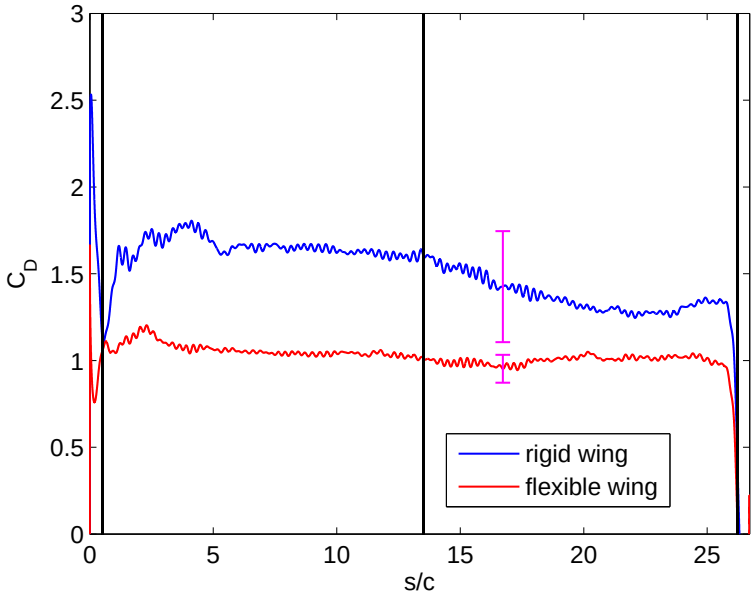

(b) Drag Coefficient

Fig. 4.18: Coefficient of lift and drag for a rigid and half chord flexible wing at $Re = 25{,}000$.

of 15,000. One prominent feature of the plot is the relatively large peak coefficient of drag for the half chord flexible wing as compared to the peak coefficient of drag for the rigid wing (see Figure 4.17(b)). The passive portion of the flexible wing hangs vertically when the wing is at rest. When the wing begins to accelerate, the forces pushing this portion of the wing to its steady-state position (see Figure 4.15(a)) oppose the wing motion. Initially, the passive portion of the wing acts like a wall to the oncoming flow, and therefore most of the forces on the section are drag forces. As the flow continues to push the wing to its steady-state position, the drag decreases since the flow encountered a smaller frontal area. Once in "steady-state", the rigid wing and flexible wing had similar values of drag coefficient. During the second revolution, however, the drag of the rigid wing decreased considerably as compared to the flexible wing. This might have been due to the flexible wing deflecting in a way that kept the drag coefficient at a high value when the wing moved through its wake from the first rotation. Figure 4.16 shows that the lift and drag coefficients in the constant velocity region for both wings were very similar.

The experiment was repeated for $Re = 25{,}000$ to study the effect of Reynolds number on performance. The unsteady lift peaks during the acceleration and deceleration portions of the wing motion can again be seen in Figure 4.18. "Steady-state" is achieved after $\approx 1.4\,\mathrm{s}$ (5 chord-lengths of travel) for the rigid wing, but after only about $0.7\,\mathrm{s}$ (2 chord-lengths of travel) for the flexible wing. This could be a result of the flexible wing's ability to deform, which causes variations of the effective angle of attack. This may allow the overall flexible wing circulation to achieve a stable value in a shorter time.

Table 4.3: Steady-state lift coefficient average values.

Steady State Region	$Re = 15{,}000$	$Re = 25{,}000$
First Rotation	$C_{L_{flex}} = 1.79$	$C_{L_{flex}} = 1.37$
	$C_{L_{rigid}} = 1.86$	$C_{L_{rigid}} = 1.90$
Second Rotation	$C_{L_{flex}} = 1.41$	$C_{L_{flex}} = 1.20$
	$C_{L_{rigid}} = 1.44$	$C_{L_{rigid}} = 1.46$

Table 4.4: Steady-state drag coefficient average values.

Steady State Region	$Re = 15{,}000$	$Re = 25{,}000$
First Rotation	$C_{D_{flex}} = 1.57$	$C_{D_{flex}} = 1.04$
	$C_{D_{rigid}} = 1.55$	$C_{D_{rigid}} = 1.64$
Second Rotation	$C_{D_{flex}} = 1.39$	$C_{D_{flex}} = 1.01$
	$C_{D_{rigid}} = 1.21$	$C_{D_{rigid}} = 1.30$

The "steady-state" mean of the lift coefficient over 8.5 chord-lengths of travel, for the rigid wing and flexible wing are given in Table 4.3. The first rotation average on the rigid wing at Re = 15,000 was C_L = 1.86 and the second rotation average was C_L = 1.44. These averages are similar to the corresponding flexible wing values for Re = 15,000. However, at a Re = 15,000, the flexible wing lift coefficients are higher than the corresponding flexible wing values at Re = 25,000. This is because an increase of Reynolds number to 25,000 caused the deflection angle of the passive half of the flexible wing to increase to approximately 66 deg, which was greater than the 45 deg angle of attack of the anterior section of the wing (refer to Figure 4.15(b)). This resulted in an effective angle of attack of approximately 35 deg for the flexible wing, reduced from 50 deg at Re = 15,000. This decreased effective angle of attack accounts for the lower lift coefficients measured for the flexible wing at Re = 25,000.

The aerodynamic efficiency, quantified by L/D, of both wings is shown for Reynolds numbers 15,000 and 25,000 in Figure 4.19(a) and 4.19(b). Comparing the performance of the two different wings reveals that the efficiency of the rigid wing was higher throughout both rotations at a Reynolds number of 15,000. At Re = 25,000, the efficiency of the flexible wing was higher than the rigid wing during the first rotation. However, efficiency of the flexible wing approached the efficiency of the rigid wing during the second rotation. The "steady-state" L/D values for both Reynolds numbers can be found in Table 4.5. It can be seen that the performance of the flexible wing at Re = 25,000 was generally better than at Re = 15,000. This improved performance persisted though the second revolution as well. It is postulated that the angle by which the posterior section flexible wing

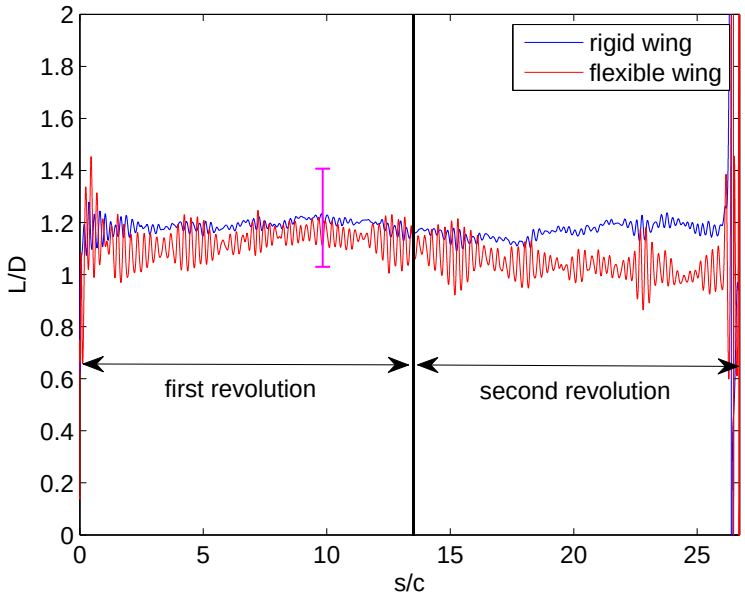

(a) $Re = 15{,}000$

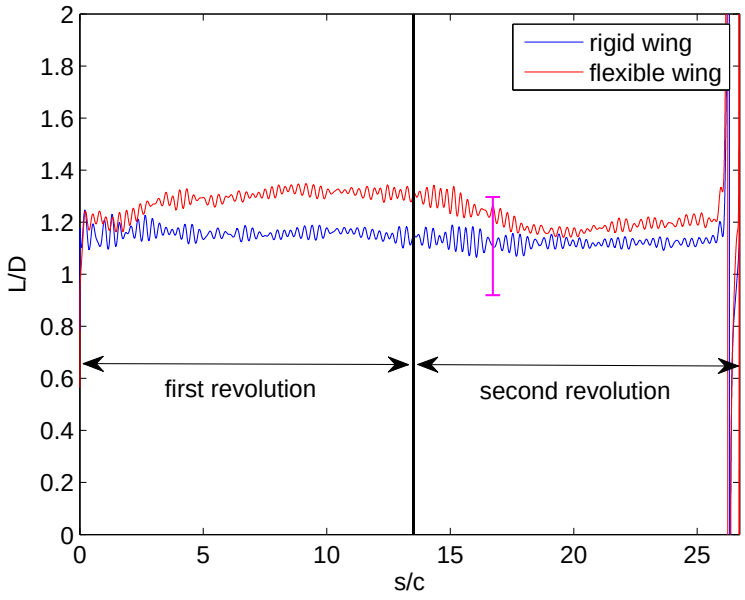

(b) $Re = 25{,}000$

Fig. 4.19: Lift-to-drag ratio for the rigid and flexible wing.

Table 4.5: Steady-state lift-to-drag ratio averages.

Steady State Region	Re = 15,000	Re = 25,000
First Rotation	$L/D_{flex} = 1.11$	$L/D_{flex} = 1.30$
	$L/D_{rigid} = 1.19$	$L/D_{rigid} = 1.16$
Second Rotation	$L/D_{flex} = 1.02$	$L/D_{flex} = 1.18$
	$L/D_{rigid} = 1.17$	$L/D_{rigid} = 1.12$

deflects changes during the second revolution, resulting in a lower effective angle of attack. Further experimentation is required to confirm this hypothesis.

4.7 Summary

This chapter presented and discussed force measurements for a rigid and chordwise flexible rotating wing at a fixed angle of attack of 45 deg. As the wing accelerated, a peak is observed in the lift and drag coefficients. This peak is largely due to added mass. The added mass was theoretically calculated for the drag force and agreed with the peaks observed from the experimentation. After the initial peak, the coefficients undershoot, increase again and eventually attain a "steady-state" after 5 chord-lengths of travel (approximately 133 deg of rotation). The coefficients remain at this intermediate value for the remainder of the first revolution. When the wing begins the second revolution, both the lift and drag coefficients begin to decrease again and level out at a second intermediate value until the wing begins to decelerate. The lift and drag coefficients values decrease by approximately 22%

from the first to the second revolution.

Other parameters that were varied include velocity profiles, acceleration profiles, Reynolds number and wing flexibility. Varying the velocity and acceleration profiles only affected the acceleration phase of the lift and drag coefficients. Higher accelerations resulted in a higher added mass and peak value of the coefficients. Increasing the Reynolds number from 15,000 to 25,000 did not have an effect on the rigid wing, but significant difference was observed on the flexible wing. This difference in the coefficients observed on the flexible wing is a result of the ability of wing's ability to passively deform. At a Re = 15,000, the the angle of attack (chord line from leading edge to trailing edge) was 50 deg, and at Re = 25,000 the angle of attack was 35 deg. For all cases tested, a high lift was achieved during the acceleration phase and in the first revolution, though values dropped off in the second revolution.

Chapter 5

Concluding Remarks

5.1 Overview

The work presented in this thesis examined the flow and forces acting on a model of a hovering insect wing stroke. The wing stroke was modeled as a fixed angle of attack rectangular flat plate of aspect ratio 2 rotating about the root. Dye flow visualization was performed at Reynolds numbers of 5,000 and 10,000 to identify the flow features that formed on the wing. A force balance was used to quantify the aerodynamic forces produced by these flow structures. Due to the limitations of the submersible force transducer used, the force acting on the wing were measured at higher Reynolds numbers of 15,000 and 25,000. Several parameters were varied in each set of experiments. Additionally, a new model that introduced unsteady pitch variation on the rotating wing was developed. Preliminary dye flow visualization was performed on the pitching-and-rotating wing to begin to characterize the effect of unsteady pitch variations on the structure of the flow.

5.2 Conclusions of the Study

5.2.1 Flow Visualization on the Rotating Wing

1. Dye injection at the wing root at a Reynolds number of 5,000 indicated the formation of a coherent leading edge vortex (LEV) near the wing root, as shown in Figure 3.1. Further outboard, the leading edge vortex became less coherent and eventually burst. As the wing continued to rotate for multiple revolutions, the spanwise location where the leading edge vortex burst moved inboard towards the wing root (Figure 3.2).

2. The flow structures at a Reynolds number of 10,000 were similar to those observed on the $Re = 5{,}000$ case. The location along the wing span where the leading edge vortex burst moved inboard towards the wing root at the higher Reynolds number. The length of the coherent portion of the leading edge vortex appeared to be smaller than for the $Re = 5{,}000$ case. It is hypothesized that increasing the Reynolds number induces vortex bursting earlier. This is in agreement with previous findings by Lentink and Dickinson [69].

3. Closing the gap between the wing root and the axis of rotation caused the leading edge vortex to burst nearer to the wing root, and no coherent leading edge vortex was observed for multiple revolutions (see Figures 3.8 and 3.9). However, in this setup the dye was not injected at the true wing root, so it is possible that a coherent leading edge vortex exists inboard the dye injection location.

4. Dye injection performed in the burst vortex revealed several small scale vortices forming and shedding at the leading edge. Shed vortices traveled downstream over the wing and began recirculating about a point. As time progressed, this recirculation region grew and a large scale recirculating region (i.e., the burst leading edge vortex) was observed, extending from the leading edge to the trailing edge.

5. Regardless of the wing's acceleration, a recirculation region formed when the wing's angle of attack was 45 deg. At lower acceleration rates, larger vortices formed on the rotating wing. At higher acceleration rates the vortices shed with at a higher frequency.

6. At a fixed angle of attack of 15 deg, unlike the 45 deg case, no recirculation region was present (see Figure 3.13), suggesting that there is no attached leading edge vortex present on the wing at this incidence.

5.2.2 Flow Visualization on the Pitching-and-Rotating Wing

1. A new pitching-and-rotating wing model was designed and constructed to introduce unsteady pitch variations on the rotating wing. Wing rotation was driven by a stepper motor above the water line and unsteady pitch variations by a submergible servo motor.

2. At low angles of attack, the flow structures on the pitching-and-rotating wing were similar to the flow structures observed on the rotating-only wing at an angle of attack of 15 deg.

3. At high angles of attack, a large recirculating region formed near the leading edge with attached flow behind it. As the wing pitched down, the recirculating region was ejected off the wing vertically instead of shedding downstream as in the fixed angle of attack case. These flow structures appeared to reestablish for the subsequent pitch cycles.

5.2.3 Force Measurements on the Rotating Wing

1. During the acceleration phase of the rotating wing stroke, a high peak in the lift and drag coefficients was observed. This peak is attributed to the added mass of the wing due to the unsteady motion. The added mass was calculated analytically for the drag force and agreed with the peaks observed experimentally.

2. During the constant velocity phase of the wing stroke, the force coefficients decreased. They briefly undershot but eventually increased, and after 5 chord-lengths of travel leveled out at an intermediate value for the remainder of the first revolution. See Figure 4.5(a) for an example.

3. During the second revolution of the constant velocity phase of the wing stroke, both the lift and drag coefficients decreased again and leveled out at a second, lower, intermediate value until the wing begins to decelerate. The residual velocity present in water from the previous wing stoke, induced a downwash on the wing. This downwash reduced the effective angle of attack of the wing resulted in lower coefficients.

4. Varying the distance over which the wing accelerated, and thus the wing acceleration, only affected the force coefficients during the acceleration phase of the wing stroke (see Figure 4.12).

5. The shape of the lift curve for the flexible wing was similar to that of the rigid wing. The initial peak observed on the flexible wing was much smaller than that observed on the rigid wing.

6. At a Reynolds number of 15,000, the rigid and flexible wings had approximately the same force coefficients, likely because the steady-state deflection angle of the flexible wing resulted in an effective angle of attack near that of the rigid wing. At $Re = 25{,}000$, the trailing half of the wing deflected upwards, resulting in a angle of attack that was much lower than the angle of attack of the rigid wing, and lower lift and drag coefficients.

5.3 Remarks for Future Work

The current work revealed a coherent leading edge vortex near the root of a rotating wing and began investigating a wide variety of possible parameter variations. This experimental setup developed here could be used as-is to provide a more complete understanding of the many factors that may affect the stability of the leading edge vortex. Some suggestions for near-term future work are as follows:

1. Dye flow visualization on the rotating wing at a fixed angle of attack showed the LEV burst at the quarter span location on the wing. However, when the

wing was further rotated, the length of the coherent portion of the LEV grew and burst further outboard. Similarly, when the forces were measured, after the initial peak the coefficients undershot, overshot and eventually settled at an intermediate value for the remainder of the first revolution. It is unclear as to what causes this initially burst LEV to grow or why the force coefficients fluctuate. This region of the wing stroke should be studied more closely to understand the behavior of the LEV within 5 chord-lengths of travel.

2. To fully understand the effect of smoothing the wing's velocity profile, the acceleration of the linear and smoothed cases should be matched and force measurements and dye flow visualization repeated for these cases. This will help understand if there is any merit in smoothing the velocity profile, and what the effect of doing so is on the flow on the wing and the forces produced.

3. To better understand the effect of the wing root geometry, the gap between the wing root and the axis of rotation should be eliminated by reducing the length of the tygon shaft rather than filling it in as was done in the current work. This would maintain the aspect ratio of the wing (though it would alter the radius of gyration). Dye flow visualization should then be performed at the true wing root. This will help determine whether a coherent leading edge vortex is present for multiple revolutions very near the wing root.

4. For the flexible wing, a spring could be incorporated in an attempt to increase lift and/or L/D while keeping the benefits of a hinged wing's ability to deform. Additional force measurements could also be performed on both the flexible

wing used in this experiment, and also another configuration of an aspect ratio 2 wing that is free to rotate about the leading edge. This test case would isolate the passively deforming portion of the wing and would help to better understand the aerodynamic forces that act on passively deforming wings. Flow visualization could be done on all of the wings described above. Finally, high speed videos could be taken of the accelerating portion of the wing stroke. This data, combined with force measurements, will help to illuminate the mechanisms that occur during the accelerating phase of the rotation.

5. The pitching-and-rotating wing model developed in this work is a new and unique model. This uniqueness should be exploited in an attempt to understand the benefits of introducing unsteady variations in pitch on the rotating-only wing model. Flow visualization should be performed by injecting dye at the wing root. This will help determine the effect of pitch on the coherent leading edge vortex near the wing root. After qualitatively understanding the behavior of the flow structures, particle image velocimetry should be performed on the pitching-and-rotating wing. A crucial parameter that was not varied in this work is the reduced frequency (k). The reduced frequency can be easily varied by increasing or decreasing the rate of change of pitch by programing the servo motor appropriately. An understanding of the effects of the reduced frequency could prove to be very crucial to be able to successfully exploit unsteady mechanism which will help design a flapping wing micro air vehicle.

The research presented in this thesis has provided a well-rounded qualitative understanding of the flow structures near the leading edge of a rotating wing. However, several quantitative properties such as the vorticity, circulation, and strength of the leading edge vortex are still unknown. A quantitative method such as particle image velocimetry is required to measure these properties of the flow structures. The behavior of these quantities along with the results presented in this work will provide a complete understanding of the aerodynamics of a rotating wing.

Bibliography

[1] McMichael, J. M. and Francis, M. S., "Micro Air Vehicles - Toward a New Dimension in Flight," TTO document, DARPA, July 1996.

[2] Pines, D. J. and Bohorquez, F., "Challenges Facing Future Micro-Air-Vehicle Development," *Journal of Aircraft*, Vol. 43, No. 2, March-April 2006, pp. 290–305.

[3] Keennon, M. and Grasmeyer, J., "Development of Two MAVs and Vision of the Future of MAV Design," *39th Aerospace Sciences Meeting and Exhibit*, AIAA 2001-127, Reno, NV, 8-11 January 2001.

[4] Keennon, M. and Grasmeyer, J., "Development of the Black Widow and Microbat MAVs and a Vision of the Future of MAV Design," *AIAA/ICAS International Air and Space Symposium and Exposition: The Next 100 Years*, AIAA 2003-2901, Dayton, OH, 14-17 July 2003.

[5] Grasmeyer, J. and Keennon, M., "Development of the Black Widow Micro Air Vehicle," *AIAA*, 2001.

[6] Chopra, I., "Hovering Micro Air Vehicles: Challenges and Opportunities," *Proceedings of the American Helicopter Society Specialists*, International Forum on Rotorcraft Multidisciplinary Technology, Seoul, Korea, 15-17 October 2007.

[7] Ramasamy, M., Leishman, J., and Lee, T., "Flow Field of a Rotating wing MAV," *62nd Annual National Forum Proceedings of the American Helicopter Society*, Phoenix, AZ, 9-11 May 2006.

[8] McMasters, J., "Reflections of a Paleoaerodynamicist," *Perspectives in Biology and Medicine*, Vol. 29, No. 2, 1986.

[9] McMasters, J. H. and Henderson, M. L., "Low Speed Single Element Airfoil Synthesis," *Technical Soaring*, Vol. 6, No. 2, 1980, pp. 1–21.

[10] Lissaman, P. B. S., "Low-Reynolds-Number Airfoils," *Annual Review of Fluid Mechanics*, Vol. 15, January 1983, pp. 223–239.

[11] Leishman, J. G., *Principles of Helicopter Aerodynamics*, Cambridge University Press, Cambridge, United Kingdom, 2nd ed., 2006.

[12] Shyy, W., Lian, Y., Tang, J., Viieru, D., and Liu, H., *Aerodynamics of Low Reynolds Number Flyers*, Cambridge University Press, New York, NY, 2008.

[13] Ellington, C. P., van den Berg, C., Willmott, A. P., and Thomas, A. L. R., "Leading-Edge Vortices in Insect Flight," *Nature*, Vol. 384, No. 6610, December 1996, pp. 626–630.

[14] Wootton, R., "From Insects to Microvehicles," *Nature*, Vol. 403, No. 6766, January 2000, pp. 144.

[15] Singh, B. and Chopra, I., "Wing Design and Optimization for a Flapping Wing Micro Air Vehicle," *American Helicopter Society Annual Forum*, Baltimore, MD, 7-10 June 2004.

[16] Dickinson, M. H., Lehmann, F.-O., and Sane, S. P., "Wing Rotation and the Aerodynamic Basis of Insect Flight," *Science*, Vol. 284, No. 5422, 18 June 1999, pp. 1954–1960.

[17] Dickinson, M. H. and Götz, K. G., "Unsteady Aerodynamic Performance of Model Wings at Low Reynolds Numbers," *Journal of Experimental Biology*, Vol. 174, No. 1, January 1993, pp. 45–64.

[18] Birch, J. M. and Dickinson, M. H., "Spanwise flow and the attachment of the leading-edge vortex on insect wings," *Nature*, Vol. 412, No. 6848, August 2001, pp. 729–733.

[19] Usherwood, J. R. and Ellington, C. P., "The Aerodynamics of Revolving Wings: I. Model Hawkmoth Wings," *Journal of Experimental Biology*, Vol. 205, No. 11, 2002, pp. 1547–1564.

[20] Leishman, J., "Dynamic stall experiments on the NACA 23012 aerofoil," *Experiments in Fluids*, Vol. 9, 1990, pp. 49–58.

[21] McCroskey, W. J., "Unsteady Airfoils," *Annual Review of Fluid Mechanics*, Vol. 14, 1982, pp. 285–311.

[22] van den Berg, C. and Ellington, C. P., "The Vortex Wake of a "Hovering" Model Hawkmoth," *Philosophical Transactions of the Royal Society of London, Series B, Biologial Sciences*, Vol. 352, No. 1351, 1997, pp. 317–328.

[23] Maxworthy, T., "Experiments on the Weis-Fogh Mechanism of Lift Generation by Insects in Hovering Flight, I. Dynamics of the 'fling'," *Journal of Fluid Mechanics*, Vol. 93, No. 1, July 1979, pp. 47–63.

[24] Anderson, J. D., *Fundamentals of Aerodynamics*, McGraw-Hill, New York, NY, 2007.

[25] Lambourne, N. and Bryer, D., "The bursting of leading-edge vortices–some observations and discussions of the phenomenon." *Aero. Res. Counc*, , No. 3282, 1961, pp. 36.

[26] Tarascio, M. J., Ramasamy, M., Chopra, I., and Leishman, J. G., "Flow Visualization of Micro Air Vehicle Scaled Insect-Based Flapping Wings," *Journal of Aircraft*, Vol. 42, No. 2, March-April 2005, pp. 385–390.

[27] Srygley, R. B. and Thomas, L. R., "Unconventional Lift-Generating Mechanisms in Free-Flying Butterflies," *Nature*, Vol. 420, 2002, pp. 660–662.

[28] Warrick, D. R., Tobalske, B. W., and Powers, D. R., "Lift Production in the Hovering Hummingbird," *Proceedings of The Royal Society*, Vol. 276, 2009, pp. 3747–3752.

[29] Shyy, W. and Liu, H., "Flapping Wings and Aerodynamic Lift: The Role of Leading-Edge Vortices," *Journal of Aircraft*, Vol. 45, No. 12, 2007, pp. 2817–2819.

[30] Sun, M. and Tang, J., "Unsteady Aerodynamic Force Generation by a Model Fruit Fly Wing in Flapping Motion," *The Journal of Experimental Biology*, Vol. 205, 2002, pp. 55–70.

[31] Ramasamy, M. and Leishman, J. G., "Phase-Locked Particle Image Velocimetry Measurements of a Flapping Wing," *Journal of Aircraft*, Vol. 43, No. 6, November-December 2006, pp. 1867–1875.

[32] van den Berg, C. and Ellington, C. P., "The Three-Dimensional Leading-Edge Vortex of a "Hovering" Model Hawkmoth," *Philosophical Transactions of the Royal Society of London, Series B, Biologial Sciences*, Vol. 352, No. 1351, 1997, pp. 329–340.

[33] Raney, D. and Slominski, E., "Mechanization and Control Concepts for Biologically Inspired Micro Aerial Vehicles," *AIAA Guidance, Navigation, and Control Conference and Exhibit*, No. 5345, Austin, TX, 11-14 August 2003.

[34] Magnus, G., "Über die Abweichung der Geschosse," *Adhandlungen der Königlichen Akademie der*, Wissenschaften zu Berlin, 1853.

[35] Seshadri, P., *Biometric Insect Flapping Wing Aerodynamics and Controls for Micro Air Vehicles*, Master of Science Thesis, University of Maryland, College Park, MD, 2011.

[36] Ramsey, J., *Flow Field and Performance Measurements of a Flapping-Wing Device Using Particle Image Velocimetry*, Master of Science Thesis, University of Maryland, College Park, MD, 2011.

[37] Shyy, W., Lian, Y., Tang, J., Liu, H., Trizila, P., Stanford, B., Bernal, L., Cesnik, C., Friedmann, P., and Ifju, P., "Computational Aerodynamics of Low Reynolds Number Plunging, Pitching and Flexible Wings for MAV Applications," *Acta Mech Sin*, Vol. 24, July 2008, pp. 351–373.

[38] Shyy, W., Klevebring, F., Nilsson, M., Sloan, J., Carroll, B., and Fuentes, C., "Rigid and Flexible Low Reynolds Number Airfoils," *Journal of Aircraft*, Vol. 36, June 1999, pp. 523–529.

[39] Eldredge, J., Toomey, J., and Medina, A., "On the roles of chord-wise flexibility in a flapping wing with hovering kinematics," *Journal of Fluid Mechanics*, Vol. 659, June 2010, pp. 94–115.

[40] Toomey, J. and Eldredge, J. D., "Numerical and Experimental Study of the Fluid Dynamics of a Flapping Wing With Low Order Flexibility," *Physics of Fluids*, Vol. 20, 2008.

[41] Dudley, R., *The Biomechanics of Insect Flight*, Princeton University Press, 2000.

[42] Weis-Fogh, T., "Quick Estimates of Flight Fitness in Hovering Animals, Including Novel Mechanisms For Lift Production," *Journal of Experimental Biology*, Vol. 59, 1973, pp. 169–230.

[43] Toomey, J. and Eldredge, J., "Numerical and Experimental investigation of the role of flexibility in flapping wing flight," *36th AIAA Fluid Dynamics Conference and Exhibit*, No. 3211, San Francisco, CA, 5-8 June 2006.

[44] Hui, H. and Kumar, A., "An experimental study of flexible membrane wings in flapping flight," *47th AIAA Aerospace Sciences Meeting Including The New Horizons Forum and Aerospace Exposition*, No. 876, Orlando, FL, 5-8 January 2009.

[45] Kim, D., Han, J., and Kwon, K., "Wind tunnel tests for a flapping wing model with a changeable chamber using micro-fiber composite actuators." *Smart Mater Structures*, Vol. 18, No. 024008, 2009, pp. 1–8.

[46] Agrawal, A. and Agrawal, S., "Design of bio-inspired flexible wings for flapping wing micro-sized air vehicle applications." *Advanced Robotics*, Vol. 23, 2009, pp. 979–1002.

[47] Ellington, C. P., "The Aerodynamics of Hovering Insect Flight, I. The Quasi-Steady Analysis," *Philosophical Transactions of the Royal Society of London, Series B, Biologial Sciences*, Vol. 305, No. 1122, February 1984, pp. 41–78.

[48] Ellington, C. P., "The Aerodynamics of Hovering Insect Flight, II. Morphological Parameters," *Philosophical Transactions of the Royal Society of London, Series B, Biologial Sciences*, Vol. 305, No. 1122, February 1984, pp. 17–40.

[49] Ellington, C. P., "The Aerodynamics of Hovering Insect Flight, VI. Lift and Power Requirements," *Philosophical Transactions of the Royal Society of London, Series B, Biologial Sciences*, Vol. 305, No. 1122, February 1984, pp. 145–181.

[50] Birch, J. M., Dickson, W. B., and Dickinson, M. H., "Force Production and Flow Structure of the Leading Edge Vortex on Flapping Wings at High and Low Reynolds Numbers," *Journal of Experimental Biology*, Vol. 207, No. 7, 2004, pp. 1063–1072.

[51] Wilkins, P. C. and Knowles, K., "The Leading-Edge Vortex and Aerodynamics of Insect-Based Flapping-Wing Micro Air Vehicles," *The Aeronautical Journal*, Vol. 113, No. 1142, April 2009, pp. 253–262.

[52] Ellington, C. P. and Usherwood, J. R., "Lift and Drag Characteristics of Rotary and Flapping Wings," *Fixed and Flapping Wing Aerodynamics for Micro Air Vehicle Applications*, edited by T. J. Mueller, Vol. 195 of *Progress in Astronautics and Aeronautics*, chap. 12, American Institute of Aeronautics and Astronautics, Inc., 1801 Alexander Bell Drive, Reston, Virginia 20191-4344, 2001, pp. 231–248.

[53] Sane, S. P., "The Aerodynamics of Insect Flight," *The Journal of Experimental Biology*, Vol. 206, No. 23, December 2003, pp. 4191–4208.

[54] Usherwood, J. R. and Ellington, C. P., "The Aerodynamics of Revolving Wings: II. Propeller Force Coefficients from Mayfly to Quail," *Journal of Experimental Biology*, Vol. 205, No. 11, 2002, pp. 1565–1576.

[55] DeVoria, A., Mahajan, P., and Ringuette, M., "Vortex Formation and Saturation for Low-Aspect-Ratio Rotating Flat Plates at Low Reynolds Number," *49th AIAA Aerospace Sciences Meeting and Exhibit*, AIAA 2011-396, Orlando, FL, 4-7 January 2011.

[56] Ozen, C. A. and Rockwell, D., "Flow Structure on a Rotating Plate," *Experiments in Fluids*, 2012.

[57] Jones, A. R. and Babinsky, H., "Unsteady Lift Generation on Rotating Wings at Low Reynolds Numbers," *Journal of Aircraft*, Vol. 47, No. 3, 2010, pp. 1013–1021.

[58] Jones, A. R., Pitt Ford, C. W., and Babinsky, H., "Three-Dimensional Effects on Sliding and Waving Wings," *Journal of Aircraft*, Vol. 48, Mar.-Apr. 2011, pp. 633–644.

[59] Jones, A. R. and Babinsky, H., "Reynolds Number Effects on Leading Edge Vortex Development on a Waving wing," *Experiments in Fluids*, online Jan. 2011.

[60] Liu, H., Ellington, C., Kawachi, K., van den Berg, C., and Willmott, A., "A computational fluid dynamic study of hawkmoth hovering," *The Journal of Experimental Biology*, Vol. 201, 1998, pp. 461–477.

[61] Bush, B. and Baeder, J., "Computational Investigation of Flapping-Wing Flight," *37th AIAA Fluid Dynamics Conference and Exhibit*, No. 4209, Miami, FL, 25-28 June 2007.

[62] Birch, J. M. and Dickinson, M. H., "The Influence of Wing Wake Interactions on the Production of Aerodynamic Forces in Flapping Fight," *Journal of Experimental Biology*, Vol. 206, Jul. 2003, pp. 2257–2272.

[63] Sane, S. P. and Dickinson, M. H., "The Control of Flight Force By A Flapping Wing: Lift and Drag Production," *The Journal of Experimental Biology*, Vol. 204, No. 15, August 2001, pp. 2607–2626.

[64] Blondeaux, P., Fornarelli, F., and Guglielmini, L., "Vortex structures generated by a finite-span oscillating foil." *43rd AIAA Aerospace Sciences Meeting and Exhibit*, No. 84, Reno, NV, 10-13 January 2005.

[65] Dong, H., Mittal, R., and Najjar, F., "Wake topology and hydrodynamic performance of low-aspect-ratio flapping foils." *J. Fluid Mech.*, Vol. 566, 2006, pp. 309–343.

[66] Taira, K. and Colonius, T., "Three-dimensional flows around low-aspect-ratio flat-plate wings at low Reynolds numbers." *J. Fluid Mech.*, Vol. 623, 2009, pp. 187–207.

[67] Brunton, S., Rowley, C., Taira, K., Colonius, T.and Collins, J., and Williams, D., "Unsteady aerodynamic forces on small-scale wings: experiments,simulations and models." *46th AIAA Aerospace Sciences Meeting and Exhibit*, No. 520, Reno, NV, 7-10 January 2008.

[68] Eldredge, J. D., Wang, C., and Ol, M. V., "A Computational Study of a Canonical Pitch-up, Pitch-down Wing Maneuver," *39th AIAA Fluid Dynamics Conference*, AIAA 2009-3687, San Antonio, TX, 22-25 June 2009.

[69] Lentink, D. and Dickinson, M. H., "Rotational Accelerations Stabilize Leading Edge Vortices on Revolving Fly Wings," *Journal of Experimental Biology*, Vol. 212, April 2009, pp. 2705–2719.

[70] Kundu, P., Cohen, I., and Dowling, R., *Fluid Mechanics*, Academic Press, Waltham, MA, 5th ed., 2012.

[71] Jones, A. R., *Unsteady Low Reynolds Number Aerodynamics of a Waving Wing*, Phd, University of Cambridge, May 2010.